Wavelength-scale confinement of light and its applications in on-chip photonic devices

Thesis by

Jingqing Huang

In Partial Fulfillment of the Requirements

for the Degree of

Doctor of Philosophy

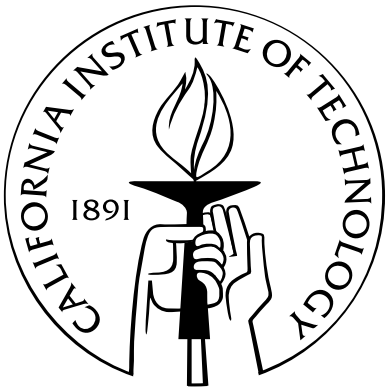

California Institute of Technology

Pasadena, California

2012

(Defended March 13, 2012)

To my parents

Acknowledgements

I am much indebted to many people, who gave me the opportunities, resources, advice, and encouragement to complete the work presented in this thesis. First, I must thank my research advisor Prof. Axel Scherer. His kindness and unreserved advice mean very much to me. Axel has created a lab that fosters creativity and independence, it is a wonderful research environment that I had the privilege to be part of and will sorely miss when I leave.

My gratitude also goes to the thesis committee, Profs. Harry Atwater, Oskar Painter, Changhuei Yang, and Amnon Yariv. It is a privilege to learn from and have my work critiqued by these awesome scientists. They have received me with kindness whenever I went to them for advice. I look to their drive, depth of knowledge, and scientific creativity for inspiration.

I would like to thank the Scherer group members past and present, who are smart, helpful, and good fun: Dvin Adalian, William Fegadolli, William Maxwell Indiana Jones, Harish Ravi, Mark Goldberg, Chieh-Feng Jeff Chang, Erika Garcia; Aditya "Ditty" Rajagopal who inspires practical jokes, Andrew "Homie-K" Homyk who instigates creative pranks, and Sameer Walavalkar who leads the implementation thereof; Muhammad "Jeebs" Mujeeb-U-Rahman, Akram Sadek, Wei-Ting Lai, Liang Feng, John "BJ" Gorman, Samuel Njoroge, Imran Malik; the alumni Yan Chen, Teresa Emery-Adleman, M. David Henry, Michael Hochberg, Zhenyu Li, George Maltezos, Michael Shearn, Saurabh Vyawahare, Chris Walker, Guangxi Wang, and Zhaoyu Zhang.

Special thanks is due to Dr. Tom Baehr-Jones, who patiently taught me nonlinear optics and RF measurements in lab, and allowed me to tag along on the many silicon photonics projects despite my inexperience as a first-year graduate student; Dr. Uday Khankhoje, with whom I shared many coffee breaks and discussions on FDTD simulations, photonic crystals, photography, food, music, literature,

and the ultimate question of life, the universe, and everything; Dr. Joyce Wong, my officemate of six years and a wonderful friend, who is my source of fun daily conversations and sensible advice on everything from research, job search, to restaurant recommendations; Ben Gudlewski, with whom I shared the custody of the temperamental Oxford180 ICP-RIE for many years (I will always remember fondly the creative solutions we came up with to keep that etcher running); Andrew Homyk, whose breadth of knowledge and willingness to help saved me many hours of head-pounding in front of my computer and in lab; and Kate "Femtofairy" Finigan, who is officially the group admin but is really the group mom, making sure that we get our monthly paycheck, that we are eating healthy somewhat, and that we are generally happy and productive.

I should acknowledge that none of the work in this thesis would have been possible without my colleague and partner in crime, Dr. Se-Heon Kim. From the time of his arrival in the group, he has taught me patiently and without reserve. He shared research ideas with me, tolerated my ill-posed questions, and gave me motivation with his quiet perseverance in solving every problem in projects. His tireless curiosity and meticulousness set a fine example for me. It has been invaluable to me to be able to go to such a knowledgeable person whenever I had an idea or a question to discuss. I could ask for a better project mate. I sincerely wish him every success in his career.

At the same time, our collaborators, Dr. Pablo Aitor Postigo in Spain and Drs. Christian Seassal and Philippe Regreny in France, were instrumental in the work reported in this thesis. The high quality InAsP/InP quantum well material provided by Pablo, Christian, and Philippe made possible the lasing results we observed and published.

Most of the devices made in this work were fabricated in the facility of Kavli Nanoscience Institute (KNI), whose smooth running would not be possible without the hard-working lab staff of Mary Sikora, Dr. Guy DeRose, Melissa Melendes, Nils Asplund, Bophan Chhim, Carol Garland, Kevin Kan, Jim Lacy, and Chris Morales.

More than a shared cleanroom facility, KNI is also where I found friends from other research groups on campus, especially students from the Yariv, Painter, Heath, Roukes, Atwater, and Schwab labs. They showed me their fabrication tricks, advised me based on their lab experience, and kept

the cleanroom a lively and friendly place. A grateful shout out to Derrick Chi, who taught me e-beam alignment on the Leica EBPG, a technique that immensely opened up the types of devices I could make.

But then I would not have thought of going to graduate school at all if it was not for several wonderful mentors at Cornell University. Prof. Harold Craighead let me join his group when I was a clueless freshman and gave me all the freedom to play in lab. His group was my first exposure to the wonderland of research. Drs. Rob Ilic and Keith Aubin guided me through my senior project, patiently teaching me every detail of the fabrication and measurement techniques for our MEMS resonators. Rob was also my supervisor at the Cornell Nanofabrication Facility (CNF), who trained me on most of the equipment there and assigned me projects from which I began gathering semiconductor fabrication experience. Prof. George Malliaras suggested that I seek out research opportunities as early as freshman year. Prof. Lois Pollack was always there when I needed help big or small, from showing me how to find relevant papers in online databases before the days of Google Scholar to earnestly helping me with graduate school applications.

A tip of the hat to my good friends Gregory Kimball, Andrej Svorencik, Douglas Tham, Sherlynn Hoon, Michael Kong, Florian Quarré, Sushant Jadhav, and Noah Gaspar for the fun times and constant encouragement during my graduate school years.

Many thanks goes to my boyfriend Christopher Henry, who cheered me along during the days of thesis writing and job search, who calmed my frustration after a bad day in lab, and whose strong work ethic in his own research is a constant motivation to me.

This thesis is dedicated to my parents. They have sacrificed much to afford me the best education and opportunities, and have always shown me unwavering support and confidence. I am everyday grateful for their love.

Abstract

We present design and experimental work toward building room temperature, continuous-wave (CW) lasers with a cavity that confines light to a volume of $\leq (\lambda/n)^3$. We begin with the mechanisms of strong optical confinement using dispersive metals and photonic crystals. Finite-difference time-domain methods (FDTD) are used to simulate the behavior of electromagnetic fields in the cavity; fast Fourier transform from FDTD-generated near-field data calculates the far-field radiation pattern from the microcavity laser.

We then present our investigations into designs where metals are incorporated into microdisk and photonic crystal optical cavities to curb or redirect radiation loss. The significant effects of boundary conditions and substrate feedback on far-field radiation directionality are studied. We evaluate the threshold gain required to achieve room temperature lasing in these metallo-dielectric cavities.

While studying the confinement mechanism of photonic crystals on metal substrate, it became clear that room temperature lasing can be achieved in optically-thick photonic crystal cavities, where the thicker semiconductor layer would give us more freedom in designing the vertical p-i-n doping profile within, for a less resistive and leaky electrical path for current injection operation. We fabricate and demonstrate single-mode room temperature lasing by optical pumping in an optically-thick single-defect cavity.

We move on to present our design and characterization of coupled-cavity photonic crystal lasers operating with CW, high output power, and directional emission. Single-mode stable emission with output power on the order of 10 μW and linear polarization was achieved. Moreover, we switched from the commonly used InGaAsP quantum well material to the lesser-known InAsP quantum wells

in InP cladding, and found that the large band-edge offset between InAsP and InP made a world of difference in achieving high power operation despite the large thermal resistance in the device.

For a microcavity laser with directional radiation, Purcell-enhanced spontaneous emission, and diminished effects due to feedback from surrounding structures such as the substrate, nanobeam photonic crystal lasers are analyzed, fabricated, and characterized. Despite thermal resistance an order of magnitude higher than their 2D counterparts, quasi-CW operation with a soft threshold turn-on was achieved.

Much work was done to optimize fabrication techniques in order to realize the optical cavity designs with little fabrication error. We detail the high-contrast hydrogen silsesquioxane (HSQ) electron-beam lithography and deep vertical dry etch procedures especially developed for this work.

Lastly, related projects on nonlinear silicon photonic devices are presented. Synthetic nonlinear polymer is integrated on to the silicon photonic platform to achieve low half-wave voltage electro-optic modulation. Causes and magnitude of the nonlinear loss particular to silicon waveguides with sub-μm^2 cross-section are evaluated.

Contents

List of Figures

List of Tables

List of Symbols and Abbreviations

$\Delta\lambda_l$	Laser linewidth
α	Waveguide linear loss coefficient
β	Spontaneous emission coupling efficiency
β_{TPA}	Two-photon absorption coefficient
η_d	Differential quantum efficiency
η_i	Internal efficiency of a laser, i.e. the fraction of injected carriers that reach the active region
γ_c	Collision frequency in the Drude-Sommerfeld model
κ	Extinction coefficient, imaginary part of the complex index of refraction
λ_l	Microlaser device emission wavelength
λ_p	Pump laser wavelength
μ_e	Electron mobility
μ_h	Hole mobility
ω_p	Frequency of the pump laser
ω_l	Frequency of the lasing mode
ω_p	Plasma frequency
σ_{FCA}	Free carrier absorption cross-section

τ_e Electron capture time due to trap-assisted recombination

τ_h Hole capture time due to trap-assisted recombination

τ_{FCA} Effective free carrier lifetime, in silicon photonics

τ_{ph} Photon lifetime in a cavity

τ_{sp} Spontaneous emission lifetime

ε_0 Permittivity of free space

ε_d Relative permittivity of a dielectric

ε_m Dielectric function of a metal

A Surface recombination coefficient

A Waveguide cross-section

a Photonic crystal lattice constant

A_{eff} Waveguide effective area

C Auger recombination coefficient

CAIBE Chemically-assisted ion beam etch

CCD Charge-coupled device

CMOS Complementary metal-oxide-semiconductor

CW Continuous-wave

DBR Distributed Bragg reflector

e Elementary charge

EDFA Erbium-doped fiber amplifier

EO Electro-optic (effect/modulation)

EUV Extreme ultraviolet

FCA Free carrier absorption

FDTD Finite-difference time-domain simulation

FFT Fast Fourier transform

F_p Purcell factor

FSR Free spectral range

FT Fourier transform

g Optical gain per unit length in a laser's gain medium

g_0 Optical gain coefficient

g_{th} Threshold gain, $g_{th} = g(N_{th})$

h Gap size between the active semiconductor layer and the underlying substrate

HH Heavy hole

HSQ Hydrogen silsesquioxane

I Electrical current

ICP-RIE Inductively-coupled plasma reactive ion etch

IPA Isopropanol

ITO Indium tin oxide

$\mathbf{j}$ Current density

L Optical power

LCA Lightwave component analyzer

LH Light hole

L_{in} Input optical power

L-L curve Light-in light-out curve

L_{out} Output optical power

m Azimuthal mode number of a disk resonator

m_0 Rest mass of an electron

m^*_{ce} Conductivity effective mass of electrons

m^*_{ch} Conductivity effective mass of holes

MIBK Methyl isobutyl ketone

MZM Mach-Zehnder modulator

N Carrier density

n Index of refraction, $n \in \mathbb{R}$

$\hat{n}$ Complex index of refraction

N_{e^-} Electron density

N_{h^+} Hole density

N_i Intrinsic carrier density

N_{th} Threshold carrier density

N_{tr} Transparency carrier density

OSA Optical spectrum analyzer

P Photon density

p Radial mode number of a disk resonator

PBG Photonic bandgap

PEC Perfect electric conductor

PECVD Plasma-enhanced chemical vapor deposition

PMMA Poly(methyl methacrylate)

Q Quality factor of a resonator

q Axial mode number of a disk resonator

Q_{abs} Quality factor due to material absorption loss

Q_{rad} Quality factor due to radiation loss

Q_{tot} Total quality factor

R Photonic crystal air-hole radius

R_{Auger} Auger recombination rate per volume

RF Radio frequency

RIU Refractive index unit

R_{nr} Number of non-radiative recombinations per volume per time

RPM Revolutions per minute, a measure of rotation speed

R_{sp} Number of spontaneous emission recombinations per volume per time

R_{sr} Surface recombination rate per volume

R_{st} Number of stimulated emission recombinations per volume per time

SEM Scanning electron microscope

SO Split-off (energy band)

SOI Silicon-on-insulator

SPA Single-photon absorption

SPP Surface plasmon polariton

T Semiconductor active layer slab thickness, therefore it is also the disk cavity thickness or the photonic crystal slab thickness

TCE Trichloroethylene

T_g Glass transition temperature of a polymer

TIR Total internal reflection

TMAH Tetramethylammonium hydroxide

TPA Two-photon absorption

U_E Electric field energy in an optical resonator

u_E Electric field energy density in an optical resonator

U_{EM} Total electromagnetic energy in an optical resonator

U_M Magnetic field energy in an optical resonator

u_M Magnetic field energy density in an optical resonator

V_a Volume of the active region in a laser cavity

VCSEL Vertical-cavity surface-emitting laser

VECSEL Vertical-external-cavity surface-emitting laser

V_{eff} Effective mode volume of an optical resonant mode

v_g Group velocity

V_π Half-wave voltage

v_{sr} Surface recombination velocity

W Beam width of a nanobeam photonic crystal

Chapter 1

Introduction

The fundamental motivation for this thesis work was the fun of playing with photons, afforded by the rich physics of electromagnetics [1, 2]. Fortunately, the fun also has real world device applications. Much of the work in the field of photonics finds use in telecommunication and more recently (quantum) computing, from optical modulators to single photon sources.

The major part of this work involves the design, fabrication, and characterization of semiconductor lasers, whose resonant cavity confines light into a volume of $\sim(\lambda/n)^3$. Interest in wavelength-scale confinement of light is not just for the simple reduction of device footprint on-chip, but for the implications of E. M. Purcell's prediction that spontaneous emission lifetime of an emitter can be changed by its environment [3]. The phenomenon is now known as the Purcell effect, and the spontaneous emission enhancement factor is the Purcell factor, defined as the ratio of emission lifetimes in bulk medium and in the cavity. On one hand, microcavities that confine light to dimensions comparable to the emission wavelength are well-suited to studying Purcell effect. On the other hand, enhanced spontaneous emission that is efficiently coupled to the lasing mode in such a cavity is predicted to lower the laser threshold and increase modulation speed [4, 5, 6].

Wavelength-scale confinement of light with high quality factor Q has been realized using periodic dielectric structures. Early cavities were formed between two sets of Bragg reflectors, such as those used in the vertical-cavity surface-emitting laser (VCSEL) [7], and in its smaller relative, the micropillar laser [8]. After the concept of two- and three-dimensional (2D and 3D) photonic crystals were proposed, full 3D photonic crystals proved to be difficult to fabricate for optical wavelengths;

instead a combination of total internal reflection (TIR) and photonic crystals are implemented in planar photonic crystal slabs or strip waveguides to achieve high Q and low optical mode volume [9]. At the same time, microdisk cavities proved to be another geometry for strong optical confinement. Soon, spontaneous emission enhancement was measured in wavelength-scale cavities [10, 11, 12, 13], and lasers were built, though still with a pronounced threshold [14, 15, 16, 17]. In time, a few groups began demonstrating lasing with Purcell enhancement [18, 19]. Recently, metal as an optical material encountered renewed interest among researchers of wavelength-scale lasers, because of its ability to achieve sub-diffraction limit photon confinement. Metallo-dielectric lasers with unprecedented small device sizes were reported [20], but limited to low-temperature operation due to metallic absorption loss. The field of plasmonic lasers was still young.

Arriving on the heel of these developments in the semiconductor laser field when I began graduate school and prompted by yet-to-be answered questions in building small lasers with the benefits of Purcell enhancement, we sought to make a few contributions of our own.

First, we looked at ways to incorporate metals into optical cavities to improve device properties that could not be achieved with dielectrics alone. We evaluated the use of metal cladding to curb radiation loss and bring up the Q of sub-wavelength disk resonators despite ohmic loss in room temperature metals. Although a metal thickness beyond the skin depth is sufficient to achieve optical confinement, we found that the far-field emission directionality depends very much on the extent of the metal cladding as well as other potential structures nearby. Moving on to photonic crystal cavities, we investigated the integration of a metal substrate to serve as a path of both heat and electrical conduction, and to eliminate the complication of substrate feedback that accompanies most suspended-slab photonic crystal lasers. While studying the confinement mechanism of photonic crystals on metal substrate, it became clear that sufficiently high Q can be achieved in optically-thick photonic crystal cavities to build a laser. Having the freedom to increase the photonic crystal slab thickness potentially enables us to better design the vertical p-i-n doping profile within the slab for electrically, instead of optically, pumped lasers. We proceeded to fabricate and demonstrate single-mode room temperature lasing from optically-thick single-defect cavities.

Then we switched gears and focused on designing wavelength-scale lasers for room temperature, continuous-wave (CW), high output power, and directional emission. We succeeded with single-mode lasing from coupled-cavities that have a stable output power up to the order of 10 μW with a mostly linearly polarization within a relatively small divergence angle. Moreover, we switched from the commonly used InGaAsP quantum well material to the lesser-known InAsP quantum wells in InP cladding, and found that the large band-edge offset between InAsP and InP made a world of difference in achieving high power operation despite large thermal resistance in the device.

Thus far, we worked with planar semiconductor slabs. Photonic crystal cavities with periodic structures extending in two dimensions suffer from substrate feedback, where the semi-reflective substrate acts as an external cavity and significantly changes Q as well as far-field radiation patterns. Moreover, the coupled-cavity devices have effective optical mode volumes too large to exhibit Purcell enhancement. Therefore, we designed and fabricated nanobeam photonic crystal cavities, where periodic air-holes are drilled into a suspended single-mode waveguide. These devices have a thermal resistance an order of magnitude higher than their 2D counterparts; however, we still observed quasi-CW operation with a soft threshold turn-on and directional emission that was barely influenced by substrate feedback.

To realize all of the designs outlined above, we worked out techniques to fabricate devices with geometries faithful to the design parameters. High-contrast electron-beam lithography using a thick layer of the etch resistant hydrogen silsesquioxane (HSQ) resist and deep vertical dry etch procedures were especially developed, so we could make the aforementioned devices with little fabrication error.

This thesis is organized according to the workflow in laser making. Beginning with optical cavity design, Chapter 2 outlines the concepts of plasmonic and photonic crystal reflectors and the numerical methods used through this work. In Chapter 3, we present details of the laser cavity designs in this work. The next step is fabricating the devices in InGaAsP or InAsP/InP epitaxial quantum well materials. Our experience and the techniques we developed are summarized in Chapter 4. Characterization of the finished devices is presented in Chapter 5.

But then, photonics is a diverse field. Interesting as lasers are, I could not help trying my hand

at related semiconductor photonic devices too. Our work in nonlinear silicon photonics involves the development of low operating voltage electro-optic modulators on-chip with the integration of synthetic electro-optic polymers. Moreover, we noticed significant nonlinearity in the absorption loss of a laser signal traveling through a simple silicon strip waveguide, and thus proceeded to study the cause and magnitude of this nonlinear loss. We present the details of the silicon photonics work in Chapter 6.

At the conclusion of this thesis in Chapter 7, we summarize our contribution and look out to the next steps in developing wavelength-scale, Purcell-enhanced microlasers.

Chapter 2

Design of wavelength-scale optical cavities

Established cavity designs for commercial semiconductor lasers are mostly based on Fabry-Pérot etalons for edge- or surface-emission with or without external-cavity. Cleaved semiconductor surfaces or distributed Bragg reflectors (DBR) that consist of periodic dielectric structures form the mirrors of the Fabry-Pérot. Similar to the trend of miniaturization in integrated electronics, there is a quest to shrink the size of semiconductor lasers, in order to pack more devices on less material and in hope of modifying the laser efficiency with control of spontaneous emission in tiny cavities [3, 21, 22]. Research labs have since used micro-toroid, microdisk, vertical-cavity, and photonic crystal cavities to confine light into smaller and smaller volumes. In this chapter, we discuss how to design and achieve strong light confinement in terms of confinement mechanisms and numerical modeling methods. After that, we relate the cavity designs to the threshold gain required for lasing.

2.1 Mechanisms of photon confinement

Two figures of merit are used to quantify a cavity design: the quality factor Q as a measure of the cavity's lossiness and the mode volume V_{eff} for how small a volume the photons are concentrated into. Q is defined as [23]

$$Q = \omega \times \frac{\text{total electromagnetic energy stored by the resonator}}{\text{power dissipated by the resonator}} = \frac{\omega U_{EM}(t)}{P(t)} \tag{2.1}$$

where ω is the frequency of the mode. In numerical simulations, we can calculate Q by measuring the slope of the exponential decay of the electromagnetic energy stored in the optical cavity,

$$U_{EM}(t) = U_{EM}(0) \exp\left[-\frac{t}{\tau_{ph}}\right] = U_{EM}(0) \exp\left[-\frac{\omega}{Qt}\right] \tag{2.2}$$

using the relation $Q = \omega\tau_{ph}$. τ_{ph} is the photon lifetime in the cavity. $U_{EM}(t)$ is the sum of electric field energy $U_E(t)$ and magnetic field energy $U_M(t)$, each of which is defined in terms of their respective energy density functions $u_E(\mathbf{r}, t)$ and $u_M(\mathbf{r}, t)$

$$U_E(t) = \int_V d^3\mathbf{r}\ u_E(\mathbf{r}, t) \tag{2.3}$$

$$U_M(t) = \int_V d^3\mathbf{r}\ u_M(\mathbf{r}, t) \tag{2.4}$$

Because we are going to concern with metallic reflectors, which have dispersive dielectric functions, we especially note that the electric and magnetic field energies are defined as follows [24, 25]

$$u_E(\mathbf{r}, t) = \frac{\varepsilon_0}{2} \Re\left\{\frac{d[\omega\varepsilon(\omega)]}{d\omega}\right\} \langle \mathbf{E}(\mathbf{r}, t) \cdot \mathbf{E}(\mathbf{r}, t)\rangle_T \tag{2.5}$$

$$u_M(\mathbf{r}, t) = \frac{\varepsilon_0}{2} \Re\left\{\frac{d\varepsilon(\omega)}{d\omega}\right\} \langle \mathbf{E}(\mathbf{r}, t) \cdot \mathbf{E}(\mathbf{r}, t)\rangle_T \tag{2.6}$$

$\langle ... \rangle_T$ denotes time average over one optical cycle. In the case where $\mathbf{r}$ lies in an ordinary dielectric media with a non-dispersive dielectric constant, the above two equations simplify to the familiar forms

$$u_E = u_M = \frac{\varepsilon_0\varepsilon_d}{2} \langle \mathbf{E}(\mathbf{r}, t) \cdot \mathbf{E}(\mathbf{r}, t)\rangle_T \tag{2.7}$$

where ε_d is the dielectric material's relative permittivity or dielectric constant. With the electromagnetic energies thus defined, we adopt in this work the cavity quantum electrodynamics definition of V_{eff},

$$V_{eff} = \frac{U_{EM}(t)}{\max\{u_E(\mathbf{r}_{max}, t) + u_M(\mathbf{r}_{max}, t)\}} \tag{2.8}$$

where $\mathbf{r}_{max}$ is the position where the sum of u_E and u_M is at the maximum.

To achieve strong confinement of light, one method is to use TIR [26], which can theoretically exhibit perfect reflectivity. Disk and toroid resonators both operate on this principle. However, perfect TIR is only possible for plane waves with a narrow range of wave vectors, not when cavity size approaches wavelength-scale so that the momentum space (i.e. k-space) field distribution is much broadened. Indeed, microtoroid cavities can reach Qs of 10^8 with a $V_{eff} > 100(\lambda/n)^3$; microdisks have Qs of 10^6 with V_{eff} of around $6(\lambda/n)^3$ [9]. Yet as cavity size shrinks, light experiences only partial reflection at the dielectric-air interface; radiation loss dominates and limits the maximum achievable Q [27]. On the other hand, carefully designed reflectors surrounding a cavity, such as periodic dielectric structures or metal mirrors, can achieve much higher Q with $V_{eff} < (\lambda/n)^3$. We now proceed to elaborate on their optical confinement mechanisms.

2.1.1 Metals as plasmonic materials and reflectors

Metals are natural reflectors due to their large negative real part of dielectric constant $\Re\{\varepsilon_m\}$ in a wide range of telecommunication frequencies. For microwave to far-infrared frequencies, only a negligible fraction of the electromagnetic waves penetrates into the metal; therefore, metals are often approximated as perfect conductors. At the optical frequencies of NIR and visible range, field penetration increases, leading to increased dissipation. At ultraviolet frequencies, however, metals acquire dielectric-like characteristics and allow the propagation of electromagnetic waves with varying degrees of attenuation. At NIR and visible wavelengths, noble metals such as gold and silver are among the most commonly used materials, as they have large negative $\Re\{\varepsilon_m\}$ and relatively low $\Im\{\varepsilon_m\}$, which represents optical loss. Their $\Re\{\varepsilon_m\}$ and $\Im\{\varepsilon_m\}$ from $\lambda = 500 \sim 2000$ nm are plotted in Figure 2.1. The data is taken from [28].

2.1.1.1 The Drude-Sommerfeld model of optical dispersion

The dispersive character of metals is often treated using the Drude-Sommerfeld model, which regards metals as a classical gas of N electrons in a diffusive motion against a background of ion cores

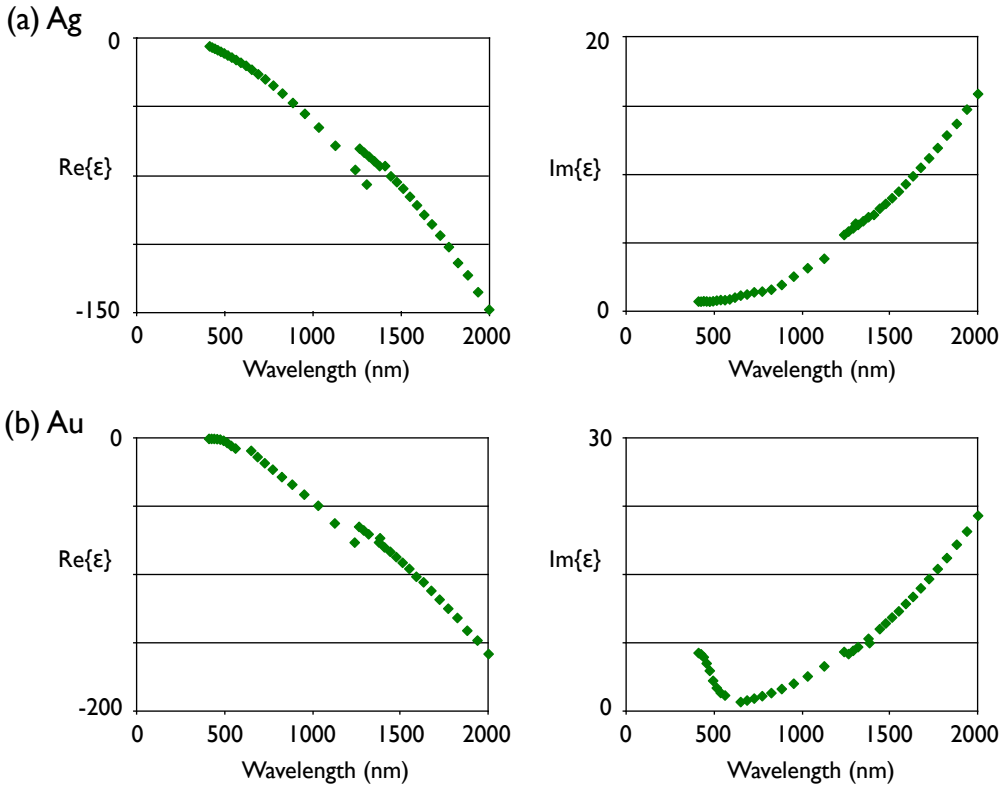

Figure 2.1: Dispersion properties of (a) silver and (b) gold from $\lambda = 500$ to 2000 nm

[29, 30]. The electron gas is modeled using kinetic theory of a neutral dilute gas. Several simplifying assumptions are made. First, akin to kinetic theory, electrons experience instantaneous collision events that abruptly change their velocity. In the case of a metal, this is attributed to electrons colliding into the much heavier ions, instead of electron-electron collision. Second, interactions other than the collisions are negligible. Third, the probability of an electron undergoing a collision within an infinitesimal time interval dt is given by dt/τ, where τ is the electron relaxation time. Fourth, electrons achieve thermal equilibrium with their surroundings only through collisions. In other words, when the external $\mathbf{E}$ field is removed, the electron gas system relaxes to equilibrium, that is, zero average momentum $\langle \mathbf{p} \rangle = 0$, with an average relaxation time τ. Lastly, the electrons have an *effective* mass m and oscillate in response to the external electric field $\mathbf{E}$. In this picture, the rate equation is

$$\frac{d\langle \mathbf{p} \rangle}{dt} = -\frac{\langle \mathbf{p} \rangle}{\tau} - e\mathbf{E} \tag{2.9}$$

When the metal is in the presence of optical irradiation with a time-harmonic $\mathbf{E}$ field

$$\mathbf{E}(t) = \Re\left\{\mathbf{E}(\omega)e^{-i\omega t}\right\} \tag{2.10}$$

the steady-state solution of $\mathbf{p}(t)$ takes the form

$$\mathbf{p}(t) = \Re\left\{\mathbf{p}(\omega)e^{-i\omega t}\right\} \tag{2.11}$$

Substitute Equations (2.11) and (2.10) into (2.9), we obtain

$$-i\omega\mathbf{p}(\omega) = -\frac{\mathbf{p}(\omega)}{\tau} - e\mathbf{E}(\omega) \tag{2.12}$$

Current density in the metal is $\mathbf{j}(t) = -Ne\mathbf{p}/m$, thus

$$\mathbf{j}(\omega) = \frac{(Ne^2/m)\mathbf{E}(\omega)}{(1/\tau) - i\omega} \tag{2.13}$$

We can rewrite the above expression in the form of Ohm's law $\mathbf{j}(\omega) = \sigma\mathbf{E}(\omega)$, and obtain the frequency-dependent conductivity

$$\sigma(\omega) = \frac{(Ne^2\tau/m)}{1 - i\omega\tau} = \frac{Ne^2\tau}{m}\frac{1 + i\omega\tau}{1 + \omega^2\tau^2} \tag{2.14}$$

By constructing the Drude-Sommerfeld model, we want to apply the results to the propagation of electromagnetic field in a metal, but we run into two complications in doing so. First, electromagnetic fields come with coupled **E** and **H** fields, and we have only included **E** field in our derivation. Second, Equation (2.14) assumes a spatially uniform **E** field, but fields in an electromagnetic wave vary in both space and time.

To address the first complication, we look at the magnitude of electron motion due to the **H** field. Adding the **H** field contribution to Equation (2.9), we have

$$\frac{d\langle\mathbf{p}\rangle}{dt} = -\frac{\langle\mathbf{p}\rangle}{\tau} - e\mathbf{E} - \frac{e\mathbf{p}}{mc} \times \mathbf{H} \tag{2.15}$$

The additional **H** term is smaller than the **E** term by a factor of ν/c, where $\nu = j/Ne$ is the magnitude of mean electron velocity. Typically, the **H** field contribution is 10^{-10} of that of the **E** field, thus it is negligible [29].

The second complication means that we need to make one more assumption in our analysis in order to use the Drude-Sommerfeld to study the effects of optical waves in a metal. If the electric field does not vary appreciably over the distance of several electron mean free paths, then the current density at any particular spatial position $\mathbf{r}$ is still correctly given by $\mathbf{j}(\mathbf{r}, \omega) = \sigma(\omega)\mathbf{E}(\mathbf{r}, \omega)$. More simply, the model applies when the optical wavelength is much greater than the electron mean free path in the metal, a condition satisfied by NIR and visible light.

Now we may turn our attention to apply Equation (2.14) to Maxwell's equations,

$$\nabla \cdot \mathbf{E} = \frac{1}{\varepsilon_0}\rho \tag{2.16}$$

$$\nabla \cdot \mathbf{B} = 0 \tag{2.17}$$

$$\nabla \times \mathbf{E} = -\frac{\partial \mathbf{B}}{\partial t} \tag{2.18}$$

$$\nabla \times \mathbf{B} = \mu_0 \mathbf{J} + \mu_0 \varepsilon_0 \frac{\partial \mathbf{E}}{\partial t} \tag{2.19}$$

Assume the fields have a harmonic time dependence $e^{i\omega t}$, we cast Maxwell's equations into the wave equation, and rewrite $\mathbf{J}$ using $\mathbf{J} = \sigma \mathbf{E}$,

$$\nabla \times (\nabla \times \mathbf{E}) = -\nabla^2 \mathbf{E} = -i\omega \nabla \times \mathbf{B} = -i\omega\mu_0 \mathbf{E} + \mu_0 \varepsilon_0 \omega^2 \mathbf{E} \tag{2.20}$$

$$-\nabla^2 \mathbf{E} = \frac{\omega^2}{c^2} \left(1 - \frac{i\sigma}{\omega \varepsilon_0}\right) \mathbf{E} = \frac{\omega^2}{c^2} \varepsilon(\omega) \mathbf{E} \tag{2.21}$$

The dielectric function derived from the Drude-Sommerfeld model becomes

$$\varepsilon(\omega) = \left(1 - \frac{i\sigma}{\omega \varepsilon_0}\right) = 1 - \frac{\omega_p^2}{\omega^2 + i\omega/\tau} = 1 - \frac{\omega_p^2}{\omega^2 + i\omega\gamma_c} \tag{2.22}$$

where $\omega_p^2 = Ne^2 m/\varepsilon_0$ is the bulk plasma frequency and $\gamma_c = 1/\tau$ is the collision frequency. This expression only includes dielectric function due to the electron gas in the ideal kinetic model, thus $\varepsilon \to 1$ when $\omega \gg \omega_p$. However, this is not the case with real metals. The contribution of the background network of ion cores need to be added, which is in the form of a constant offset ε_∞. Thus we finally arrive at the Drude-Sommerfeld description of optical dispersion in metal

$$\varepsilon(\omega) = \varepsilon_\infty - \frac{\omega_p^2}{\omega^2 + i\omega\gamma_c} \tag{2.23}$$

We fit the optical properties data from [28] to Equation (2.23). The Drude-Sommerfeld fitted values for silver and gold are shown in Table 2.1 [31].

Table 2.1: Drude-Sommerfeld fit of dielectric functions of silver and gold at room temperature

Material	Wavelength range	ε_∞	ω_p	γ_c
Silver	$1260 \sim 2000$ nm	1.722	1.155×10^{16}	1.108×10^{14}
	$375 \sim 1240$ nm	3.9943	1.329×10^{16}	1.128×10^{14}
Gold	$1250 \sim 1800$ nm	1	1.207×10^{16}	1.362×10^{14}
	$650 \sim 1250$ nm	12.99	1.453×10^{16}	1.109×10^{14}

2.1.1.2 Loss channels in metallo-dielectric cavities

In most metallic optical cavities, the two main channels of loss are radiation and material absorption. Their relative contribution to device Q is given by

$$\frac{1}{Q_{tot}} = \frac{1}{Q_{rad}} + \frac{1}{Q_{abs}} \tag{2.24}$$

where Q_{tot} is the total device Q-factor, and Q_{rad} and Q_{abs} are the Q-factors due to radiation loss and material absorption in the metal[1], respectively. The amount of radiation loss also represents the signal we can collect when the cavity is lasing. To calculate the power absorbed in the Drude metal, the following volume integration is carried out [1, 32]

$$P_{abs}(t) = \int_V d^3\mathbf{r}\ \omega\varepsilon_0 \Im\left\{\varepsilon_m(\omega)\right\} \langle \mathbf{E}(\mathbf{r},t) \cdot \mathbf{E}(\mathbf{r},t) \rangle_T \tag{2.25}$$

and from Equation (2.1) $Q_{abs} = \omega U_{EM}(t)/P_{abs}(t)$. Similarly, $Q_{rad} = \omega U_{EM}(t)/P_{rad}(t)$, where $P_{rad}(t)$ is given by

$$P_{rad}(t) = \oint_S d^2\mathbf{r} \cdot \langle \mathbf{E}(\mathbf{r},t) \times \mathbf{H}(\mathbf{r},t) \rangle_T \tag{2.26}$$

Alternatively, Equation (2.24) can be used to calculate of one of the Q components when the other one is known.

2.1.2 Bragg reflectors and photonic crystals

If metals are natural mirrors, artificial reflectors can be made from periodic dielectric structures, whose periodicity or lattice constant a is on the scale of the optical wavelength. These periodic

[1] Material absorption in dielectrics is negligible in comparison to the metals.

dielectric structures are often called *Bragg reflectors* when the periodicity extends in one dimension or *photonic crystals* for periodicity in two or three dimensions. Studies of wave propagation in periodic media extends at least as far back in history as Lord Rayleigh's examination of the quarter-wave stack, which consists of alternating layers of transparent dielectrics with contrasting refractive indices [33, 34]. If we plot the dispersion relations of light propagating across the dielectric stack, forward propagation is forbidden for a certain optical frequency range, because multiple reflections at each dielectric interface interfere destructively at those frequencies. We can then think of this forbidden frequency range as a *photonic bandgap* (PBG), analogous to the electronic bandgap from the periodic potential within a crystal lattice. Periodic dielectric stacks have been used as reflectors to confine electromagnetic waves in microwave [35, 36, 37] and optical frequencies [38, 39, 40]. More recently, Yablonovitch and John both proposed the extension of periodic dielectric reflectors to two and three dimensions [41, 42]. Ideal 3D photonic crystals can achieve a *complete* PBG in all propagation directions, but they are very difficult structures to make [43, 44]. The highest Q achieved from 3D photonic crystal cavities is about 9000 so far [45, 46]. 2D PBG can be realized in photonic crystals patterned in a high-index dielectric layer using conventional planar lithography and etching techniques with great control over fabrication error. Light confinement in the third dimension is achieved by TIR. This idea of using TIR and PBG in combination is extended to constructing photonic crystal cavities in a single-mode waveguide with 1D symmetry [47, 48].

Design of photonic crystal cavities begins with bandgap engineering. The dispersion relations of a nanobeam and a 2D slab photonic crystal are plotted in Figure 2.2. Optical frequencies where propagation in the medium is inhibited are labeled as the PBG. The target resonant wavelength λ should be somewhere within the PBG. In the case of Figure 2.2(a), $a = 480$ nm, $\omega = 0.31(2\pi c/a)$ for $\lambda = 1550$ nm; in Figure 2.2(b), $a = 420$ nm, $\omega = 0.27(2\pi c/a)$. Filling in one or more consecutive air-holes creates a defect cavity. However, maximizing the PBG size and choosing a defect cavity size that results in a precisely mid-gap resonance at the target wavelength do not give a high Q. Most early photonic crystal cavities thus constructed have Qs of $<$1000.

An import consequence of combining TIR and PBG for optical cavities is that the band diagram of

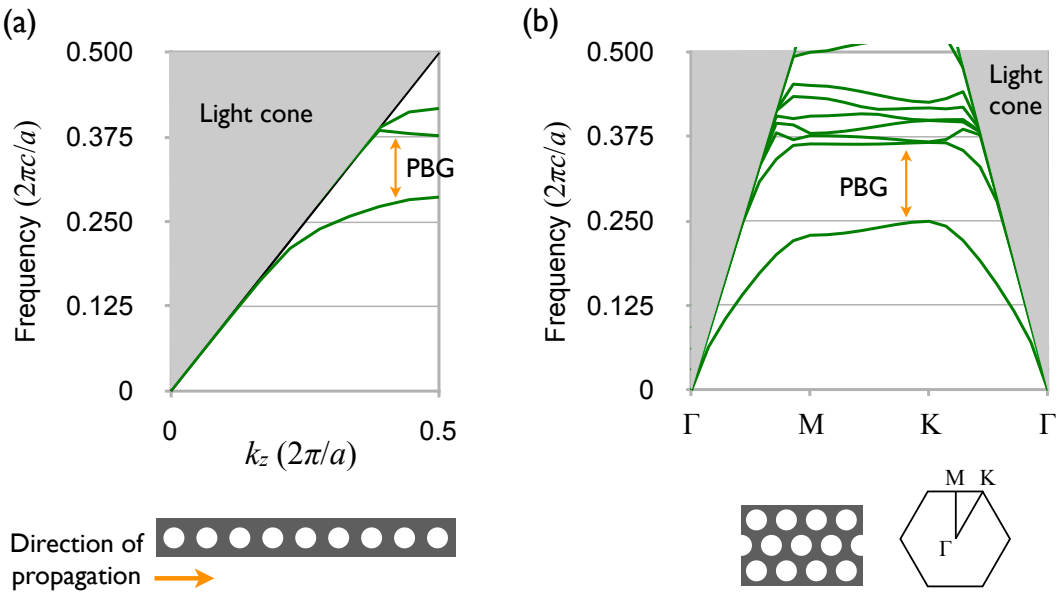

Figure 2.2: Light cone and bandgap for nanobeam and 2D slab photonic crystals: (a) nanobeam; (b) 2D slab. Gray shade indicates the light cone.

the slab or waveguide has a light cone, a region on the ω-k plane that corresponds to radiation modes, whose propagation is not tethered to the photonic crystal. The main reason for low Q-factors from unmodified defect cavities is not because of incomplete reflection by the photonic crystal reflectors, but due to the resonant mode coupling to radiation modes in the light cone. This is especially clear in the momentum space picture [49]. Using the L3 cavity[2] as an example, Akahane and colleagues showed that the lowest order resonant mode from an unmodified cavity has overlap with the light cone in k_x-k_y momentum space. By shifting the nearest air-holes in the longitudinal direction, the momentum space distribution of the fundamental mode moves away from the light cone, and Q increases dramatically from a couple thousand to 45,000. Similar design methods have been applied to nearest air-hole tuning in other cavities—including H0 [50], H1 [51], and other LNs formed in the triangular lattice—with equally effective Q optimization.[3] For example, hexapole mode in an H1 cavity can have a theoretically calculated Q in excess of 2×10^6 with mode volume of $\sim(\lambda/n)^3$ [52]. The same cavity design was experimentally implemented and showed a Q of 3.65×10^5 [53].

[2]L3 cavity is formed in a triangular lattice photonic crystal slab by removing three consecutive air-holes.

[3]H0 is formed by shifting two adjacent air-holes away from each other. H1 denotes cavities formed by the removal of a single air-hole. An LN cavity consists of removing N consecutive air-holes in a row.

The same concept also applies to photonic crystals with 1D symmetry, such as the one shown in Figure 2.2(a), but now with greater freedom. One is not limited to tuning only the nearest air-holes, instead a slowly-varying taper can be built into the N air-holes leading up to the defect cavity. Many design theories have been proposed, including Bloch-wave engineering to increase the modal reflectivity [54, 55] or local gap modulation [56, 57]. The tapering may be introduced by slowly narrowing or widening the nanobeam width, or tapering the air-hole size without disturbing the lattice constant, or changing both the lattice constant and air-hole radius. The tapering itself can be linear [58], quadratic [59], or parabolic [60]. Some of the highest Q and Q/V at optical wavelengths have been achieved with 1D symmetric geometries—numerical simulations predict Q of $>10^8$ with a V_{eff} of just over $(\lambda/n)^3$ in passive silicon cavities [53, 59]; experimental results demonstrated $Q \approx 1.3 \times 10^6$ [61].

2.1.3 Functional similarities between metals and photonic crystals

It would seem that metals and photonic crystals are very different animals—the former reflect light due to the materials' large negative real part of the dielectric function, the latter reflect by the PBG as a result of periodic dielectric structures. The same material property that makes metals reflective also leads to other interesting consequences that have captured the interest of the optics research community in recent years, namely, surface plasmon polaritons (SPP) [62], metallic nano-antennas with hot spots of extremely concentrated light [63], and negative refractive index meta-materials [64, 65]. However, all of these metallic phenomena have counterparts in photonic crystals made of only lossless dielectrics. Surface modes can occur at the interface of air[4] and 2D or 3D photonic crystals with dispersion relations and evanescent mode profiles similar to those of SPP, where the E-field decays evanescently into both the photonic crystal and air [66, 67]. Chang and colleagues designed photonic crystal cavities with a nanoslot in the middle that concentrate light like a nano-antenna [68]. Lastly, Notomi proposed that, just like metallic (meta-)materials with engineered band structures, negative refractive index materials can be realized by band engineering of photonic

[4] Or other isotropic low-index dielectric media.

crystals [69].

The big difference between metals and photonic crystals is in essence the trade-off between size and lossiness. Metals are known to obtain their bulk plasmonic properties even when they are tiny nuggets of <10 nm across [70]. However, their positive imaginary part of the dielectric function means room temperature metallic devices are accompanied by non-negligible ohmic loss. In contrast, photonic crystals are made of lossless dielectrics, but necessarily have dimensions on the order of a few wavelengths, since at least several lattice periods are needed to achieve the collective band structure and PBG [44, 66].

2.1.4 Purcell factor calculation

The cavity quantum electrodynamics definition of Purcell factor is given by [11]

$$F_p = \frac{3Q}{4\pi^2 V_{eff}} \left(\frac{\lambda}{n}\right)^3 \tag{2.27}$$

In quantum well lasers, where the spectral and spatial alignment of the emitter and the resonant mode is usually imperfect, a more realistic estimation of the same figure of merit is [19]

$$F_p = \frac{a_p}{2\pi^2 V_{eff}} \left(\frac{\lambda}{\Delta\lambda}\right) \left(\frac{\lambda}{n}\right)^3 \tag{2.28}$$

where a_p is the normalized average projection component of electric dipoles on the electric field of the laser mode and $\Delta\lambda$ is the wider spectral linewidth between the homogeneous broadening and the cavity resonance.

2.1.5 Threshold gain for lasing

Based on the cavity Q, we can determine the threshold material gain g_{th} required to achieve room temperature lasing, given by [25, 71, 72]

$$g_{th} = \frac{\omega_0}{Q v_{g,a}(\omega_0) \Gamma_E} \tag{2.29}$$

where ω_0 is the resonant frequency and $v_{g,a}(\omega_0) \approx c/n_{g,a}(\omega_0)$ is the material group velocity. Γ_E is the energy confinement factor that quantifies the extent of overlap between the optical mode and the regions of active gain medium such as quantum wells or quantum dots.

$$\Gamma_E = \frac{\int_{V_a} \frac{\varepsilon_0}{4}\{\varepsilon_{g,a}(\omega_0) + \Re[\varepsilon_a(\omega_0)]\}|\mathbf{E}|^2 dV}{\int_V \frac{\varepsilon_0}{4}\{\varepsilon_g(\mathbf{r},\omega_0) + \Re[\varepsilon(\mathbf{r},\omega_0)]\}|\mathbf{E}|^2 dV} \tag{2.30}$$

in which

$$\varepsilon_g = \frac{\partial}{\partial\omega}\Re[\omega\varepsilon(\mathbf{r},\omega)] \tag{2.31}$$

and subscript a denotes active gain material. Generally, $g_{th} \leq 1000$ cm^{-1} is achievable in III-V quantum well materials [73, 74].

2.2 Numerical modeling of photon confinement and radiation

2.2.1 Near-field calculation using finite-difference time-domain method

2D and 3D optical structures often do not have exact analytical solutions, and numerical methods are called for. The main methods used are finite-difference time-domain (FDTD) and finite element method (FEM); both are based on the idea of implementing master differential or integral equations using finite differential elements. In this work, numerical simulations are done using the FDTD program developed by Dr. Se-Heon Kim *pFDTD* [31] in conjunction with another FDTD-based program *MEEP* developed by Prof. Joannopoulos's group at MIT; photonic dispersion relations are calculated using the Joannopoulos group's frequency-domain photonic bandgap program *MPB* and pFDTD. FDTD algorithms are a broad and rich subject. In this section, we will only outline the basis of FDTD and finer points particular to this work; references are provided for further details.

The basis of the 3D FDTD analysis used in this work is the algorithm introduced by K. S. Yee [75] and the *perfectly matched layer* boundary conditions put forward by J. P. Berenger [76]. Yee devel-

oped a method to spatially sample the E- and H-field components that robustly represent Maxwell's equations. Berenger's treatment of boundary conditions allows plane waves of arbitrary incidence angle, polarization, and frequency to be absorbed at the boundary, even when the simulation domain contains dispersive, anistropic, and nonlinear media.

The application of FDTD algorithm to dielectric optical materials has become mature. Complications arise when dispersive metals are integrated into the structure. One cannot simply implement dispersive dielectric functions fitted to any mathematical model in FDTD with satisfactory boundary conditions at interfaces of dissimilar media. The dielectric function of metals $\epsilon_m(\omega)$ is therefore fitted to the form of a Lorentz medium, or more commonly a Drude-Sommerfeld medium with one or more poles

$$\varepsilon(\omega) = \varepsilon_\infty - \sum_{p=1}^{P} \frac{\omega_p^2}{\omega^2 + i\omega\gamma_p} \tag{2.32}$$

In *pFDTD*, the main simulation program used in this work, the time-domain auxiliary differential equation method is used to implement Lorentz and Drude media [31, 32, 77].

The introduction of metals also brings regions where changes in the electromagnetic field components are much more rapid than others. While a resolution of 10 or 20 nm is often sufficient to simulate purely dielectric structures, the evanescent field decay in commonly used metals such as silver and gold has a skin depth of about 20 nm, and thus needs a much finer resolution. The large range of required simulation resolutions prompts the need for non-uniform spatial grid within the simulation domain. There are several solutions, including the flexible and robust hybrid FDTD/FEM [78]. However, most of the structures designed in this work only involves metal sheet or cladding that is perpendicular to one of the major axes of the FDTD lattice. Then a quicker solution is to implement the Maloney-Smith technique for thin material sheets [79].

We find an exhaustive compilation of the FDTD method in the book by Taflove and Hagness [78], from which we leant all of the aforementioned algorithms in detail.

2.2.2 Far-field radiation pattern

Commercial laser diodes boast small divergence angles of about 25° [80], so the emitted light can be easily collimated or efficiently coupled into an optical fiber. In the quest for microlasers, earlier efforts have been to improve quantum well and quantum dot materials, to design cavities for higher Q and lower V_{eff}, and to manage device thermal resistance in order to achieve room-temperature CW lasing. Laser emission directionality was not a point of concern until recently. Microtoroid and microdisk lasers emit in radial direction, resulting in low coupling efficiency whether via free-space or tapered fiber [81, 82, 83]. Microdisks were then modified to incorporate intentional asymmetry to enhance emission directionality, so far with improvement to 45° to 70° divergence angle in two opposite directions in-plane with the disk [84, 85]. Photonic crystal lasers are favored for their ability to achieve cold-cavity Q of 10^3 to 10^5 [86][5], while maintaining a V_{eff} of $<0.5(\lambda/n)^3$ [19, 87]. Moreover, photonic crystal lasers show a rich variety of far-field emission patterns, indicating a potential to design the laser cavity with control of emission directionality [51]. One can simulate a laser cavity's far-field pattern in two ways: one, extend the FDTD calculation space to larger than a few free-space wavelengths beyond the emission surface, with the disadvantage of costly computation memory and time, as well as algorithm inelegance; or two, calculate from near-field patterns using surface equivalence theorem, radiation vectors, and Fourier transform (FT) [78, 88], on which we will elaborate in this section. The latter method is well developed, originally as part of antenna theory. Vučković and colleagues also used fast Fourier transform (FFT) based methods to calculate photonic crystal cavities' far-field pattern [89].

Surface equivalence theorem states that if the tangential electromagnetic fields over a closed surface S are completely known, then the fields in the source-free region Ω inside the enclosure can be determined. We can find the fields in Ω by placing equivalent electric and magnetic current densities $\mathbf{J_s}$ and $\mathbf{M_s}$ over S and calculating vector potentials $\mathbf{A}$ and $\mathbf{F}$ using the equivalent current densities [88]. We apply the theorem to find our far-field pattern and set up the calculation geometry as shown in Figure 2.3. The far-field pattern is calculated in the domain Ω bound by an infinite

[5]Material absorption loss of laser cavity materials, such as InP, are taken into account.

hemisphere S, which consists of a horizontal plane $S_{\parallel}$ located just above the top surface of the surface-emitting laser and a dome shaped $S_{\cap}$. $\mathbf{R}$ is the vector from the origin to the point of observation, $\mathbf{R}_{\parallel}$ is from the origin to the point on $S_{\parallel}$, and $\mathbf{R}'$ is from the point on $S_{\parallel}$ to the point of observation.

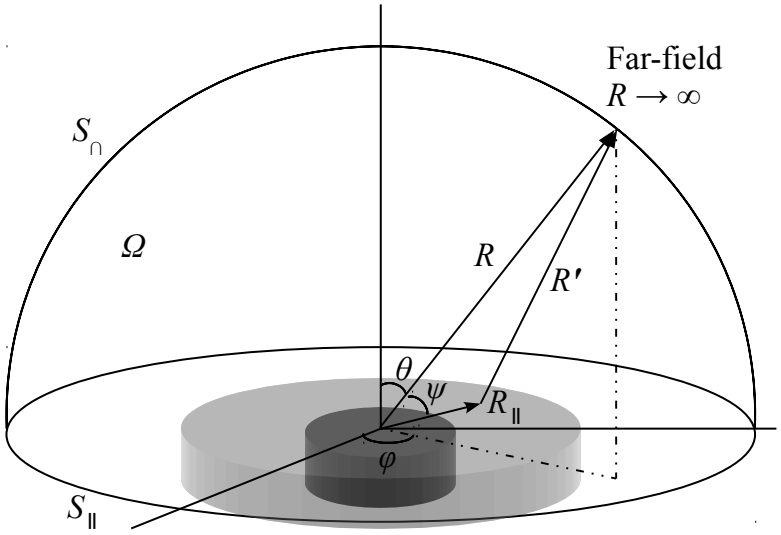

Figure 2.3: Geometry used to calculate far-field pattern of laser emission. It is shown here with a metal-clad disk laser, but is equally applicable when the disk laser is replaced with a photonic crystal cavity in the case of a surface-emitting photonic crystal laser.

Since light can only be coupled from the resonator into free space through a single flat surface, the top surface for the metal-clad disk or photonic crystal designed in this work, we can assume that the electromagnetic field components fall off as $1/R$ and the in-plane components decay exponentially with increasing $|R_{\parallel}|$. The fields in Ω are then determined by the components of $\mathbf{E}$ and $\mathbf{H}$ parallel to the surface $S_{\parallel}$. The equivalent current densities are given by

$$\mathbf{J}_s = \hat{n} \times \mathbf{H} \tag{2.33}$$

$$\mathbf{M}_s = -\hat{n} \times \mathbf{E} \tag{2.34}$$

where $\hat{n}$ is the unit vector normal to the emission surface, and in this case, $\hat{n} = \hat{z}$. The vector

potentials are then calculated using the equivalent current densities by

$$\mathbf{A} = \mu_0 \int_s \frac{\mathbf{J}_s e^{-ikR'}}{4\pi R'} dS \tag{2.35}$$

$$\mathbf{F} = \varepsilon_0 \int_s \frac{\mathbf{M}_s e^{-ikR'}}{4\pi R'} dS \tag{2.36}$$

For large R and R', as in the case of far-field, $R' \approx R - R_{\parallel} \cos\psi$ for phase variation and $R' \approx R$ for amplitude variation. Therefore, we can simplify the vector potentials to

$$\mathbf{A} = \frac{\mu_0}{4\pi} \frac{e^{-ikR}}{R} \int_s \mathbf{J}_s e^{ikR_{\parallel} \cos\psi} dS = \frac{\mu_0}{4\pi} \frac{e^{-ikR}}{R} \mathbf{N} \tag{2.37}$$

$$\mathbf{F} = \frac{\varepsilon_0}{4\pi} \frac{e^{-ikR}}{R} \int_s \mathbf{M}_s e^{ikR_{\parallel} \cos\psi} dS = \frac{\varepsilon_0}{4\pi} \frac{e^{-ikR}}{R} \mathbf{L} \tag{2.38}$$

Express the electromagnetic fields in Ω in terms of the vector potentials, we have the components of $\mathbf{E}$ and $\mathbf{H}$ from vector potential $\mathbf{A}$ given by

$$\mathbf{E}_A = -i\omega \left[\mathbf{A} + \frac{1}{k^2} \nabla(\nabla \cdot \mathbf{A}) \right] \tag{2.39}$$

$$\mathbf{H}_A = \frac{1}{\mu_0} \nabla \times \mathbf{A} \tag{2.40}$$

and the components contributed by vector potential $\mathbf{F}$ are given by

$$\mathbf{E}_F = -\frac{1}{\varepsilon_0} \nabla \times \mathbf{F} \tag{2.41}$$

$$\mathbf{H}_F = -i\omega \left[\mathbf{F} + \frac{1}{k^2} \nabla(\nabla \cdot \mathbf{F}) \right] \tag{2.42}$$

so the total fields are $\mathbf{E} = \mathbf{E}_A + \mathbf{E}_F$ and $\mathbf{H} = \mathbf{H}_A + \mathbf{H}_F$. In the far-field, the R components of $\mathbf{E}$

and **H** become negligible,[6] E_θ, E_φ, H_θ, and H_φ are the dominant components, given by

$$E_r \approx 0, \tag{2.43}$$

$$E_\theta \approx -i\omega(A_\theta + \eta F_\varphi) = -\frac{ike^{-ikR}}{4\pi R}(L_\varphi + \eta N_\theta), \tag{2.44}$$

$$E_\varphi \approx -i\omega(A_\varphi - \eta F_\theta) = \frac{ike^{-ikR}}{4\pi R}(L_\theta - \eta N_\varphi), \tag{2.45}$$

$$H_r \approx 0, \tag{2.46}$$

$$H_\theta \approx \frac{i\omega}{\eta}(A_\varphi - \eta F_\theta) = \frac{ike^{-ikR}}{4\pi R}(N_\varphi - \frac{L_\theta}{\eta}), \tag{2.47}$$

$$H_\varphi \approx -\frac{i\omega}{\eta}(A_\theta + \eta F_\varphi) = -\frac{ike^{-ikR}}{4\pi R}(N_\theta + \frac{L_\varphi}{\eta}), \tag{2.48}$$

where $\eta = \sqrt{\mu/\varepsilon}$.

The precise expression for the θ- and φ- components of **N** and **L** depends on the coordinate system used in calculating the laser cavity's near-field **E** and **H**. Microdisk, pillar, and toroid cavities all have azimuthal symmetry. To save computation resources, near-field simulations of these devices are usually done in cylindrical coordinates (r,ρ,z), where one assumes an analytical ρ-dependence in the form $e^{im\rho}$ where m is an integer. In this case, N_θ, N_φ, L_θ, and L_φ are given by

[6] Radiated fields from an emitter of finite dimensions are spherical waves, then the general solution for vector potentials **A** and **F** in spherical coordinates take the forms

$$\mathbf{A} = \hat{a}_R A_R(R,\theta,\varphi) + \hat{a}_\theta A_\theta(R,\theta,\varphi) + \hat{a}_\varphi A_\varphi(R,\theta,\varphi)$$

$$\mathbf{F} = \hat{a}_R F_R(R,\theta,\varphi) + \hat{a}_\theta F_\theta(R,\theta,\varphi) + \hat{a}_\varphi F_\varphi(R,\theta,\varphi)$$

The amplitude dependence on R is of the form $1/R$, $n = 1, 2, \ldots$. In the limit of $r \to \infty$ and neglecting higher order terms of $1/R$, $n > 1$, the general solutions reduce to

$$\mathbf{A} = [\hat{a}_R A'_R(\theta,\varphi) + \hat{a}_\theta A'_\theta(\theta,\varphi) + \hat{a}_\varphi A'_\varphi(\theta,\varphi)]\frac{e^{-ikR}}{R}$$

$$\mathbf{F} = [\hat{a}_R F'_R(\theta,\varphi) + \hat{a}_\theta F'_\theta(\theta,\varphi) + \hat{a}_\varphi F'_\varphi(\theta,\varphi)]\frac{e^{-ikR}}{R}$$

Substitute the new general solutions into 2.39 and 2.42, respectively, we obtain

$$\mathbf{E} = \frac{-i\omega e^{-ikR}}{R}[\hat{a}_\theta A'_\theta(\theta,\varphi) + \hat{a}_\varphi A'_\varphi(\theta,\varphi)] + \text{higher order terms}$$

$$\mathbf{H} = \frac{-i\omega e^{-ikR}}{R\sqrt{\mu/\varepsilon}}[\hat{a}_\theta A'_\theta(\theta,\varphi) + \hat{a}_\varphi A'_\varphi(\theta,\varphi)] + \text{higher order terms}$$

Only the θ and φ components remain; E_R and H_R are both zero, since their contribution from the two terms of 2.39 and 2.42 cancel each other.

$$\begin{aligned} N_\theta &= \int_S [J_r \cos\theta \cos(\varphi-\rho) + J_\rho \cos\theta \sin(\varphi-\rho) - J_z \sin\theta] e^{ikR_\parallel \cos\psi} dS \\ &= \int_S [-H_\rho \cos\theta \cos(\varphi-\rho) + H_r \cos\theta \sin(\varphi-\rho)] e^{ikR_\parallel \cos\psi} dS \end{aligned} \tag{2.49}$$

$$\begin{aligned} N_\varphi &= \int_S [-J_r \sin(\varphi-\rho) + J_\rho \cos(\varphi-\rho)] e^{ikR_\parallel \cos\psi} dS \\ &= \int_S [H_\rho \sin(\varphi-\rho) + H_r \cos(\varphi-\rho)] e^{ikR_\parallel \cos\psi} dS \end{aligned} \tag{2.50}$$

$$\begin{aligned} L_\theta &= \int_S [M_r \cos\theta \cos(\varphi-\rho) + M_\rho \cos\theta \sin(\varphi-\rho) - M_z \sin\theta] e^{ikR_\parallel \cos\psi} dS \\ &= \int_S [E_\rho \cos\theta \cos(\varphi-\rho) - E_r \cos\theta \sin(\varphi-\rho)] e^{ikR_\parallel \cos\psi} dS \end{aligned} \tag{2.51}$$

$$\begin{aligned} L_\varphi &= \int_S [-M_r \sin(\varphi-\rho) + M_\rho \cos(\varphi-\rho)] e^{ikR_\parallel \cos\psi} dS \\ &= \int_S [-E_\rho \sin(\varphi-\rho) - E_r \cos(\varphi-\rho)] e^{ikR_\parallel \cos\psi} dS \end{aligned} \tag{2.52}$$

However, most photonic crystal cavities are designed to have a broken azimuthal symmetry to break the degeneracy in resonant modes, e.g. degeneracy in the dipole mode of a point-defect cavity in a triangular photonic crystal [90], and often to produce linearly polarized emission for efficient coupling into a fiber or the next optical device [51]. With these designs, FDTD simulations are carried out in cartesian coordinates, in which case N_θ, N_φ, L_θ, L_φ take the form

$$N_\theta = \int_S (J_x \cos\theta \cos\varphi + J_y \cos\theta \sin\varphi - J_z \sin\theta) e^{ikR_\parallel \cos\psi} dS \tag{2.53}$$

$$N_\varphi = \int_S (-J_x \sin\varphi + J_y \cos\varphi) e^{ikR_\parallel \cos\psi} dS \tag{2.54}$$

$$L_\theta = \int_S (M_x \cos\theta \cos\varphi + M_y \cos\theta \sin\varphi - M_z \sin\theta) e^{ikR_\parallel \cos\psi} dS \tag{2.55}$$

$$N_\varphi = \int_S (-M_x \sin\varphi + M_y \cos\varphi) e^{ikR_\parallel \cos\psi} dS \tag{2.56}$$

Alternatively, as Kim and colleagues outlined in [51], $kR_\parallel \cos\psi$ in Eqs. 2.37 and 2.38 is simply $k_x x + k_y y$, thus $\mathbf{N}$ and $\mathbf{L}$ are 2D Fourier transforms ($\mathcal{F}$) of $\mathbf{J}_s$ and $\mathbf{M}_s$, respectively,

$$N_x(k_x, k_y) = -\mathcal{F}\{H_y(x,y)\} \tag{2.57}$$

$$N_y(k_x, k_y) = \mathcal{F}\{H_x(x, y)\} \tag{2.58}$$

$$L_x(k_x, k_y) = \mathcal{F}\{E_y(x, y)\} \tag{2.59}$$

$$L_y(k_x, k_y) = -\mathcal{F}\{E_x(x, y)\} \tag{2.60}$$

Thus, one can fast Fourier transform (FFT) the near-field data obtained from FDTD and use the result to calculate the far-field pattern. In doing the FFT, the input data is an N $\times$ N array of discretized x-y plane, and the output is an N $\times$ N array in frequency space. The extent of the input array corresponds to a length of L wavelengths in physical space, the extent of the output array then corresponds to a frequency range of Nf_0/L with a discrete step size $1/(L\lambda) = f_0/L$. The light-cone boundary corresponds to the L-th point in frequency space; only those components lying within the light-cone contribute to far-field radiation.

Chapter 3

Design for room-temperature CW lasing with high-$F_p\beta$ and directional emission

Theoretical investigations establish that the effect of spontaneous emission modification is more pronounced in a cavity with high Q/V [11] and that the control of spontaneous emission coupling to a cavity's optical modes could lead us to build high modulation rate light sources [91], low noise [92] and *thresholdless* [93, 94] laser, and single-photon source [95]. At the time this work began, researchers had long recognized the potential of photonic crystals as a way to design high Q/V laser cavities. VCSELs and the related micropillars are essentially 1D photonic crystal lasers with strong light confinement [7, 8]. The first 2D slab photonic crystal laser with a V_{eff} about the volume of a half cubic wavelength was reported by Painter and colleagues in [90] with Q of 250 and pulsed lasing at a temperature of 143 K. Since then, many more optically pumped photonic crystal lasers have been reported and studied, however, mostly with pulsed operation at room temperature due to device thermal resistance as high as $10^5 \sim 10^6$ K/W, where material gain saturates and non-radiative processes overwhelm before the device can go into stimulated emission [17, 90, 96]. At the same time, the photonic crystal community learnt to design extremely high Q/V cavities—$Q > 10^6$ in the case of double-heterostructure cavities with $V_{eff} \approx 1.2(\lambda/n)^3$ [56], $V_{eff} \approx 0.3(\lambda/n)^3$ in point-shift cavities with $Q = 10^5$ [50], and $V_{eff} \approx 0.4(\lambda/n)^3$ with $Q \approx 10^7$ in nanobeam photonic crystal cavities [58].

To alleviate thermal resistance, many proposed or tried bonding photonic crystal membranes to

a thermally conductive substrate such as the lower index aluminum oxide [97, 98] or DBR mirrors [99] with varying degrees of success; however, most low-index materials are electrically insulating, complicating potential designs to build current-injection photonic crystal lasers. Another solution is to reduce the lasing threshold by increasing Q or decreasing the transparency carrier density N_{tr} required for lasing [19, 86].

Our goal is to build a room temperature, CW microlaser with a *soft* threshold transition, directional emission, and current-injection (as opposed to optical pumping) operation. In the subsequent sections, we present the device design progress made in this work. We begin by studying the possibility of using metal to improve disk lasers' cavity Q, V_{eff}, and emission directionality [27]. We then investigate the merit of using metal in conjunction with photonic crystal nanocavity to serve as both a thermal and electrical conduction path, which may help achieve room temperature CW lasing by current injection [32]. In looking at the confinement mechanisms of photonic crystal cavity on metal, we find that optical confinement can be obtained in optically thick[1] photonic crystal slab with $Q \approx 1000$ while keeping $V_{eff} \approx (\lambda/n)^3$. We show this structure is feasible to lase [101] and that the thicker slab gives us more space to properly design a vertical p-i-n stack, where gain is in the intrinsic region, for current-injection operation. Following that, we turn our attention back to photonic crystal cavities in optically thin slabs and evaluate ways to improve the far-field emission directionality using coupled-cavity designs [102]. Lastly, we push the limit of optical confinement in semiconductor dielectrics with the nanobeam photonic crystal designs. We expect their small V_{eff} will result in a high $F_p\beta$ laser with a *soft* threshold transition, and their small cross-sectional area will reduce the effect of feedback from surrounding structures, compared with 2-D photonic crystal cavities [87].

[1] Most 2D photonic crystal cavities are thus far designed for optically thin slabs, about $\lambda/2n$, in order to maximize photonic bandgap size [100].

3.1 Metal-clad disk laser

Metal-optic and plasmonic cavities have in recent years been of particular interest. Due to their dispersive dielectric function $\epsilon_m(\omega)$, whose real part $\Re\{\epsilon_m\}$ is negative in the NIR and visible spectra [28, 103], metals such as gold and silver can be used to overcome the diffraction limit and confine electromagnetic energy to very small volumes [104, 105, 106]. Yet metals also present considerable optical loss that worsens as wavelength decreases from NIR to visible. As a result, most subwavelength metallic cavities have room temperature Q factors of below 100, and thus can only lase in cryogenic temperatures with III-V semiconductor as the gain material [20, 107, 108]. Mizrahi, Nezhad, Fainman, and colleagues have proposed and demonstrated higher Q metallic cavities by inserting a low-index silicon dioxide SiO_2 layer around the semiconductor gain material, that is thick enough to push the optical mode away from the metal [109, 110]. However, this complicates the realization of an electrically pumped laser based on the same design and precludes the use of metal as an effective heat sink, a feature that is proving to be important for small volume semiconductor lasers [96, 111].

In this section, we present a design of surface-emitting, subwavelength metal-clad disk laser cavities that have a room temperature Q-factor of 200 to 300 at the visible red wavelength of $\lambda \approx 670$ nm. Non-degenerate single-mode operation can be achieved by shrinking device size, retaining only the TE_{011} mode, and thereby increasing the spontaneous emission coupling factor β. The laser cavity's Q and extraction efficiencies can be tuned by placing a reflector directly under the device's bottom surface. The TE_{011} mode can have a Q of 230 and a V_{eff} of $0.46(\lambda_0/n)^3 \sim 0.004$ μm^3 with a 400×400 nm^2 footprint. Far-field radiation pattern and emission directionality are also evaluated.

3.1.1 Laser cavity design

Dielectric disk laser cavities have Q-factors limited by radiation loss in the horizontal direction, which imposes a lower limit of $d_0 \approx 0.7 \sim 0.8\lambda$ on device size [112, 113, 114], where d_0 is the dielectric disk diameter. We consider specifically, as an example, a disk laser cavity designed for the more localized transverse electric-like TE_{mpq} modes (m, p, and q are the azimuthal, radial, and

axial mode numbers, respectively) at $\lambda = 670$ nm. It has a thickness of $T = 210$ nm and a dielectric constant of $\varepsilon_d = 11$, corresponding to the commonly used red laser material AlGaInP [115]. As is evident in Figure 3.1, cavity Q falls sharply as the disk diameter shrinks, and a resonant mode with $m < 3$ can hardly exist.

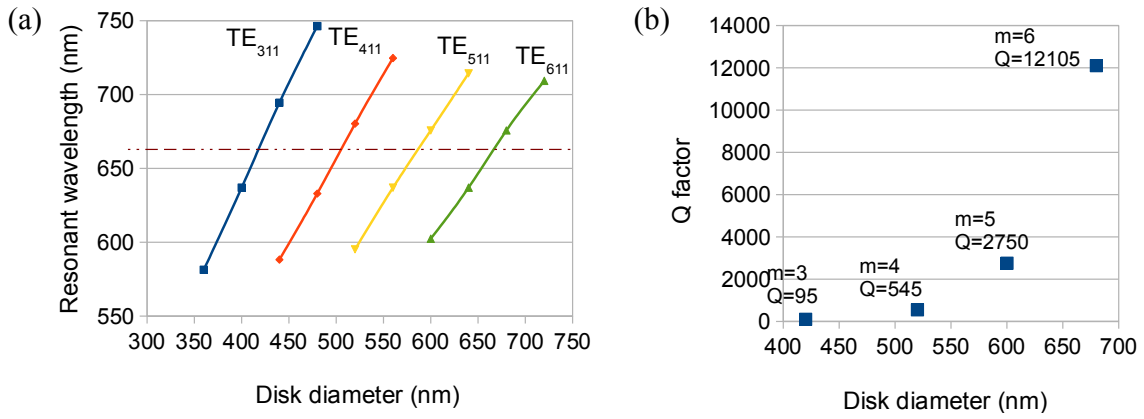

Figure 3.1: (a) Resonant modes for various disk diameters, the dotted red line indicates $\lambda = 670$ nm resonant wavelength; (b) Q-factors for various disk diameters at $\lambda \approx 670$ nm. $d_0 = 420$ nm gives TE_{311} with $\lambda = 667$ nm and $Q = 95$, $d_0 = 520$ nm gives TE_{411} with $\lambda = 682$ nm and $Q = 545$, $d_0 = 600$ nm gives TE_{511} with $\lambda = 677$ nm and $Q = 2750$, and $d_0 = 680$ nm gives TE_{611} with $\lambda = 675$ nm and $Q = 12105$.

To curb radiation loss, we clad the semiconductor disk's curved surface in an optically thick, reflective, and low loss metal layer, shown schematically in Figure 3.2(a). We choose to use silver, because it is a relatively low loss metal in the visible spectrum. Its dispersive dielectric function can be described by fitting experimental data to the Drude-Sommerfeld model [28, 103, 116].

$$\varepsilon_{Ag}(\omega) = \varepsilon_h - \frac{(\varepsilon_s - \varepsilon_h)\omega_p^2}{\omega^2 + i\omega\gamma} \tag{3.1}$$

where, at room temperature, $\varepsilon_s = 6.18$ is the relative permittivity in the static limit, $\varepsilon_h = 5.45$ is the relative permittivity in the high frequency limit, $\omega_p = 1.72 \times 10^{16}$ rad/s is the plasma frequency, and $\gamma_c = 8.35 \times 10^{13}$ rad/s is the damping or collision frequency. The skin depth of silver at this wavelength is about 25 nm, so a metal thickness of $\geq$100 nm in the radial direction is sufficient. We use a high resolution of 2 nm in the FDTD simulations to capture the rapid attenuation of electromagnetic fields in metal. A sub-wavelength sized device with $d_0 = 420$ nm forms a multi-

mode resonator and, due to the effective radiation loss inhibition by the silver cladding, supports the lowest order $m = 0, 1, 2, 3$ modes with Q-factors of 160 to 290. The non-degenerate $m = 0$ mode has a Q of 240. Normalized mode profiles are shown in Figure 3.2(b)–(e). To obtain non-degenerate single-mode operation, the device needs to be shrunk to $d_0 = 220$ nm, where only the TE_{011} mode is supported with a Q of 210; its mode profile is shown in Figure 3.3(a)–(b). We note that the presence of silver cladding enables the co-existence of a $\lambda \sim 670$ nm SPP resonant mode, distinguished by its electric field maximum at the silver-dielectric interface, as shown in Figure 3.3(c)–(d); however, it has a material absorption limited low Q of about 50, since a large fraction of the electromagnetic field exists in the metal cladding and suffers much ohmic loss.

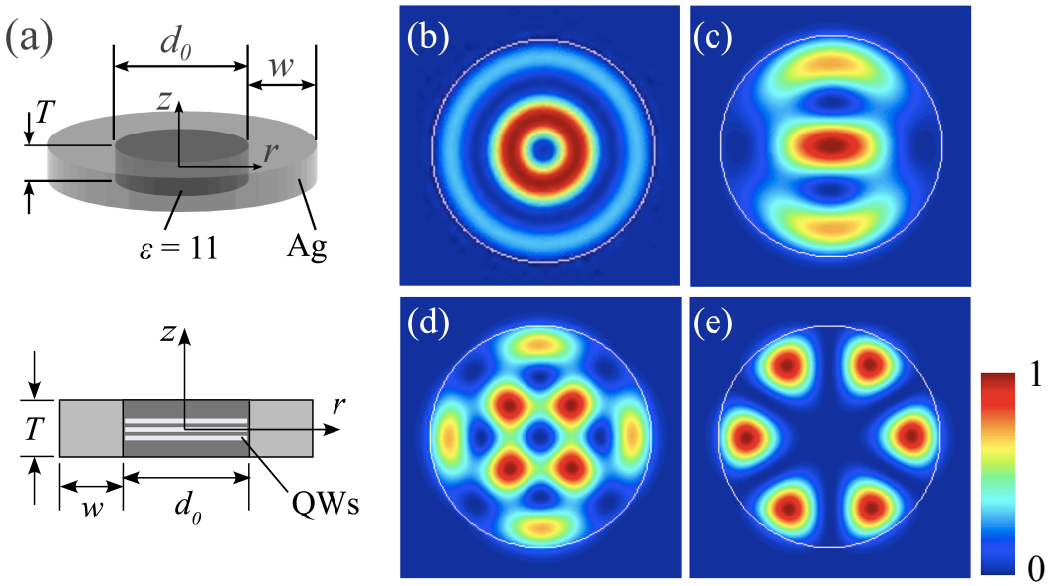

Figure 3.2: (a) 3D schematic and side view cross-section of the silver-clad disk cavity, the origin of the coordinate system is located at the center of the dielectric disk; (b)–(e) Electric-field intensity distribution $|\mathbf{E}|^2$ of resonant modes in a $d_0 = 420$ nm cavity, $m = 0$ (TE_{021}, $\lambda = 642$ nm, $Q = 240$), $m = 1$ (TE_{122}, $\lambda = 660$ nm, $Q = 160$), $m = 2$ (TE_{221}, $\lambda = 676$ nm, $Q = 230$), and $m = 3$ (TE_{311}, $\lambda = 675$ nm, $Q = 290$), respectively. White circle indicates the dielectric-silver interface. Field maximum is at $z = 0$ for $m = 0, 2, 3$ and at $z \approx \pm T/4$ for $m = 1$.

To evaluate if the cavity can lase, we use Equations (2.29) and (2.30) introduced in Section 2.1.5 and experimentally measured and fitted dielectric function $\varepsilon_d(\omega)$ for GaInP/AlGaInP [117], and assume that optical gain comes from seven or nine 7-nm thick GaInP QWs separated by 10-nm

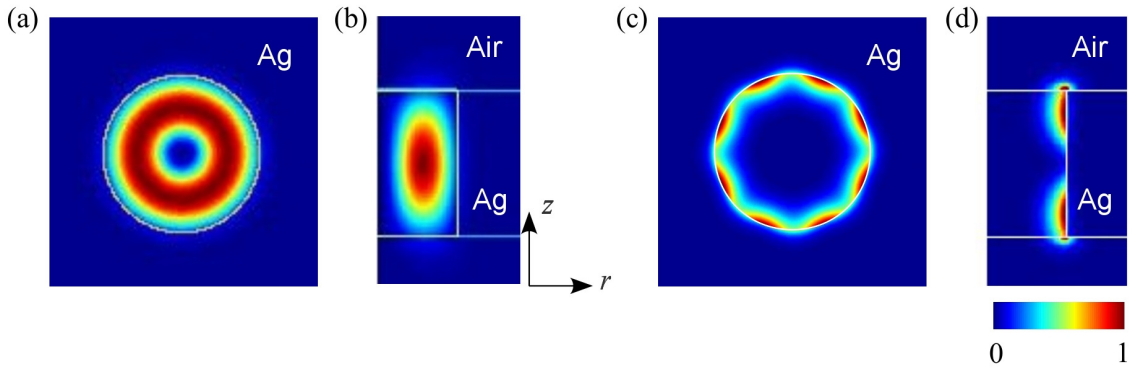

Figure 3.3: Electric-field intensity distribution $|\mathbf{E}|^2$ of modes in a $d_0 = 220$ nm cavity: TE_{011} mode at (a) the horizontal center plane $z = 0$ and (b) the vertical center plane of the disk, $\lambda = 663$ nm; surface plasmon mode at (c) the horizontal $z = 80$ nm plane and (d) the vertical center plane through field intensity maxima, $\lambda_{SP} = 675$ nm. White lines indicate material interfaces.

thick $Al_{0.3}GaInP$ barriers [74, 113] with the middle well located at the $z = 0$ plane, as shown in Figure 3.2(a). Purcell factor F_p is calculated using Equation (2.27). The calculated results are given in Table 3.1. For comparison, we include data for the aforementioned SPP resonant mode. The $m = 0$ modes experience the most spontaneous emission enhancement due to their relatively high Q, smaller V_{eff}, and non-degeneracy. All of the low order non-plasmonic resonant modes have similar or better Purcell factor and much better radiation efficiency compared with the SPP mode. The SPP mode's low Q and poorer Γ_E also results in much higher g_{th}, more or less precluding the possibility of room temperature lasing. With 7 QWs, the non-plasmonic modes' g_{th} ranges between $5348 \sim 16016$ cm^{-1}; with 9 QWs, it is between $4644 \sim 9810$ cm^{-1}. These threshold gain values are still not quite achievable in GaInP/AlGaInP at room temperature [74, 118].

Table 3.1: Comparative characteristics of metal-clad disk modes

	$d_0 = 220$ nm		$d_0 = 420$ nm			
	$m = 0$	SPP mode	$m = 0$	$m = 1$	$m = 2$	$m = 3$
Q_{tot}	210	54	240	160	230	290
λ [nm]	663	664	642	660	676	675
V_{eff} $[(\lambda/n)^3]$	0.46	0.23	0.71	0.80	1.27	1.36
F_p	35	18	26	15	14	16
η_{rad}	0.16	0.00017	0.47	0.72	0.39	0.33
Γ_E (7 QWs)	0.34	0.14	0.32	0.17	0.34	0.14
g_{th} [cm^{-1}]	5922	53837	5607	16016	5348	10409
Γ_E (9 QWs)	0.39	0.24	0.38	0.27	0.39	0.21
g_{th} [cm^{-1}]	5085	31896	4833	9810	4644	6831

Higher Qs are needed to bring down g_{th} and make room-temperature operation feasible. There

are two loss channels for the metal-clad disk cavity: radiation loss into free-space and absorption loss mostly due to the metal's significant $\Im\{\varepsilon_m\}$. By separating out the Q_{rad} and Q_{abs} components, it is apparent that Q_{tot} is limited by material absorption. For the TE_{011} mode, for example, Q_{rad} is >1000, while Q_{abs} is around 250 and dominates. Indeed for most metallic cavities at optical wavelengths, the material absorption limited room temperature Q is seldom greater than 100 and lasing only occurs at cryogenic temperatures [20, 107, 119].

Looking ahead to extending similar designs to CW current-injection operation, a low-index dielectric needs to be inserted between the semiconductor disk and the metal cladding to curb metallic absorption and to provide electrical insulation where needed. We can imagine a combination of thermally conductive aluminum oxide and electrically conductive indium tin oxide (ITO). More specifically, we envision two potential schemes for current-injection. First, thin insulating dielectric layers will need to be inserted at parts between the metal and the semiconductor material for electrical isolation, but this can be done with negligible effect on the device's optical properties. One can use standard-grown epitaxial p-i-n structures, where the quantum wells, wires, or dots typically lie in plane with the epitaxial layers, indicated by parallel white lines in Figure 3.4(a). Bulk silver cladding forms one electrical contact, while a transparent conductor such as ITO or a thin (∼30 nm) Ag layer forms the other contact. Alternatively, epitaxially grown structures with concentric quantum wells have been reported [120]. The $m \neq 1$ modes all have zero electric field along the z-axis in the cavity. One can then propose a radial p-i-n device with one of the electrodes at the center of the disk's top surface, and the other electrical contact via the curved surface, as shown in Figure 3.4(b).

3.1.2 Radiation characteristics

A metal-clad disk laser such as one shown in Figure 3.2(a) radiates through both its top and bottom surfaces. It is difficult to collect light in both directions; half of the radiated light would be lost. We can thus think of placing a reflector under the disk to redirect the downward traveling light, as has been proposed for microcavity LEDs [121, 122] and photonic crystal resonators [51]. To keep to

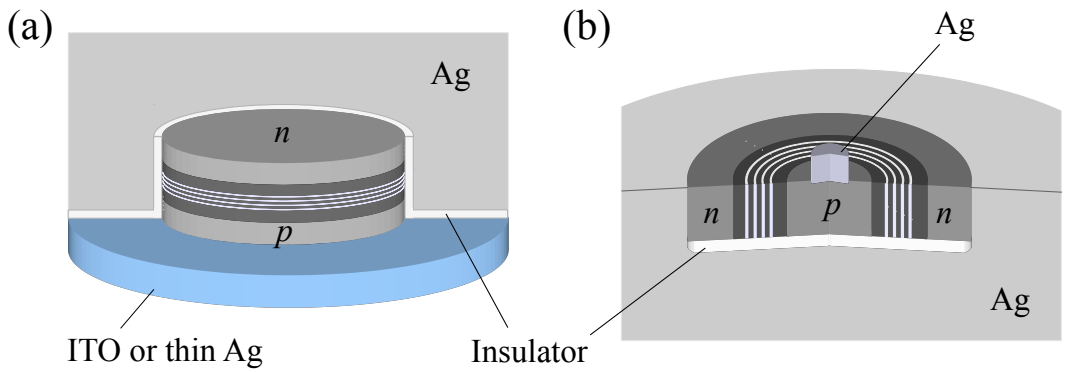

Figure 3.4: Two current-injection schemes for metal-clad disk laser design

the sub-wavelength size and mode volume and to be able to place the reflector arbitrarily close to the resonator's bottom surface, we use an optically thick silver layer instead of Bragg reflectors. A silicon dioxide SiO_2 spacer of thickness h is used to tune the radiation characteristics. Other low-index materials can also be used for better thermal conductivity, such as silicon nitride or aluminum oxide. The device structure is shown in Figure 3.5(a). To illustrate the effect of the bottom reflector, we study the non-degenerate TE_{011} mode (see Figure 3.3). The electric field has its maximum located at $z = 0$ and decays to small magnitude at the $\varepsilon_d = 11$ dielectric disk's top and bottom surfaces. Silver has a large negative real dielectric constant $\Re\{\varepsilon_{Ag}\} \approx -22$ at $\lambda = 670$ nm [28, 103]. Therefore, the bottom reflector results in little change in the resonant mode profile, even when it is in contact with the disk resonator, as shown in Figure 3.5(b). Although we are mostly interested in (near-)room temperature operation for laser applications, it is nevertheless instructive to look at the effect of the bottom reflector at lower temperatures. The low temperature metallic dielectric function $\varepsilon_{Ag}(\omega)$ can be estimated using the resistivity versus temperature data of silver [123]. The damping frequency is proportional to material resistivity, and is 18% of its room temperature value at T = 80 K.

Loss due to metallic absorption does not change much, regardless of the presence of the bottom silver reflector or its position. Q_{abs} is consistently about 250 at room temperature and 1400 at 80 K. The increase in Q_{abs} with respect to temperature is as expected, due to the corresponding decrease in resistivity and thus ohmic loss in silver. On the other hand, Q_{rad} are strongly modulated

by the bottom reflector. By varying the spacer thickness h, Q_{rad} changes between 225 and 2710, and thereby enhances or deteriorates Q_{tot}. When $h \leq 150$ nm, Q_{rad} is enhanced with no additional material absorption loss, consequently at room temperature Q_{tot} is increased to 230, from $Q_{tot} = 150$ for a laser cavity on SiO_2 substrate or $Q_{tot} = 210$ for one suspended in air with no bottom reflector. When $h \approx 250$ nm, however, Q_{rad} is at a minimum and Q_{tot} deteriorates to 120.

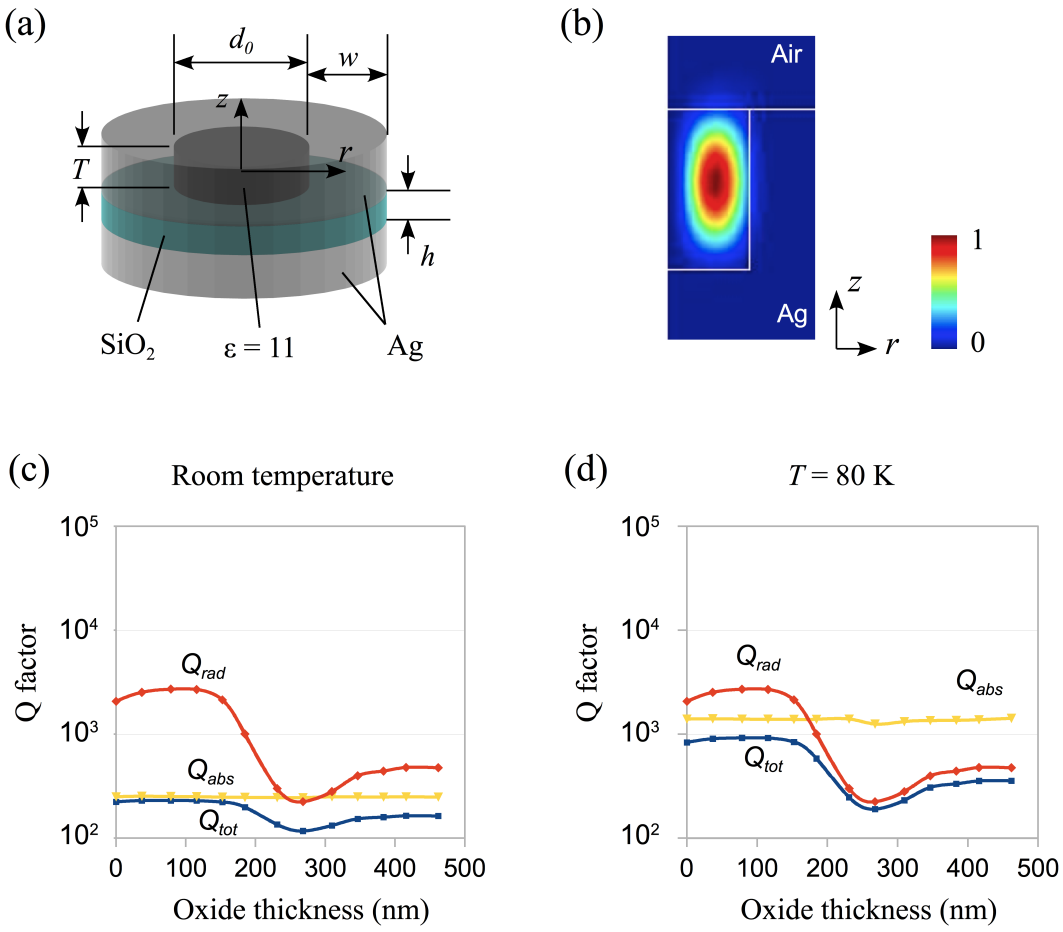

Figure 3.5: Q_{tot}, Q_{abs}, and Q_{rad} of metal-clad disk resonators with a bottom reflector

We proceed to study the far-field radiation pattern of the surface-emitting metal-clad disk laser. Normalized far-field intensities are plotted in Figure 3.6(b) and (c) with the laser surface normal at the center, and 30°, 60°, and 90° from surface normal are indicated with dotted white circles.

To study the far-field radiation pattern due to light emission from the top surface alone, we extend the cladding thickness w to 1 μm in order to block any interference due to light emitted from

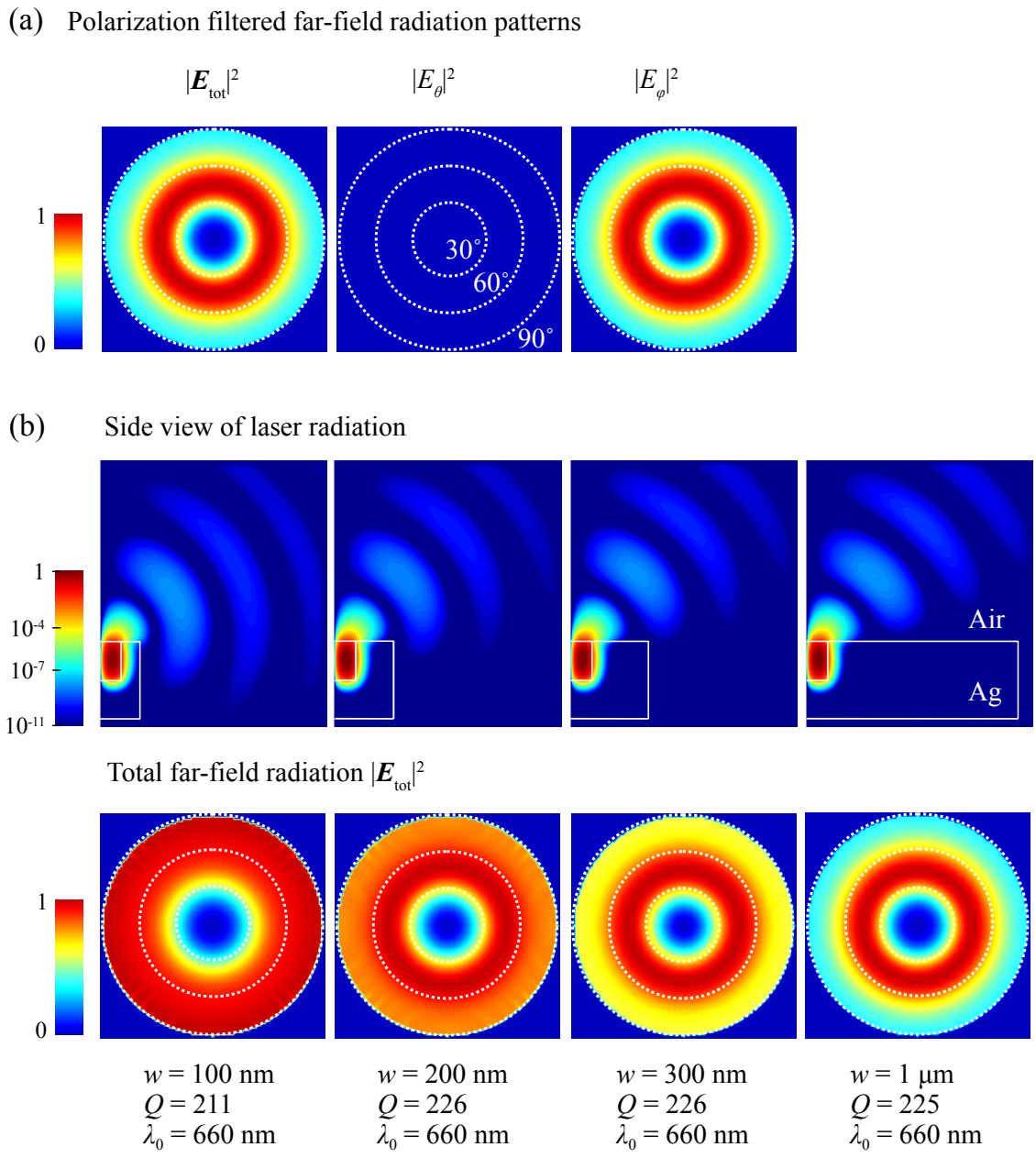

Figure 3.6: Metal disk far-field

the disk's bottom surface and reflected off of material interfaces. The TE_{011} mode from a $d_0 = 220$ nm cavity exhibits a mostly φ-polarized far-field radiation with negligible θ-polarization, which is analogous to the far-field pattern of the monopole mode in a single-defect photonic crystal cavity [51]. The radiation is directed upward, with the field intensity maximum at about 45° from surface normal, as shown in Figure 3.6(b). We find that the far-field pattern remains unchanged with or without the bottom reflector and as we vary the spacer thickness h.

As we reduce w, however, the radiated light interacts with the laser cavity's surroundings; the far-field pattern is strongly affected. Take the example of the TE_{011} mode with a bottom reflector and $h = 0$, where the only light emission is through the laser cavity's top surface. Varying w from 1 μm to 100 nm, the resonator retains its resonant wavelength of $\lambda = 660.2$ nm and a Q_{tot} of 210 to 225. The far-field radiation remains φ-polarized, but its field intensity distribution changes from having a distinct maximum at 45° to spreading in the horizontal direction between 60° and 90°; the device changes from a surface-emitting laser to a horizontal emitter with poorer directionality, as is evident in Figure 3.6(c). Thus, in designing sub-wavelength lasers, one needs to be aware of the influence on the directionality of the emitted light by structures surrounding the laser cavity. While a metal cladding thickness of several times the metal's skin depth is sufficient to suppress radiation loss and create a laser resonator, it may need to be of wavelength scale to obtain light emission in the desired direction.

3.1.3 Conclusion

We analyzed metal-clad disk cavities designed for nanolasers in the visible red spectrum with sub-wavelength device size and mode volume. Metal cladding suppresses radiation loss and supports low order modes with room temperature Q of $200 \sim 300$. Non-degenerate single-mode operation with enhanced spontaneous emission coupling factor β is expected with the TE_{011} mode that has a $0.46(\lambda/n)^3$ mode volume and $Q = 210$ in a device of size $0.12\lambda^3$. Placing a planar metal reflector under the cavity can enhance radiation and extraction efficiencies or increase the Q, without incurring additional metallic absorption loss. We show that the far-field radiation characteristics are strongly

affected by the devices' immediate surroundings, such as changes in metal cladding thickness, even as the resonant mode profile, frequency, and Q remain the same. When the metal cladding is 1 μm thick, light radiates upward with a distinct intensity maximum at 45°; when the cladding is 100 nm thick, the emitted light spreads in a near-horizontal direction.

3.2 Photonic crystal cavity bonded on metal

Photonic crystal defect cavity lasers are a relatively new design. The research field has so far been occupied with progress toward achieving stable lasing at room temperature with hope of demonstrating signatures of Purcell effect [6, 19, 124]. Much progress was made in fine-tuning the cavity geometry for high Q/V [49, 50, 52, 56, 125] and improving fabrication techniques [96, 126, 127, 128]. Interestingly, the basic device structure has not changed since the first 2D photonic crystal laser [15, 90]—a regular array of air-holes are drilled into a suspended III-V semiconductor membrane to form the 2D photonic crystal, a single defect or several adjacent defects where there is no air-hole form the cavity. In most cases, the membrane is suspended less than one free-space wavelength above the substrate. Research on now-established forms of lasers, including Fabry-Pérot-type semiconductor diode lasers, have shown that feedback from a laser's output signal can significantly alter the device's linewidth and other noise characteristics; even 0.5% is considered a large feedback [71]. For photonic crystal lasers, Kim and colleagues [51] investigated the effect of the bottom substrate on a single-defect cavity's emission characteristics, calling to attention both the tunability of emission directionality and the effect of feedback from structures surrounding the suspended photonic crystal membrane.

We build upon this investigation using the single-defect cavity, whose structure and resonant mode profiles are reproduced in Figure 3.7. The dipole and hexapole modes are studied in particular, for they are able to achieve vertical light emission with a small divergence angle, unlike the monopole and quadrapole modes. The reason for this difference can be understood using the simple symmetry argument of the modes' electric fields, see Figure 3.8. For the monopole and quadrapole modes, E_x and E_y field components both exhibit odd symmetry across x- and y-axes, respectively, therefore

they interfere destructively along the z-axis, the far-field intensity is necessarily zero in the vertical direction. E_x component of the dipole mode and E_y component of the hexapole mode also show odd symmetry across the x- and y-axes, respectively; their contribution to radiation intensity in the vertical direction is also zero. In contrast, E_y of the dipole mode and E_x of the quadrapole mode have even symmetry, so the fields interfere constructively along the z-axis, making vertical light emission a possibility.

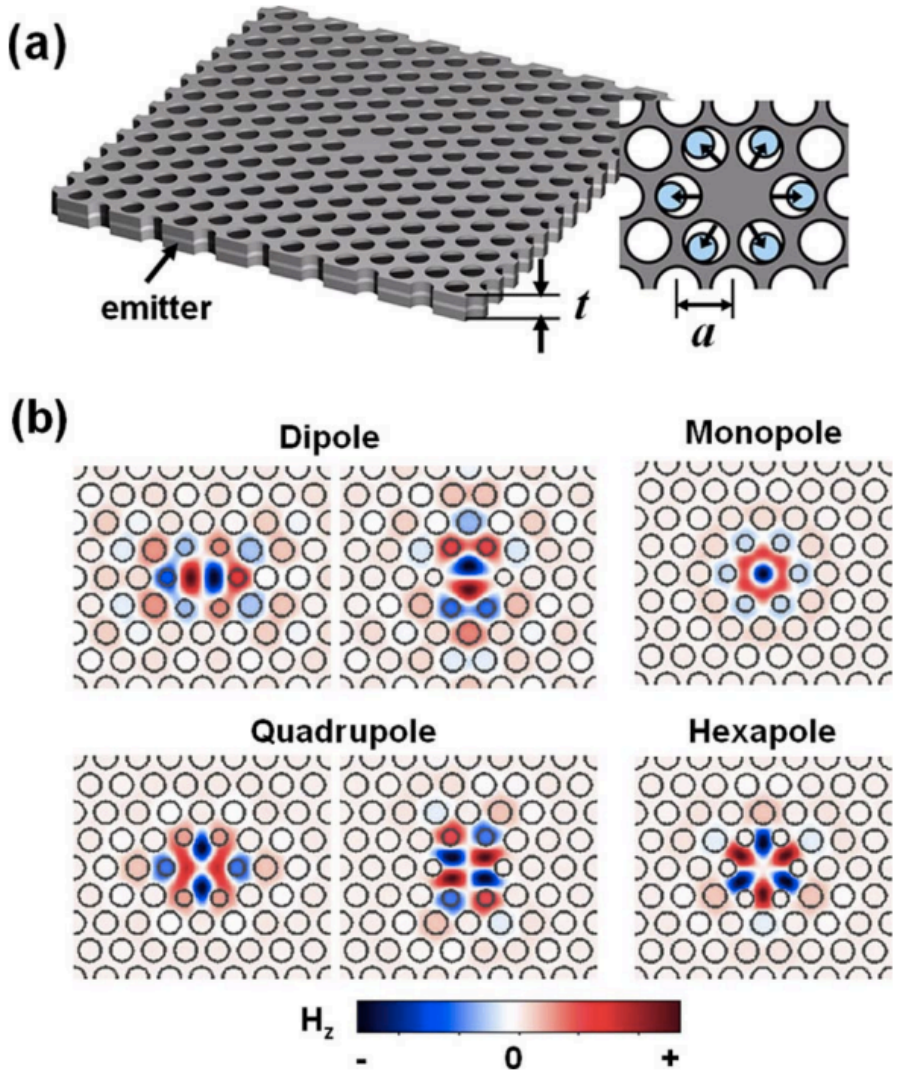

Figure 3.7: Modified single-defect cavity. (a) Device structure. (b) H_z field profile for the distinct resonant modes. Reproduced from [51] with permission from the authors.

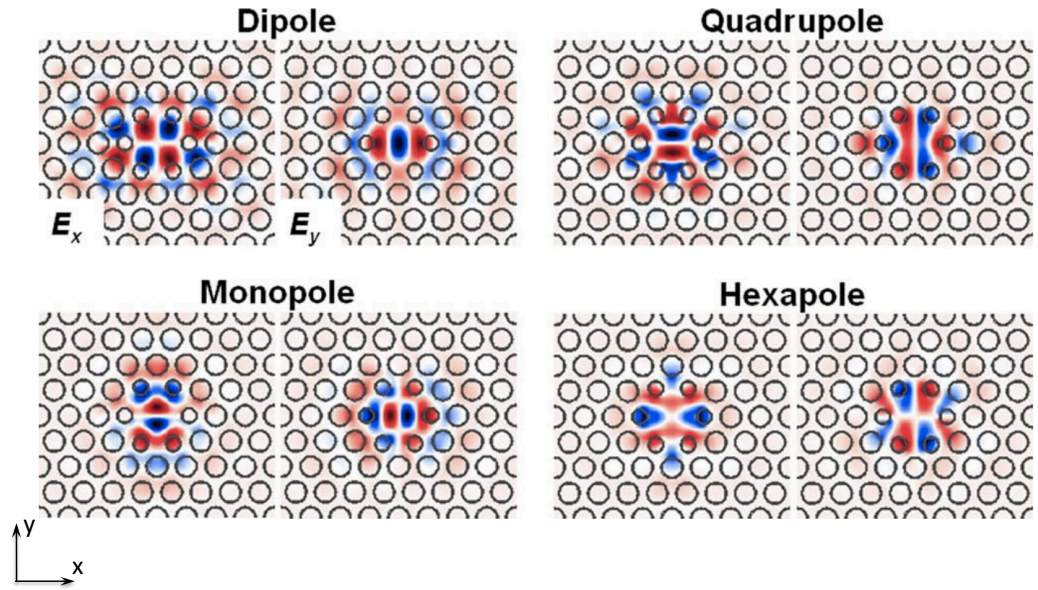

Figure 3.8: Electric field profile for monopole, dipole, quadrapole, and hexapole modes of a modified single defect photonic crystal cavity. Reproduced from [51] with permission from the authors.

3.2.1 Effects of feedback from the substrate

Let h be the air-gap size between the photonic crystal membrane and the underlying substrate; the device structure is shown in Figure 3.9(a). The background air-holes have radii of $R = 0.35a$. The air-holes nearest to the defect cavity are shrunk to $Rm = 0.25a$. Then to break the six-fold symmetry, two opposite air-holes are enlarged by $Rp = 0.05a$. We present an example of the effect of substrate feedback using the modified hexapole mode shown in Figure 3.10 [32]. h is varied between $0.5a$ and $5a$; $\lambda = 1.3$ μm $= 0.29a$. Three types of substrate are used in the simulations: perfect electric conductor (PEC), InP dielectric constant, and dielectric function of gold at room temperature fitted to the Drude-Sommerfeld model given by Equation (2.23), where $\varepsilon_\infty = 10.48$, $\omega_p = 1.38 \times 10^{16}$, and $\gamma_c = 1.18 \times 10^{14}$ [28]. Gold is used, because it is one of the least lossy metals at $\lambda = 1.3$ μm. 3D FDTD simulations show that cavity Q and far-field radiation pattern vary as a function of h with a periodicity of 0.5λ. For example, Q reaches its minimum at $1.75a$ and $3.5a$, corresponding to 0.5λ. This periodic behavior maintains the same trend regardless of substrate material, though the effect is most pronounced with a PEC, weakest with a dielectric, and medium

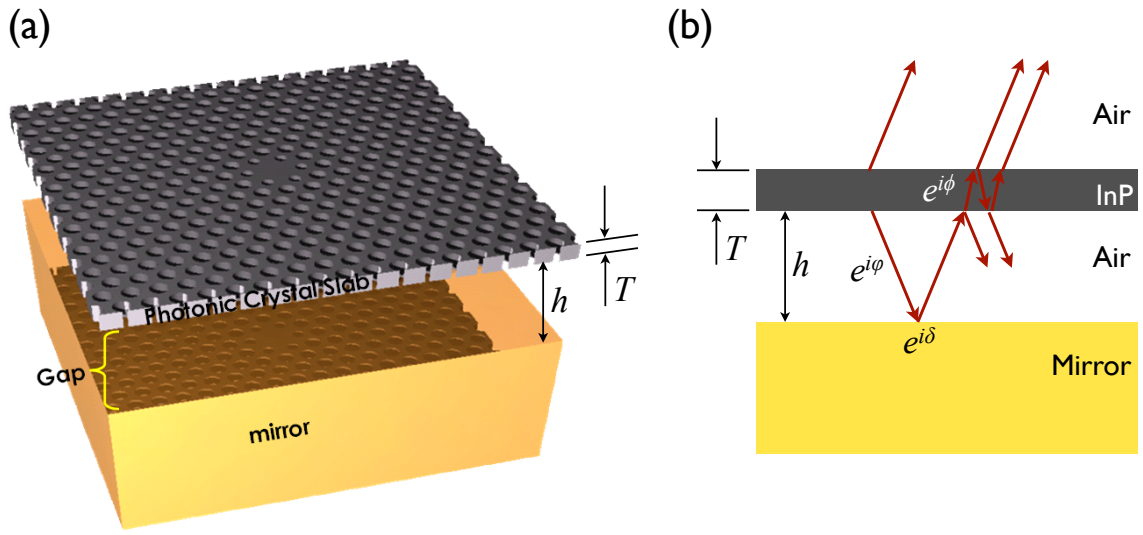

Figure 3.9: Schematic of device structure: (a) tilted view of the photonic crystal slab suspended over a substrate mirror, which can be a metal, DBR like those used in VECSEL, or simply a flat-surface dielectric such as InP; (b) side view of the same structure, red arrows indicate the path of emitted light from the photonic crystal cavity in the plane wave interference model.

with a room temperature metal substrate, due to difference in the materials' reflectivity.[2]

The 0.5λ periodicity calls to mind the analogy of a dipole emitter in a planar Fabry-Pérot cavity that can be modeled using plane wave interference [122, 129]. Kim and colleagues also used the wave interference model to explain how radiation efficiency and emission directionality changes as a function of slab thickness T and air-gap h [32, 51]. Figure 3.9(b) shows a schematic of the model. The multiple reflection path taken by light emitted from the photonic crystal cavity is shown as red arrows. The model makes the simplifications that the photonic crystal slab is approximated as a uniform dielectric layer having an effective index [130], the lasing mode is approximated as a dipole point source at the middle of the slab, emitted radiation is described by simple scalar plane waves, and the substrate reflector is far enough from the photonic crystal slab that it does not perturb the resonant mode too much [51, 122]. In the figure, φ is the phase the plane wave picks in traveling across h, δ is the phase addition due to reflection at the mirror surface, and ϕ is the

[2]PEC is an idealized material that reflects all light, room temperature gold has slightly lower reflectivity and some ohmic absorption, and InP has a reflectivity of ~ 0.3 at 1.3 μm. As h shrinks, absorption due to gold becomes more severe. When a semiconductor substrate like InP is too close to the photonic crystal membrane, e.g. $h < a$, light tunnels through the air-gap and leaks through the substrate; as a result Q suffers drastically.

With all three materials, the PBG confinement of light breaks down as $h \to 0$—when the substrate is InP, there is no more optical confinement and light leaks through the substrate; in the cases of PEC or gold, the photonic band structure is equivalent to that of slab thickness of about $2t$. We will investigate this structure further in Section 3.3.

phase from traveling across slab thickness T. Using the model and validated by FDTD simulations, enhanced vertical emission due to constructive plane wave interference occurs when $e^{2i\varphi}e^{i\delta}e^{i\phi} = 1$ [51]. Assume phase change due to reflection at the mirror surface is $\delta = \pi$, and the slab thickness is often $T \approx (\lambda/2n_{eff})$ to maximize the PBG, i.e. $\phi \approx \pi$, then h should be about $m\lambda/2$, $m \in I$, to maximize emission in the vertical direction.

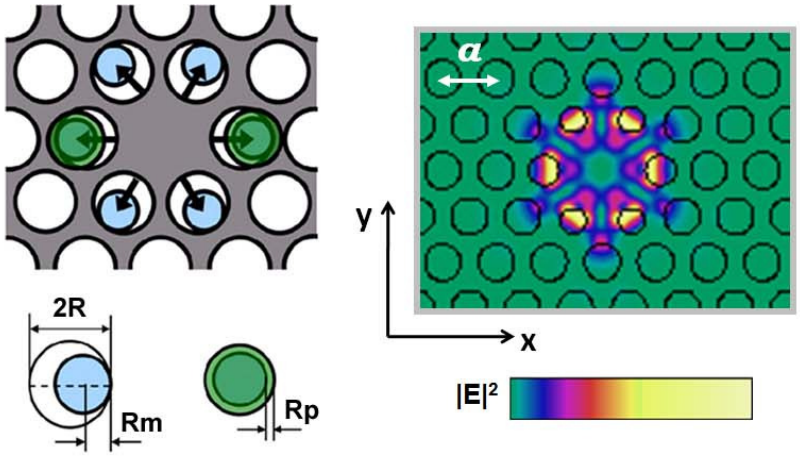

(a)

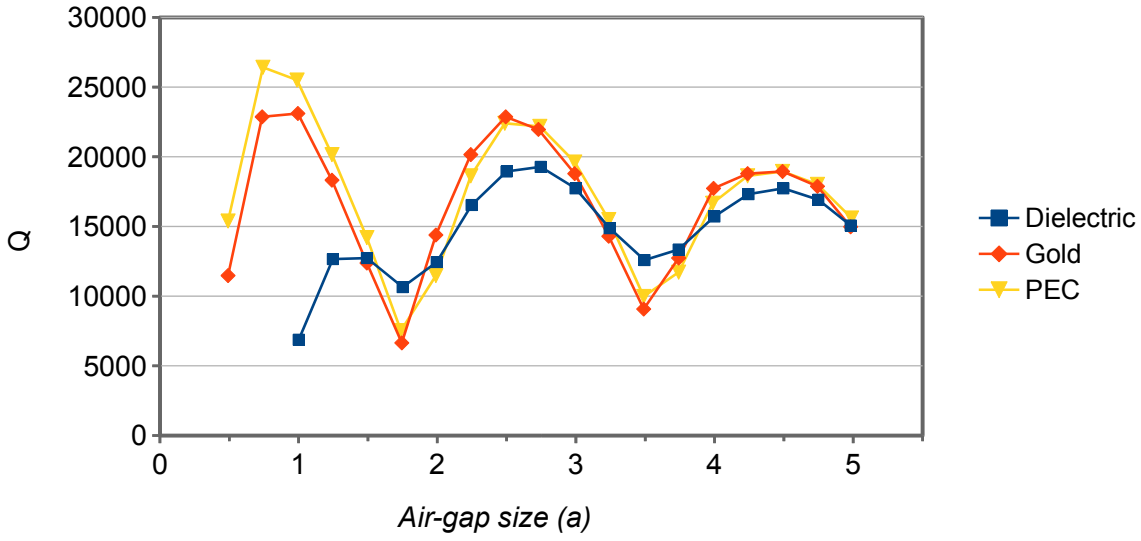

(b)

Figure 3.10: Q of the modified hexapole mode varies as a function of air-gap size h: (a) modified nearest air-holes and the hexapole mode profile, $R = 0.35a$, $Rm = 0.25a$, and $Rp = 0.05a$; (b) variation in Q as a function of h in units of a. Near-field profile changes very slightly with h.

In our modified hexapole example, the modulation in Q is caused by the substrate mirror's effect on the laser cavity's radiation characteristics. We would then expect that the far-field radiation pattern would be somehow affected as well. We used FDTD simulation with methods outlined in Section 2.2.2 to calculate how far-field radiation changes as h varies from 0.7λ to 1.4λ. Photonic crystal slab thickness was $T = 0.9a$ and a PEC substrate was assumed. We found that the presence of the substrate mirror does not change the near-field mode profile much; however, the far-field patterns show a sensitive dependence on h, see Figure 3.11. Again a periodicity of 0.5λ is noticeable—radiation patterns with $h = 0.7\lambda$ and 1.2λ show similar divergence, and those with $h = 0.9\lambda$ and 1.4λ exhibit vertically emission with similarly small divergence angle. Moreover, the most spread out far-field pattern roughly corresponds to when Q is at a local maximum ($0.7\lambda = 2.4a$, $1.2\lambda = 4.13a$), and directional far-field emission is when Q is nearing its local minimum ($1\lambda = 3.45a$).

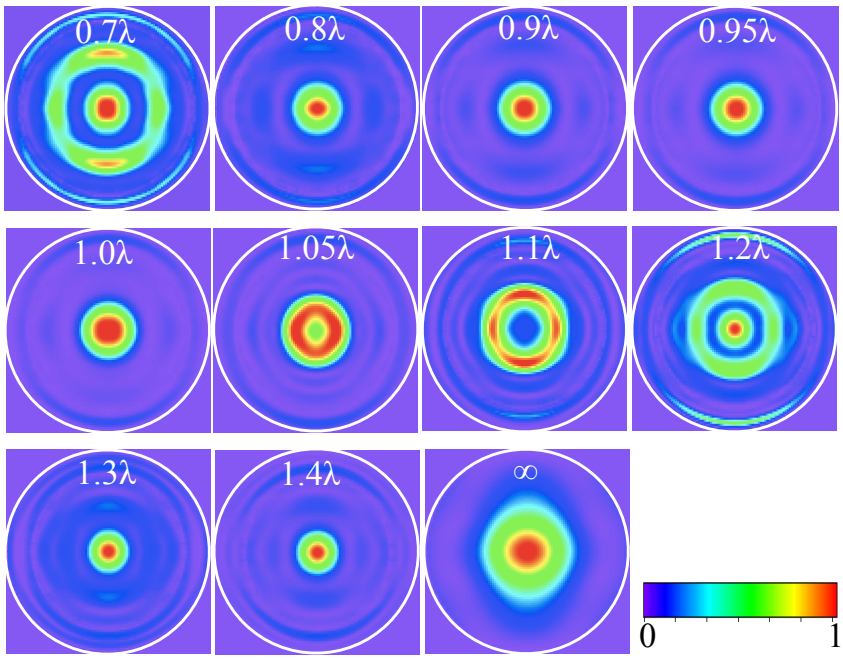

Figure 3.11: FDTD simulation results of far-field radiation pattern from the modified hexapole mode, as a function of h variation from 0.7λ to 1.4λ. ∞ indicates the far-field in the absence of a substrate. Seen in the $-z$ direction from the directly above the device surface, radiation detected over the hemisphere shown in Figure 2.3 is mapped into 2D using $x = \theta\cos\varphi$ and $y = \theta\sin\varphi$. Numbers on each

3.2.2 Cavity characteristics of photonic crystal on a metal substrate

In the previous section, we concerned with the case where the air-gap between the photonic crystal slab and the substrate is large enough, approximately $h > a$, such that the photon confinement mechanism of PBG is still effective. As $h \to 0$, however, this is no longer the case. When the photonic crystal slab rests directly against a dielectric substrate such as InP, there is no more confinement, light leaks into the substrate. When the slab is bonded to a PEC or gold, a weaker confinement remains. For a slab thickness of $T = 0.9a$, $Q > 1000$ in the case of PEC, and is but a few hundred for gold. Such a low Q is insufficient for building room temperature CW lasers. That is too bad, as metals have very good thermal and electrical conductivity, a characteristic that would have been useful to relieve microlasers' huge thermal resistance and to make electrical contact for current-injection operation. Metal substrates also do not support downward propagating optical mode as do dielectric substrates, so the device only emits light through its top surface, showing promise of increased collection efficiency. Moreover, when the photonic crystal slab rests directly on the reflective metal, we eliminate a source of external feedback to the microlaser, potentially simplifying device design and analysis. In this section, we attempt to increase Q of this *photonic crystal bonded on metal* structure to a level at which room temperature CW lasing may be possible, and study its optical confinement mechanisms. Once a satisfactory Q is achieved, we tune the design parameters to obtain directional emission with very good linear polarization. The device schematic is given in Figure 3.12(a). We investigate, particularly, the modified dipole mode, whose mode profile is shown in Figure 3.12(b).

We postulate two main channels of optical loss, which we need to mitigate in order to raise Q. First, metal absorption loss—with an optically-thin slab, we would expect a significant electromagnetic field overlap with the gold substrate, leading to appreciable material absorption due to the non-zero ε_I in room temperature gold. Second, photonic crystal bonded on metal has a diminished PBG, if it has a PBG at all, thus in-plane confinement is compromised.

One way to decrease modal overlap with the gold substrate is to simply increase the photonic crystal slab thickness T. Figures 3.13(a)–(b) show the 3D FDTD simulation results of effective mode

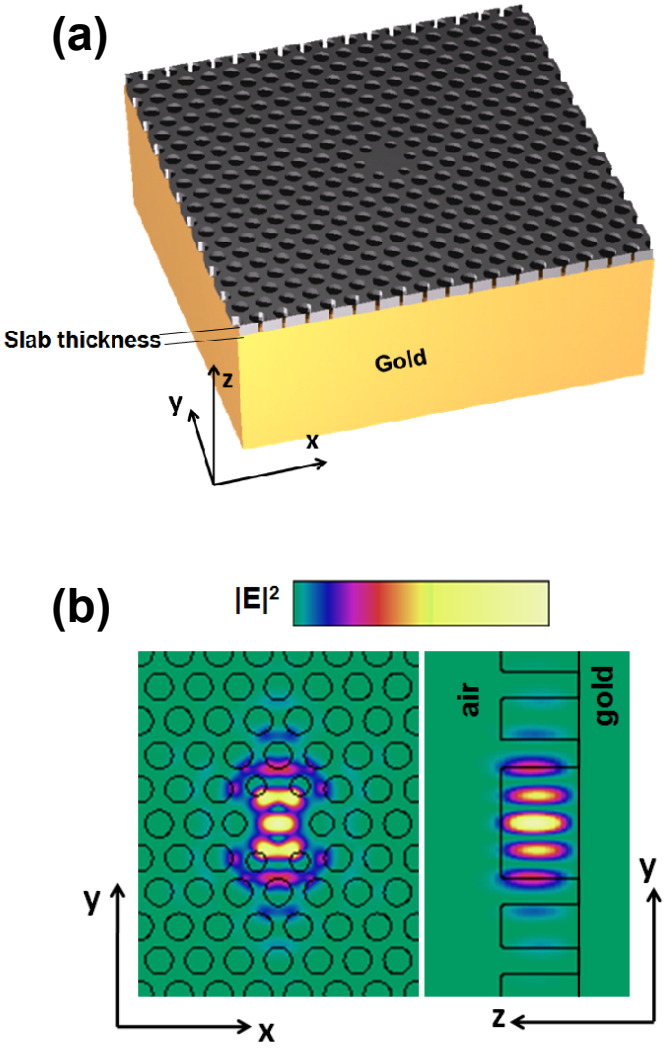

Figure 3.12: Modified single-defect cavity on gold substrate: (a) schematic of device structure; (b) mode profile of the modified dipole mode

volume V_{eff} and Q as T increases from 300 nm to 1800 nm. At $T = 1800$ nm thickness, lattice constant a is set to 300 nm to keep the fundamental mode wavelength at $\sim$1.3 μm, the slab is now optically very thick with $T = 6a$. Interestingly, Q increases steadily as well. $Q > 600$ when $T > 2a$ (600 nm), and $Q > 3000$ when $T > 5a$ (1500 nm). What's more, Q seems to increase indefinitely with increasing T. On the other hand, unsurprisingly, V_{eff} increases monotonically though not drastically. $V_{eff} \approx (\lambda/n)^3$ when $T \approx 720$ nm. Our concern with V_{eff} is chiefly due to its effect on the amount of Purcell effect we can expect from the cavity. As discussed in Section 2.1.4, the expression for Purcell factor takes different forms. When we assume the ideal case of a single emitter (e.g. a quantum dot) located in a medium of refractive index n without regard for the emitter's spectral broadening and polarization misalignment with the cavity mode, F_p is given by Equation (2.27) $F_p = (3Q/4\pi^2 V_{eff})(\lambda/n)^3$ [11], which is the maximum achievable spontaneous emission rate enhancement. When we consider realistic room temperature laser cavities, where the gain material such as QWs exhibits homogeneous broadening so its spectral linewidth is wider than that of the cavity's and the dipole emitters do not align perfectly with the electric field of the lasing mode, F_p is given by Equation (2.28) $F_p = (a_p/2\pi^2 V_{eff})(\lambda/\Delta\lambda)(\lambda/n)^3$ [19]. F_p as a function of increasing T, calculated using either expression, is shown in Figure 3.13(c)–(d); (d) is calculated using emitter properties of the widely used InGaAsP QWs, where the normalized average projection component of electric dipoles on the electric field of the laser mode $a_p = 0.4$, the spectral width of the QWs is $\Delta\lambda = 8.8$ nm due to homogeneous broadening of 4.3 meV [19, 131]. While the idealistic F_p increases to fabulous values, $F_p = 120$ when $T = 1500$ nm, the values calculated using Equation (2.28) show that realistic F_p could show the opposite trend, depending on material properties.

At this point, the seemingly indefinitely increasing trend in Q requires a closer look. We know that PBG closes in optically-thick slabs [66]; it is certain to have done so when $T \to 6a$. Using 3D FDTD and MPB from the Joannopoulos Lab at MIT, we simulate and plot band structures of $T = 450$ nm triangular lattice photonic crystals on room temperature gold, shown in Figure 3.14. For comparison, band structures of the same photonic crystal on PEC or suspended in air, and that of an air-suspended $T = 900$ nm slab are also presented. We plot seven or eight lowest order

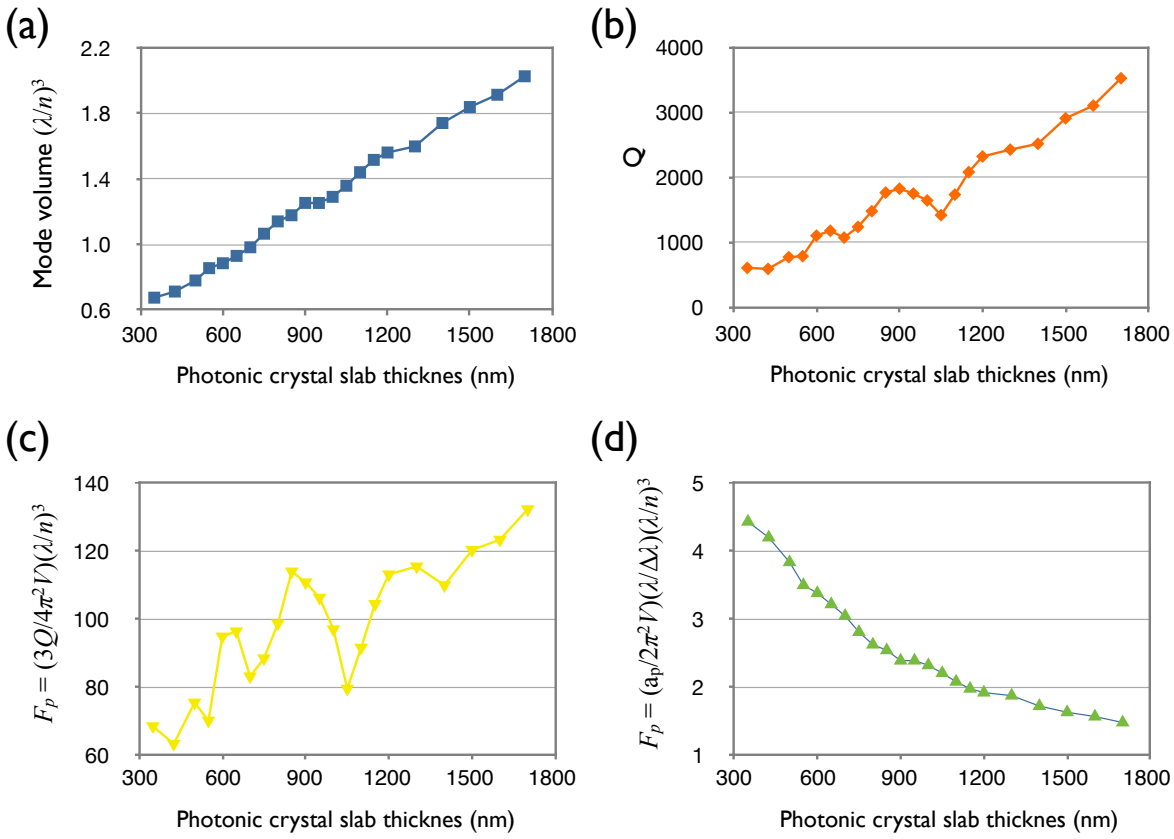

Figure 3.13: Modified dipole mode characteristics of photonic crystal slab bonded on gold, as functions of slab thickness T: (a) effective mode volume in unit of $(\lambda/n)^3$; (b) cavity Q; (c) Purcell factor F_p calculated using Equation (2.27); (d) Purcell factor F_p calculated using Equation (2.28)

modes; higher frequency ones are ignored. Here the lattice constant is $a = 320$ nm, $\lambda \approx 1.3$ μm, the resonant frequency is then $a/\lambda \approx 0.25$. Though $T = 450$ nm and greater than $\lambda/(2n)$, there is still an appreciable TE-like bandgap when the slab is suspended in air. When it is on a metal or PEC substrate, however, there is no more bandgap. To see why this is so, we look at the mode profile of each band. Shown in Figure 3.14(e), FDTD results for both gold and PEC substrates are compared side by side, with panel colors corresponding to the band color code in Figure 3.14(a)–(b). The presence of gold or PEC substrate supports surface plasmon modes, adding new bands to the purely dielectric dispersion diagram in Figure 3.14(c), with the slight difference that surface modes on PEC reside completely in the dielectric, but with gold a portion of the mode overlaps with the metal. Bands of non-plasmonic modes shift closer to each other too, since they see a different effective index when the slab is surrounded by air or adjacent to a reflector substrate. These changes fill up the in-plane PBG.

We also note that Figure 3.14(a), (b), and (d) look awfully similar to each other, with (b) and (d) being almost identical. This phenomenon is not surprising when we think about our metallo-photonic crystal using the method of images [1]. TE-like modes in a photonic crystal with slab thickness T on PEC is equivalent to TM-like modes in one with thickness $2T$. Gold substrate has a finite $\Re\{\varepsilon\}$ and $\Im\{\varepsilon\}$, so the equivalence is approximate, but qualitatively correct. Indeed, if we apply the same method to the mode profiles, bands 1, 5, 6, and 7 in Figure 3.14(e) are but modes with an antinode mid-slab in the photonic crystal of thickness $2T$, whereas bands 2, 3, 4, and 8 have a node mid-slab. We can thus analyze many of the cavity characteristics, such as optical confinement mechanism for the metallo-photonic crystal, as we would a air-suspended thick-slab device with twice the dielectric thickness. This very much simplifies numerical simulations: the metal substrate presents a rapid evanescent field decay inside it[3], requiring fine resolution of 1–2 nm, and it breaks the symmetry in the z-direction, further increasing computation memory and time requirements; in contrast, an air-suspended dielectric thick-slab can be simulated using coarser resolution of 10–20 nm pixel size and also enables us to use odd or even symmetry in z.

[3]The evanescent field penetration in metal is simply the skin depth, usually ∼20 nm.

With no in-plane PBG modes, the optical confinement in our thick-slab photonic crystal can be understood based on dispersion along the z-direction. Instead of the ω-$k_{\|}$ band diagrams we are used to for conventional photonic crystal slabs, we look at the ω-k_z relations. This we discuss in more detail in the subsequent Section 3.3 on thick-slab photonic crystal cavities.

The fact that we can achieve Qs of a couple of thousand is very encouraging for building room temperature CW current-injection lasers. In designing an electrically-pumped device based on this geometry, a thin low-index dielectric can be inserted between the photonic crystal slab and the gold substrate—to further reduce mode overlap with the metal—and with a small gold-filled aperture under the cavity to act as a current aperture. Furthermore, the results suggest that we do not have to adhere to optically-thin photonic crystal cavities. We demonstrate in Sections 3.3 and 5.4 lasing in thick-slab single-defect photonic crystal cavities, which potentially have lower thermal resistance and give us more room to design gradient doping in a p-i-n epitaxial QW or QD structure for current-injection operation.

3.2.3 Radiation characteristics

Now a brief interlude to look at how we can design for directional emission from the metallo-photonic crystal cavities: Consider again the model we proposed in Section 3.2.1, but with $h = 0$, where interference of emitted light comes from the slab thickness itself and the dielectric function of the metal substrate. Using 3D FDTD and near- to far-field transformation, we tune T and see how the far-field radiation pattern changes. The results in Figure 3.15(a) show that this single parameter changes things drastically. When $T = 600$ nm, emission is concentrated within a $\pm 15^\circ$ cone, yet $T = 700$ nm results in a divergent emission where field intensity is evenly distributed within a $\pm 60^\circ$ angle. At the optimum $T = 600$ nm, the radiation is also mostly linearly polarized in the x-direction, as shown in Figure 3.15(b), promising easy coupling into optical fibers or waveguides.

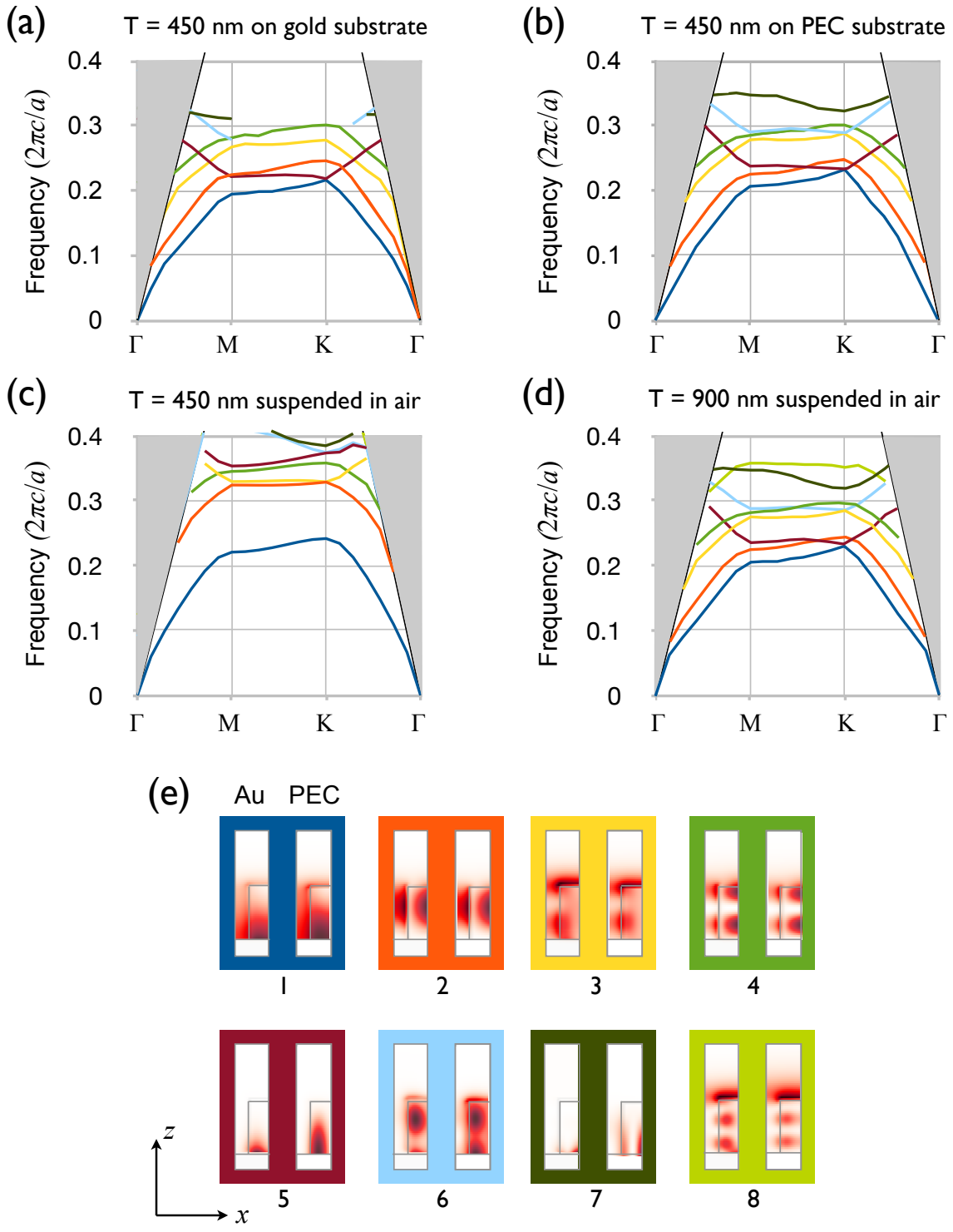

Figure 3.14: Band structures (dispersion relations) of $T = 450$ nm and $T = 900$ nm triangular lattice photonic crystal: (a) TE modes in $T = 450$ nm slab on room temperature gold substrate; (b) TE modes in $T = 450$ nm slab on PEC substrate; (c) TE modes in $T = 450$ nm slab suspended in air; (d) TM modes $T = 900$ nm slab suspended in air; (e) $|E|^2$ mode profile of the different bands in (a) and (b), left panels are for gold substrate, right panels are for PEC substrate, panel colors correspond to color code in the band structure diagrams.

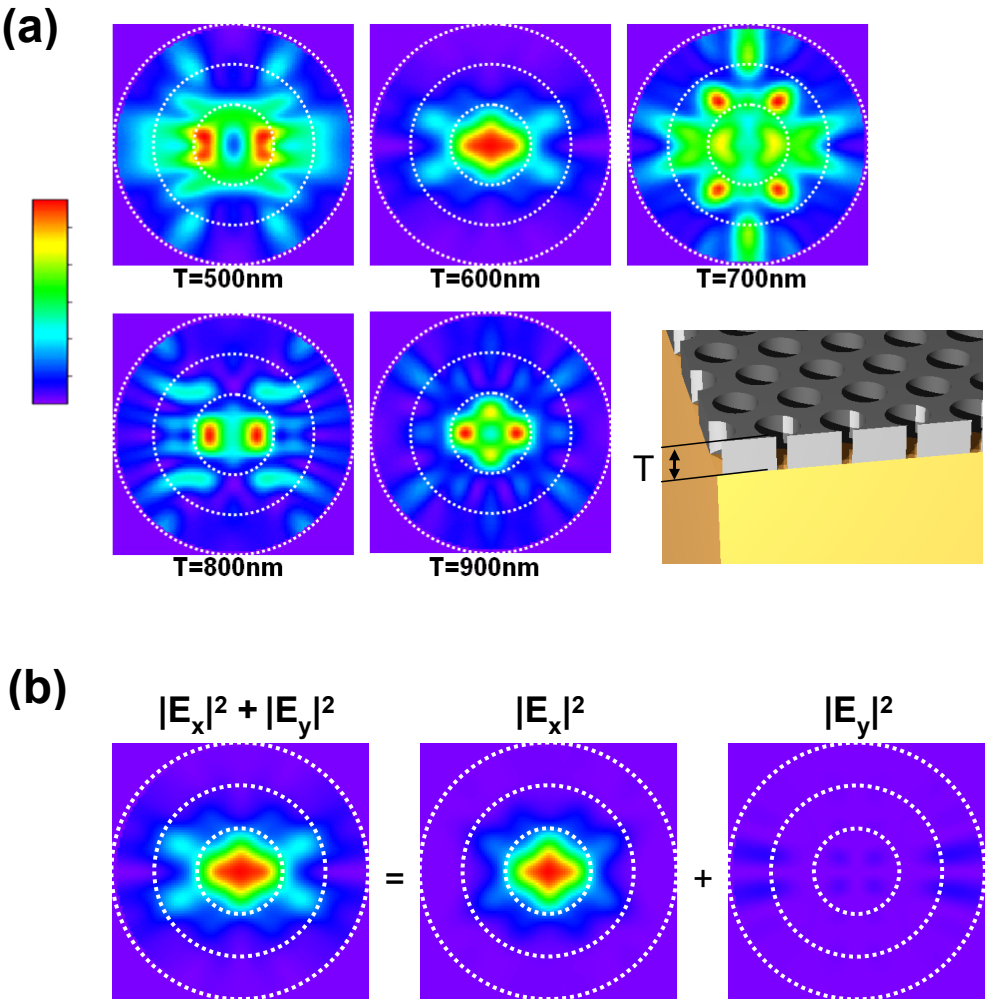

Figure 3.15: Far-field radiation pattern of the modified dipole mode on a gold substrate: (a) far-field pattern modulation due to changes in T; (b) linear polarization decomposition of far-field radiation from a $T = 600$ nm slab.

3.3 Thick-slab photonic crystal lasers

Our investigation into photonic crystal bonded on metal substrate shows that in-plane bandgap is not necessary to achieve high enough Q for lasing. This prompted us to look into the possibility of lasing in optically-thick single-defect cavities [101]. Thicker slabs have the advantage of lower thermal resistance and allow us more room and freedom in designing the device's vertical p-i-n doping profile for better electrical properties. In fact, concurrent with our work, Tandaechanurat and colleagues studied the same problem, and demonstrated CW lasing at a cryogenic temperature of 4 K in a thick-slab cavity with $T = 1.1a \sim 1.6a$ [132].

Consider the modified dipole mode in an air-suspended single-defect photonic crystal cavity with a large thickness T, shown in Figure 3.16(a). The cavity design is the same as that shown in Figure 3.10(a), where $R = 0.35a$, $Rm = 0.25a$, and $Rp = 0.05$. First, let us look at the TE-like band structures of the background photonic crystal in Figure 3.16(d).[4] At $T = 1.4a$, the second guided band begins to droop down to lower frequencies in the Γ-M and Γ-K directions, decreasing bandgap. When $T \approx 2a$, PBG disappears, a resonant mode at any frequency would overlap with at least one guided band. The band structure for $T = 3a$ is just a tangle. Lack of PBG notwithstanding, FDTD simulations show that we still have well-defined resonant modes in the cavity that have the same transverse mode profile but different numbers of intensity lobes in the z-direction, as shown in Figure 3.16(b)–(c). The three modes are closely spaced spectrally. When $T = 2000$ nm, for example, resonant wavelength is $\lambda = 1324$, 1305, and 1275 nm, $Q = 5390$, 1580, and 750, and $V_{eff} = 2.45$, 2.65, and 2.86 $(\lambda/n)^3$ for the fundamental, first order, and second order modes, respectively. Moreover, Q of the fundamental dipole mode ranges between 1000 and 6000 for $T = 2a$ to $6a$ (see Figure 3.17(a)), indicating effective optical confinement mechanisms at work that were not previously considered in optically-thin slabs.

To gain some insight, we decompose Q_{tot} into $Q_\perp$ and $Q_\parallel$, where the former measures loss in the vertical direction and the latter quantifies loss in-plane in the photonic crystal slab, and plot the result as a function of T in Figure 3.17(b). When the slab is optically-thin, $Q_\perp$ depends very much

[4] There is no TM-like PBG between the four lowest guided modes. The PBG exists at a much higher frequency [66].

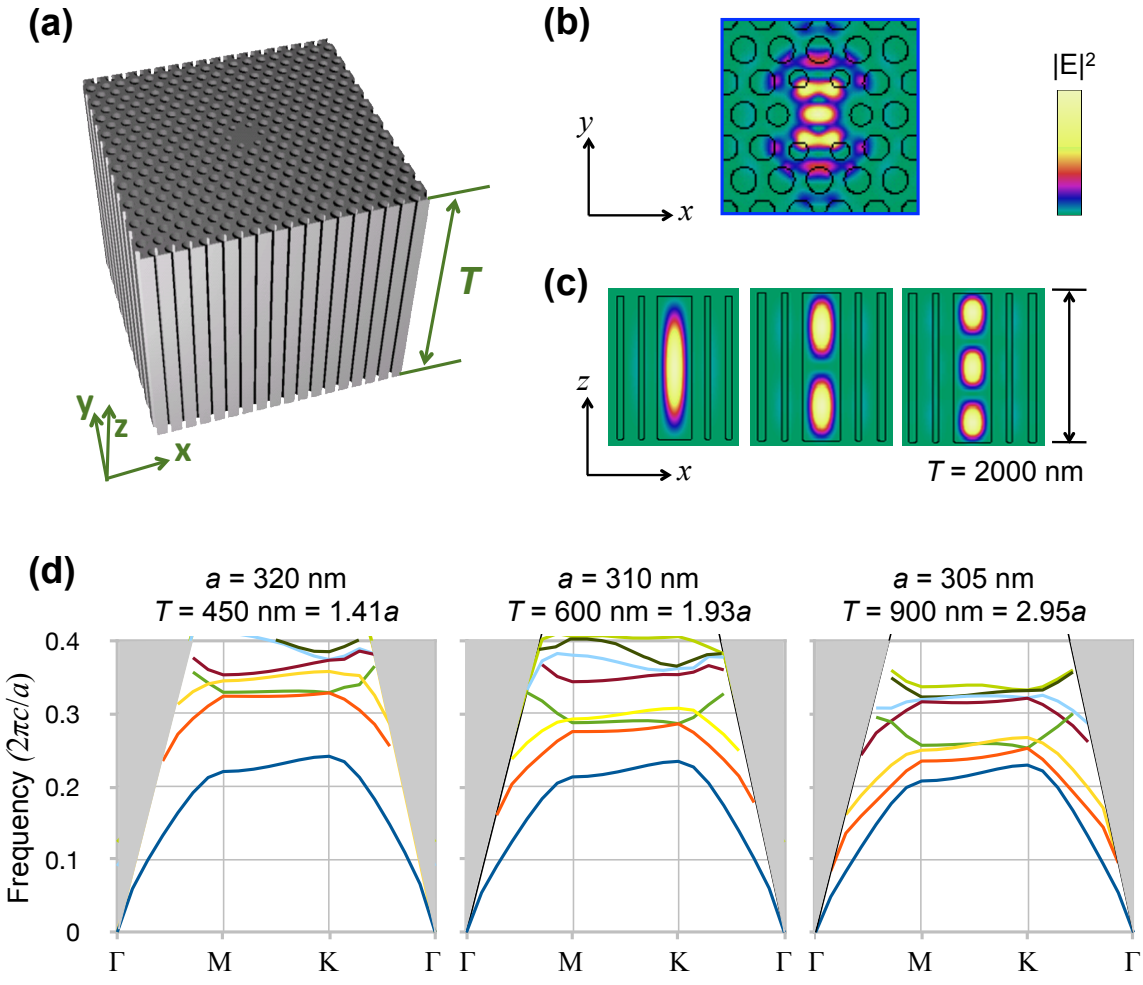

Figure 3.16: Modified dipole mode in optically-thick single-defect photonic crystal cavity: (a) schematic of device structure; (b) fundamental $|E|^2$ mode profile in x-y plane; (c) $|E|^2$ mode profile for fundamental, first, and second order modes when $T = 2000$ nm, in x-z plane; (d) band structures with increasing slab thickness from $T = 1.4a$ to $T = 3a$.

on the particulars of cavity design, such as Rm and Rp parameters [52], and is in the range of 10^4 for $T < 400$ nm, in agreement with other published results [51]. It drops to a few thousand when $T = 1.5a \sim 2a$, then shoots up to a surprising value of 6×10^5 at $T = 2000$ nm. $Q_{\parallel}$ drops from 10^4 to several thousand as PBG disappears and seems to remain in that range. This contrast in $Q_{\perp}$ and $Q_{\parallel}$ prompts one to think of vertical confinement no longer as total internal reflection in a very thin 2D slab wavelength [15] but perhaps as a vertical Fabry-Pérot in a short photonic crystal fiber. At the same time, the in-plane confinement can be understood to be due to mode mismatch between the cavity mode and guided mode(s) in momentum space, allowing only weak coupling between the two [132].

Consider a device with a very large T, which resembles a photonic crystal fiber. In the absence of both TE- and TM-like PBG in the transverse direction, our dipole mode is analogous to the index-guided modes in a fiber with a dielectric core, confined by the index contrast between the defect region and the holey photonic crystal background [66] and in contrast to the bandgap guided *Bragg fibers* usually with a hollow core [40]. We can then define a k_z and plot the waveguide dispersion in the z-direction, shown in Figure 3.17(b). We have also labeled the intersection of the fundamental, first order, and second order mode frequencies on the dispersion curve. These intersections appear to be evenly spaced in k_z, confirming a satisfied Fabry-Pérot condition [23]:

$$\Delta k_z = \pi / T \tag{3.2}$$

To translate this to the normalization used in FDTD simulation and in the figure, $\Delta k_z/(2\pi/a) = a/(2T) = 0.076$. Loss in a generalized Fabry-Pérot cavity is mainly due to waveguide propagation loss α, which in our case is due to the imperfect in-plane confinement and scattering loss at the

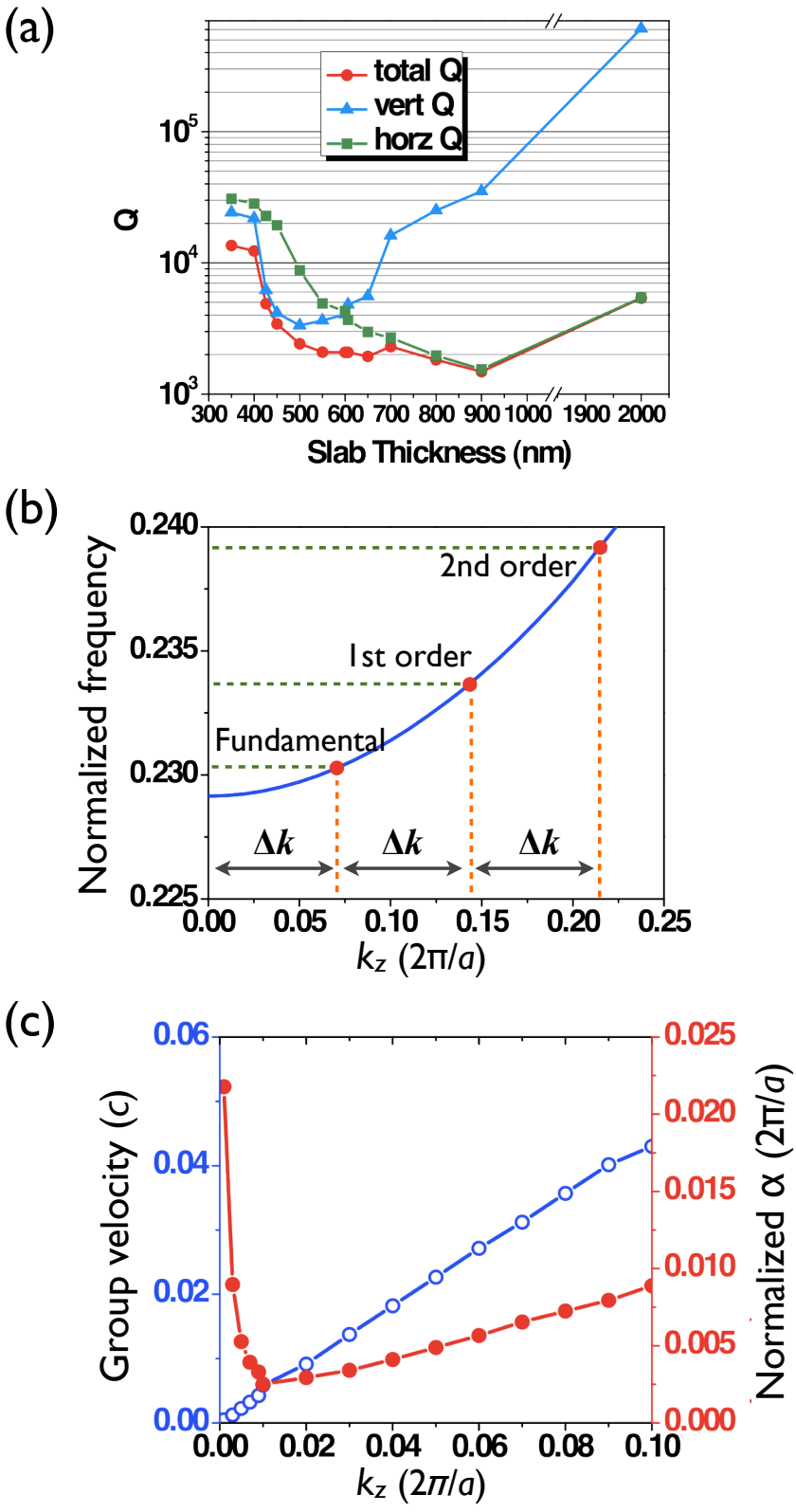

Figure 3.17: Analysis of optical confinement mechanisms in the modified dipole mode: (a) Q as a function of T and its decomposition into $Q_\perp$ and $Q_\parallel$; (b) dispersion relation ω-k_z with the fundamental, first order, and second order modes labeled; (c) group velocity v_g and normalized waveguide loss coefficient α as functions of k_z.

mirror facets, that is [71, 23]

$$\begin{aligned} \frac{1}{Q_{tot}} &= \frac{v_g}{\omega}\left[\alpha + \frac{1}{T}\log\left(\frac{1}{r_0^2}\right)\right] \\ &= \frac{v_g\alpha}{\omega} + \frac{v_g}{\omega T}\log\left(\frac{1}{r_0^2}\right) \\ &= \frac{1}{Q_{\parallel}} + \frac{1}{Q_{\perp}} \end{aligned} \tag{3.3}$$

where $Q_{\parallel}$ and $Q_{\perp}$ are expressed in terms of α and r_0 is the reflectivity of the mirror facets. We can calculate v_g from our ω-k_z dispersion diagram, $v_g = d\omega/dk$, shown in Figure 3.17(c). From the trend of $v_g(T)$ and the equation above, the steady increase in $Q_{\perp}$ as the photonic crystal slab becomes thicker ($T > 2a$) is explained.

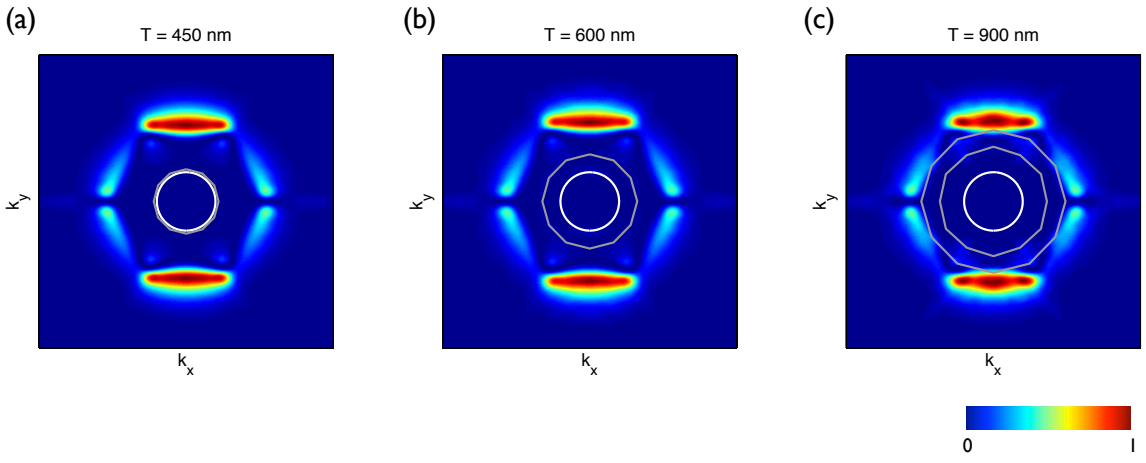

Figure 3.18: E-field intensity $|E|^2$ distribution in momentum space. T = 450 nm ($1.40a$), 600 nm ($1.94a$), and 900 nm ($2.95a$). White circle indicate the light cone. Grey lines are the locations of the guided modes at the resonant frequency, based on the equifrequency contours' intercepts with the Γ-M and Γ-K vectors.

Transverse optical confinement by index contrast is a plausible explanation, but it does not explicitly address the potential coupling between the resonant mode and the propagating modes guided by the photonic crystal slab as we see in the band diagrams (Figure 3.16(d)). We postulate that there is little coupling between the resonant mode and the guided modes due to momentum mismatch. To confirm, the modified dipole mode's E-field intensity distribution $|E|^2$ in momentum space is calculated using 3D FDTD for several slab thicknesses $T = 1.40a, 1.94a, 2.95a$, as shown in Figure 3.18. The light cone is indicated by the white circles. The equifrequency lines for the guided

modes at the resonance frequency are drawn in grey lines by interpolating their locations in the Γ-M and Γ-K directions. The majority of the resonant mode resides far from the light cone, and the guided modes do not intercept areas of high intensity. Thus moderate Qs can be achieved despite the lack of a PBG in optically-thick photonic crystal slabs.

3.4 Coupled-cavities for enhanced far-field emission directionality

Coupled-cavity photonic crystal lasers have been studied to increase lasing power and differential quantum efficiency [133]. Single mode operation can be achieved from coupled cavities even when they are individually multimode, as the constituent cavities act as mode filters for each other [134]. At the same time, most of the wavelength-scale laser cavities are so far optimized for high Q and small V_{eff} in attempt to maximize F_p, but are not particularly designed for efficient light extraction. Extraction methods such as evanescent coupling to a tapered microfiber [83] and monolithic integration with a passive waveguide using wafer regrowth techniques [135] have been demonstrated; lasers with highly directional surface emission can provide an alternative way to achieve efficient free-space light coupling [51]. To further investigate and improve on these issues, we have designed coupled photonic crystal cavities that exhibit single mode lasing and enhanced emission directionality.

Our devices are formed in an InP slab with a thickness T of 240 nm on top of a 1.16 μm thick sacrificial InGaAs layer. Cylindrical holes etched into the slab in a hexagonal lattice form the photonic crystal. One missing air hole forms a simple H1 cavity; 3 or 5 missing air holes along the Γ-K direction form an L3 or L5 cavity, respectively. We laterally couple these cavities as shown in Figure 3.19: Design A consists of L3-L5-L3 cavities, Design B consists of H1-L3-L5-L3-H1 cavities. FDTD simulations show that for both designs there are resonant modes with Q of a couple hundred within the InP/InAsP QWs' gain spectrum; however, there is one prominent mode with $Q = 1690$ for Design B, and $Q = 3110$ for Design A. Thus, we can expect single-mode lasing from these designs.

Efficient free-space coupling requires the laser to have a directional far-field radiation pattern.

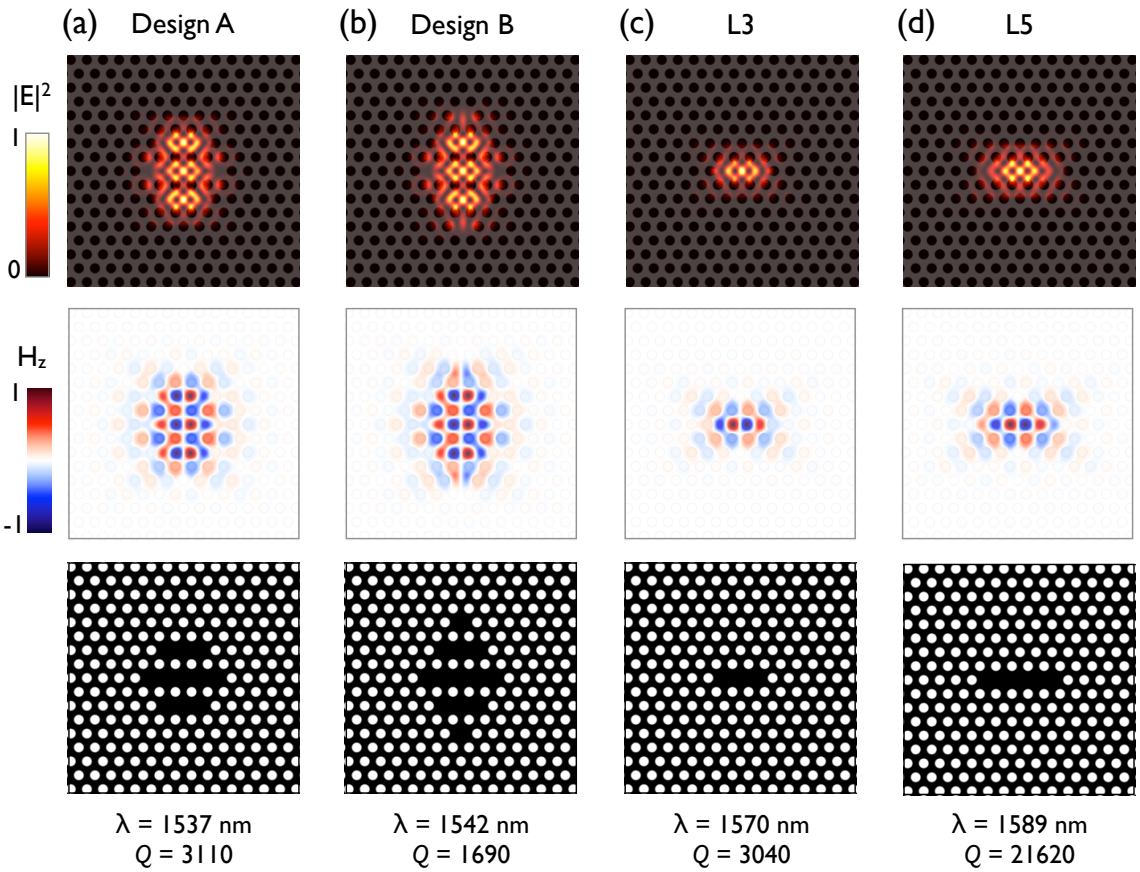

Figure 3.19: $|E|^2$ and H_z mode profiles and top view device schematic of coupled-cavity designs, L3 and L5 cavities are shown for comparison: (a) coupled-cavity Design A; (b) coupled-cavity Design B; (c) L3 cavity; (d) L5 cavity.

The proposed schemes so far for directional emission from photonic crystal microcavity lasers involve fine modification of the air-holes in the vicinity of the main cavity [51, 136]. In fact, Kang and colleague have experimentally confirmed the effect of nearest air-hole tuning on the single-defect laser's far-field pattern from a hexapole mode [137]. Here, we show that far-field directionality can be engineered by proper arrangement of coupled cavities to a level that is satisfactory for practical application without fine-tuning the PhC air-holes. We calculate the coupled cavities' far-field radiation pattern using methods described by Kim et al. [51], the results are shown in Figure 3.20. While the PhC cavities' mode profile and Q hardly change with the presence of the substrate under the suspended PhC slab, the far-field pattern is noticeably affected, making the reflectivity and distance of the substrate an important design parameter. Single L3 or L5 cavities radiate light with poor directionality. Most of Design A's emission is at $\pm 60^\circ$ in the x-direction, making free-space light collection difficult. Under the comparison, Design B has much enhanced emission directionality along the laser's surface normal, suggesting efficient free-space coupling. For Design B of a coupled-cavity laser suspended 1.16 μm above the InP substrate as is our case, the emitted light has a Gaussian-like dominant center peak. The center emission lobe represents $\sim$40% of the light emitted from the laser's top surface and has a FWHM beam divergence of 20° from surface normal in the x-direction and 8° in the y-direction.

3.5 Nanobeam photonic crystal lasers

The photonic crystal microlaser cavities we have studied so far are designed for room temperature CW lasing with potential for current-injection operation. However, their relatively large mode volume precludes strong Purcell effect in realistic QW materials.[5] Using the expression for Purcell effect in a laser cavity, Equation (2.28), reproduced here

$$F_p = \frac{a_p}{2\pi^2 V_{eff}} \left(\frac{\lambda}{\Delta\lambda}\right) \left(\frac{\lambda}{n}\right)^3$$

[5] See Section 3.2.2.

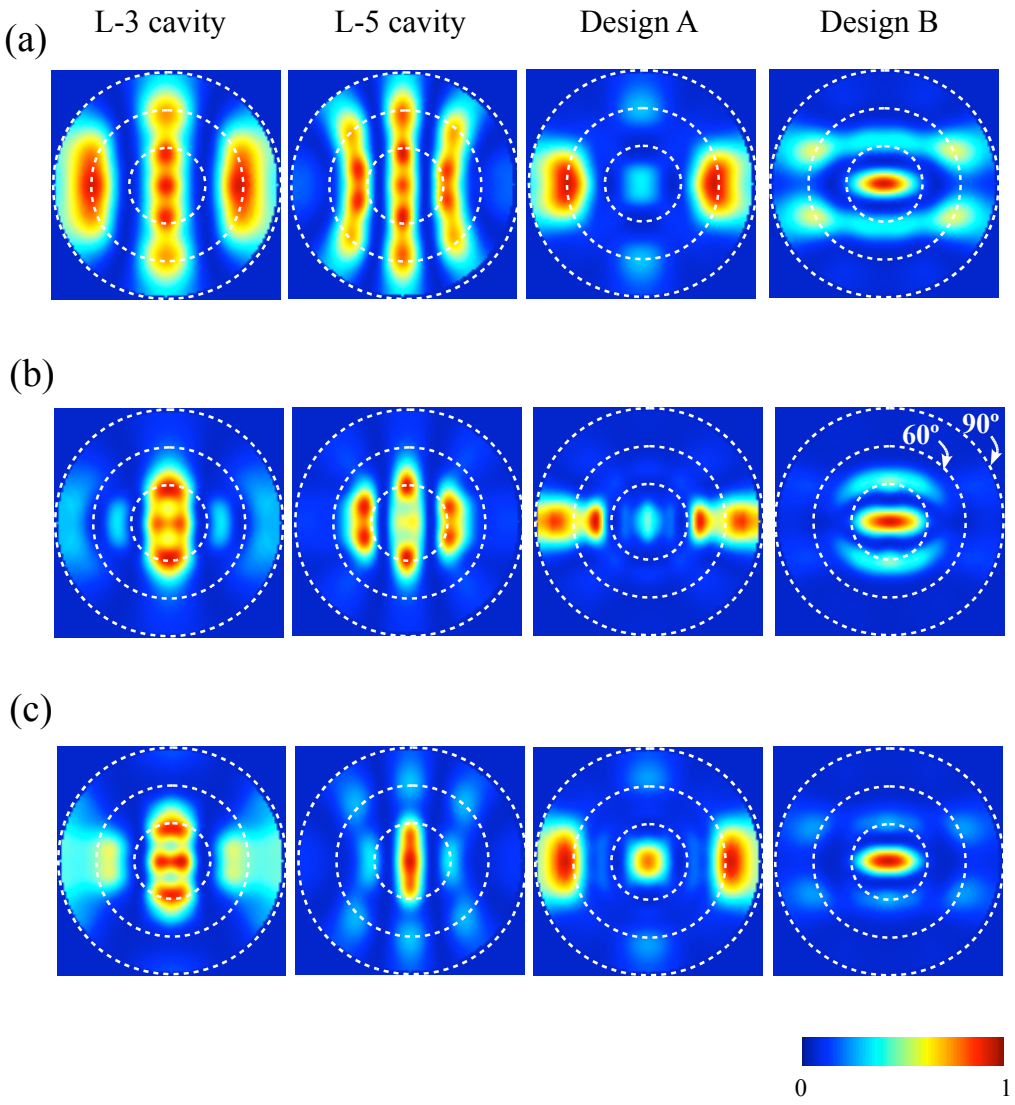

Figure 3.20: Simulation of far-field emission patterns single L3, L5, and coupled-cavity lasers: (a) suspended PhC slab with no substrate; (b) PhC slab suspended 1160 nm above the InP substrate; (c) PhC slab suspended 770 nm above the InP substrate. Dashed white circles indicate 30°, 60°, and 90° from surface normal.

recall that $\Delta\lambda$ is the spectral linewidth of the gain material or the cavity, whichever is wider. With InGaAsP, the commonly used gain material for $\lambda = 1.3 \sim 1.55$ μm, spectral linewidth due to homogeneous broadening is about 4.3 meV or 8.8 nm [131], wider than the linewidth of any cavity with $Q > 150$. High $F_p\beta$ lasers, therefore, are achieved with small V_{eff}. For example, assume $a_p = 0.4$ and $\lambda = 1.5$ μm, $F_p > 5$ when $V_{eff} < 0.7(\lambda/n)^3$, which is roughly the mode volume of a typical *L3* cavity in optically-thin slab [49]. The ultimate small mode volume cavities—with $Q > 1000$ to give a reasonable g_{th} for lasing, thus plasmonic cavities are excluded—are the point-shift photonic crystal cavity and chirped nanobeam photonic crystal, both with $V_{eff} \approx 0.3(\lambda/n)^3$ [50, 58]. Lasing with pronounced Purcell enhancement and thus soft threshold turn-on was demonstrated with the point-shift cavity on SQW InGaAsP [19]. We set out to demonstrate competitive lasing properties using the nanobeam photonic crystal cavities. They have the advantage of small on-chip footprint and no mode degeneracy like that present in microdisks and 2D photonic crystals with rotational symmetry, and they can be designed for large free spectral range (FSR) between resonant modes such that a single resonant mode overlaps with the material's gain spectrum in order to increase the amount of spontaneous emission coupled into the lasing mode, i.e. a high β. These cavities are also shown to be well-suited for coupled-cavity devices, with potentials for coupled-cavity laser arrays or optomechanically reconfigurable cavities [138, 139, 140, 141].

3.5.1 Cavity design

Design principles for nanobeam (sometimes also called *nanowire*) photonic crystal cavities have been explored since the early days of the photonic crystal field [48, 59, 142, 143, 144, 145]. From ideas outlined in Section 2.1.2, it becomes obvious that we can implement a waveguide form of DBR by drilling an array of air-holes into the waveguide along its axial direction. We start with a strip waveguide for $\lambda \approx 1.5$ μm formed by a suspended InP beam. Propagating modes in a strip waveguide decouple into two symmetry classes or polarizations: TE-like modes whose E-field is mainly in the transverse and H-field mainly in the axial direction of propagation, and TM-like modes where transverse H and axial E are the dominant field components [23]. We choose to focus on

TE-like modes for three reasons: first, highest optical confinement is achieved with the fundamental TE-like mode; second, isolated high-index dielectric spots give rise to large TM bandgap while connectivity of high-index dielectric material enhances TE bandgaps [142, 146], connected dielectric devices are much easier to implement experimentally; third, QW and QD materials can be grown for TE-polarized gain, increasing the coupling between the emitters and the cavity mode. The QW materials we have on-hand are all grown for TE-polarized gain. With these factors in mind, our suspended InP beam has a cross-section of thickness $T = 240$ nm and width $W = 450 \sim 500$ nm, forming a single-mode waveguide, both to confine light within a small cross-sectional area and to control the polarization of the guided light. More specifically, most photonic bandgap devices are polarization sensitive—PBG for TE-like and TM-like modes often exist at different frequency ranges. In a multimode waveguide, there is a possibility of TE-TM coupling due to fabrication error [147, 148], the bandgap confined TE-like modes can couple to poorly confined TM-like modes and suffer radiation loss. Moreover, we want to ensure that the resulting cavity has only one resonant mode in the wavelength range of interest, thereby potentially increase the spontaneous emission coupling factor β. Lastly, a single polarization enables efficient input and output coupling of light.

We introduce a periodic array of circular air-holes in the waveguide with lattice constant a and radius $R = 0.3a$, as shown in Figure 3.21(a). Analogous to DBRs and as shown in Figure 3.21(b), the periodic modulation in dielectric constant between $\varepsilon_{InP} = 10.1$ and $\varepsilon_{air} = 1$ leads to a bandgap for quasi-TE modes at the Brillouin zone edge where $k_x = \pi/a$. When $T = 0.51a$ and $W = 1.06a$, the bandgap is 27% of the mid-gap frequency, extending from normalized frequency of 0.286 to 0.377. For reference, our target wavelength of $\lambda = 1.5$ μm corresponds to 0.303 in frequency. To create a cavity, one can simply insert a defect, i.e. a disruption in the periodicity, between two sets of waveguide DBRs. For example, by increasing the distance between the two center air-holes, Figure 3.21(c). Q of this cavity can be tuned by changing the gap distance, however to a disappointing maximum value of a few hundred [48], due to the scattering loss at the interface of the defect and the DBRs analogous to the low-Q unmodified single defect cavities in 2D photonic crystal slabs. Therefore, the simplistic picture of an optical mode trapped between two highly reflective mirrors

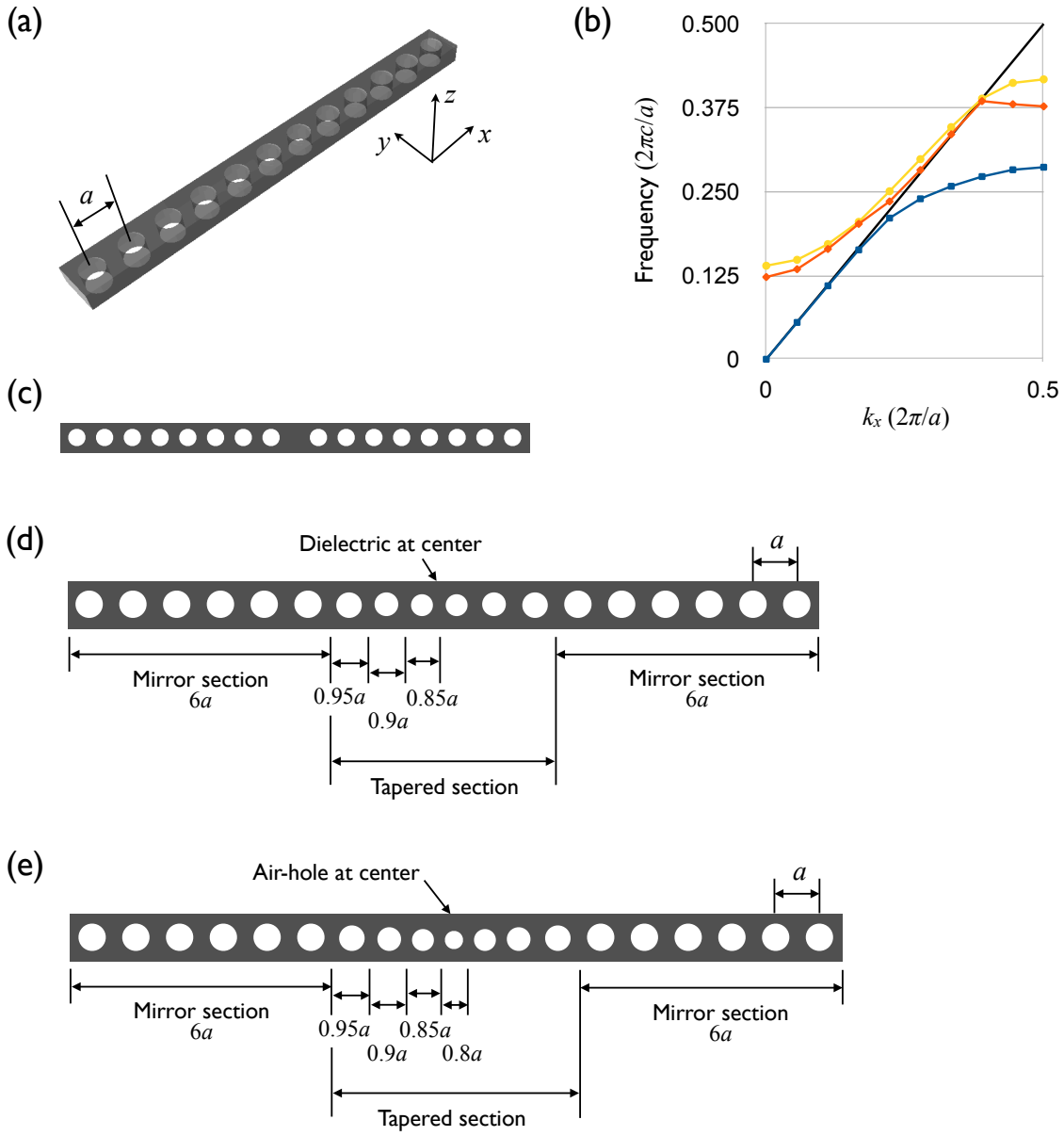

Figure 3.21: Waveguide DBR: (a) device schematic with the cartesian coordinates set-up; (b) band structure ω-k_x of the three lowest order TE-like modes, solid black line indicates the light line; (c) top view of a single defect cavity between two sets of DBRs; (d) structure of the tapered air-hole cavity with semiconductor vein in the middle; (e) structure of the tapered air-hole cavity with air-hole in the middle. $R = 0.3a$, $T = 0.5a$, $W = 1.06a$, $\lambda = 1.5$ μm corresponds to normalized frequency of 0.31.

is insufficient for designing waveguide DBR devices.

The solution to minimizing scattering loss at mirror boundaries and increasing cavity Q comes from constructing tapered air-hole gratings by fine tuning air-holes nearest to the cavity, a method that is already used in 2D photonic crystal slabs, examples include modified H1, L3, and double-heterostructure cavities [56, 49, 52]. Several models have been proposed to explain this phenomenon, including cancellation of the multipole far-field radiation [149], Bloch-wave engineering for increasing the modal reflectivity [54, 55], or momentum space tuning to minimize the resonant mode's coupling to radiative modes in the light cone [49, 150].

There are many degrees of freedom in tuning the design parameters of a tapered air-hole grating. The tapering may be introduced by narrowing or widening the nanobeam width, or tapering the air-hole size without disturbing the lattice constant, or changing both the lattice constant and air-hole radius. The tapering can be linear [58], quadratic [59], or parabolic [60]. We have not fully explored the large space of parameters for tapered nanobeam photonic crystal cavity design. We chose to begin our study with linear tapering. Design parameters of the nanobeam photonic crystal cavities are shown in Figure 3.21(d)–(e). The mirror sections each consist of six air-holes with lattice constant a and radius $R = 0.3a$. In the tapered section that forms the cavity, successive lattice constants are tapered by $\Delta = 0.05a$ for three periods, giving $0.95a$, $0.9a$, and $0.85a$. In the case where an air-hole is at the center of the cavity, its lattice constant is $0.8a$. Air-hole radius in the tapered region is scaled according to their respective lattice constant.

A tapered air-hole cavity in the nanobeam photonic crystal geometry can have one of two symmetries—it has either a semiconductor vein in the middle of the cavity and thus supports a fundamental mode whose E_y field has even symmetry across the $x = 0$ plane, shown in Figure 3.22(a); or it has an air-hole at the middle and support a fundamental mode with odd E_y symmetry across $x = 0$, shown in Figure 3.22(b). These two designs have quite different radiation characteristics. With $\Delta = 0.05a$ tapering, the former design has a Q of 30,000, while the latter has a Q of 110,000. Both Q-factors are more than enough to build a laser cavity. However, more importantly, E-field symmetries tell if the cavity can potentially achieve vertical emission, similar to our discus-

sion in Section 3.2. In both cases, the E_x field component shows odd symmetry across the $y = 0$ plane and thus interferes destructively along the z-axis. The E_y field, the major E-field component for our TE-like modes, has even symmetries across $x = 0$ and $y = 0$ planes in Figure 3.22(a). In contrast, it has an odd symmetry across the $x = 0$ plane in Figure 3.22(b). Therefore, only designs with semiconductor vein at the center of the cavity, instead of an air-hole, can potentially achieve vertical emission. For laser applications, we will focus on this design.

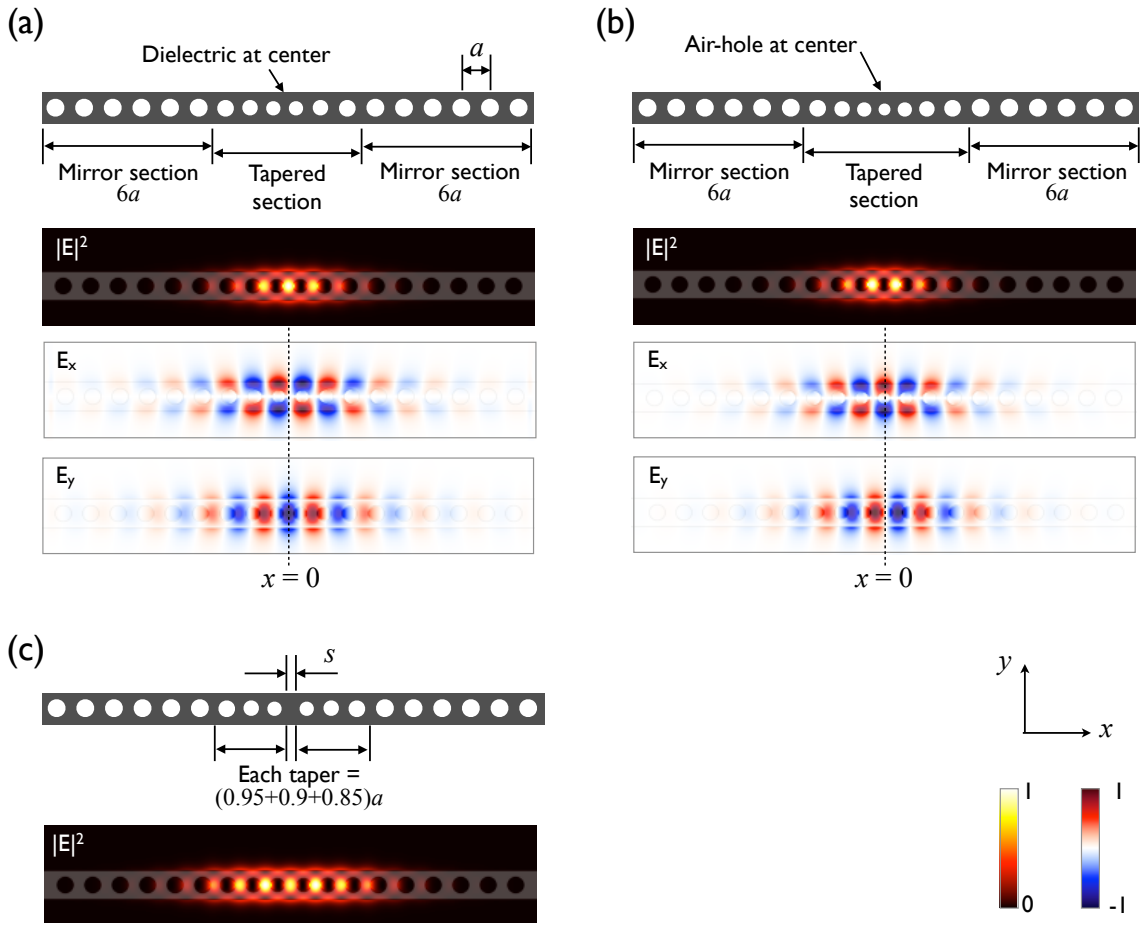

Figure 3.22: Waveguide DBR: (a) cavity formed by chirped air-holes in the *tapered section* between two sets of DBRs the *mirror sections* with $|E|^2$, E_z, and E_x profiles; (b) cavity formed by chirped air-holes between DBRs, with an air-hole at the center; (c) defect of length s can be introduced in the tapered section to tune the cavity's Q and radiation characteristics. $R = 0.3a$, $T = 0.5a$, $W = 1.06a$. The vertical dotted line in (d) and (e) indicate the $z = 0$ plane.

3.5.2 Far-field radiation directionality and effects of substrate feedback

To tune the device's emission directionality, we use the FDTD and FFT near-field to far-field transform methods detailed in Section 2.2. We find that the insertion of an extra gap size s, see Figure 3.22(c), in the middle of the cavity has the most effect on enhancing vertical emission. Figure 3.23(a) shows the evolution of far-field radiation pattern as s increases from 0 to 52 nm; the amount of emitted power contained in the 30° cone from surface normal increases from 6.5% with $s = 0$ to 33.2% with $s = 52$ nm, where the center lobe in the radiation profile represents 56% of the total surface-emitted power with a FWHM of 30° in x and 66° in y-direction. Larger s also results in lower Q. Assuming a suspended nanobeam without other dielectric structure nearby such as a substrate, Q is 30,360 when $s = 0$, but it is 4230 when $s = 52$ nm. For laser cavities, however, this may be an advantage. Investigations by T. Baba and colleagues showed that *thresholdless* lasing behavior is more pronounced with lower Q of a couple thousand. In higher Q cavities, photons coupled to the lasing mode are strongly re-absorbed below the transparency condition because of the long photon lifetime τ_{ph}. Carriers generated by re-absorbed photons may then be redistributed to non-lasing modes or non-radiative recombination, resulting in carrier loss and reduced spontaneous emission [19, 86].

Table 3.2: Summary of nanobeam photonic crystal designs

		$s = 0$	$s = 18$ nm	$s = 34$ nm	$s = 52$ nm
Effective mode volume V_{eff}		0.0537 μm^3	0.0677 μm^3	0.0883 μm^3	0.0908 μm^3
Q-factor	$[h = \infty]$	30360	12320	6720	4230
	$[h = 790$ nm$]$	19040	10570	6470	4280
	$[h = 860$ nm$]$	23690	11420	6570	4200
	$[h = 930$ nm$]$	26730	11730	6500	4080
	$[h = 1000$ nm$]$	28470	11890	6470	4030
	$[h = 1060$ nm$]$	29140	11990	6500	4050
% of emitted light in	$\pm 10°$	0.4%	4.7%	6.2%	8.2%
	$\pm 20°$	2.1%	12.8%	16.5%	21.4%
	$\pm 30°$	6.5%	20.2%	26.0%	33.2%
	$\pm 60°$	23.3%	41.2%	47.7%	55.9%

Based on our experience with 2D photonic crystal as guidance, we can expect non-negligible feedback effect from the substrate under the laser cavity, which is known to influence both Q and emission directionality [51, 151]. To estimate the effect of substrate feedback, we vary the gap

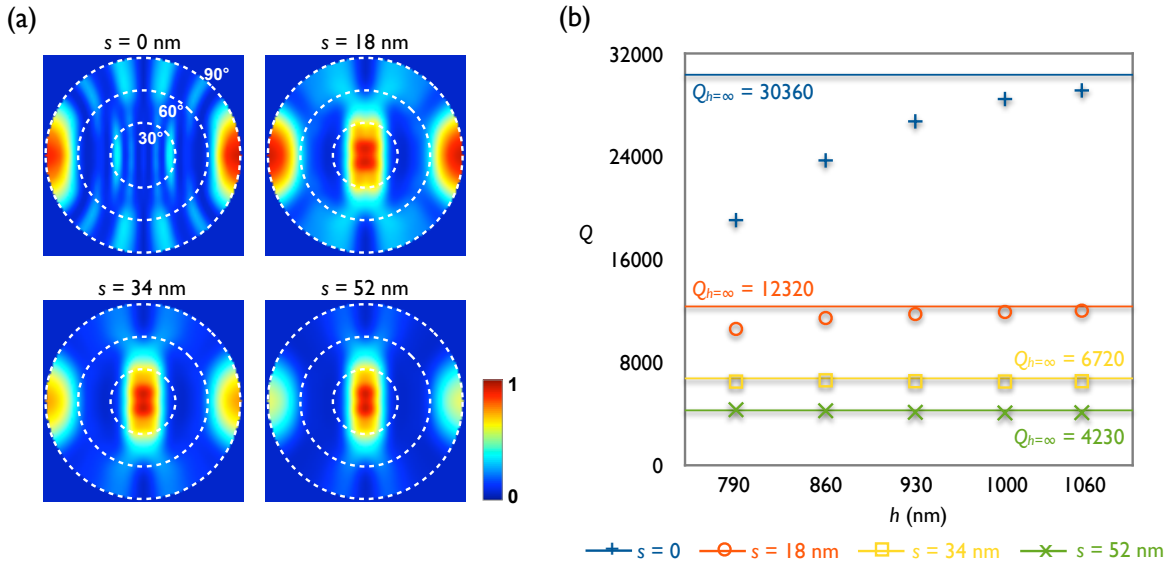

Figure 3.23: Radiation characteristics by tuning s and h the distance between the cavity and the underlying substrate: (a) far-field radiation patterns for different values of s; (b) Q-factor as a function of h for cavities with different s. $h = \infty$ indicates suspended nanobeam cavity without a substrate in the simulation space.

distance between the nanobeam and the underlying substrate h from half resonant wavelength to 1060 nm, the thickness of the sacrificial layer in the InP/InAsP QW wafer we have. For a lattice constant $a = 480$ nm, half of the resonant wavelength is 790 nm. FDTD simulated results are shown in Figure 3.23(b). We find that high Q-factors cavities with small s are more sensitive to the presence of the substrate. When $s = 34$ and 52 nm, Q oscillates within 5% of its value without a substrate.

Lastly, we look at the influence of substrate feedback on the far-field radiation pattern, see Figure 3.24. Surprisingly, unlike 2D photonic crystals such as the coupled-cavities in Section 3.4, the presence of the substrate nearby hardly changes the nanobeam photonic crystal cavity's far-field pattern at all. Regardless of h, radiation from the cavity is 80% linearly polarized in the y-direction when $s = 52$ nm and 75% y-polarized for $s = 34$ nm.

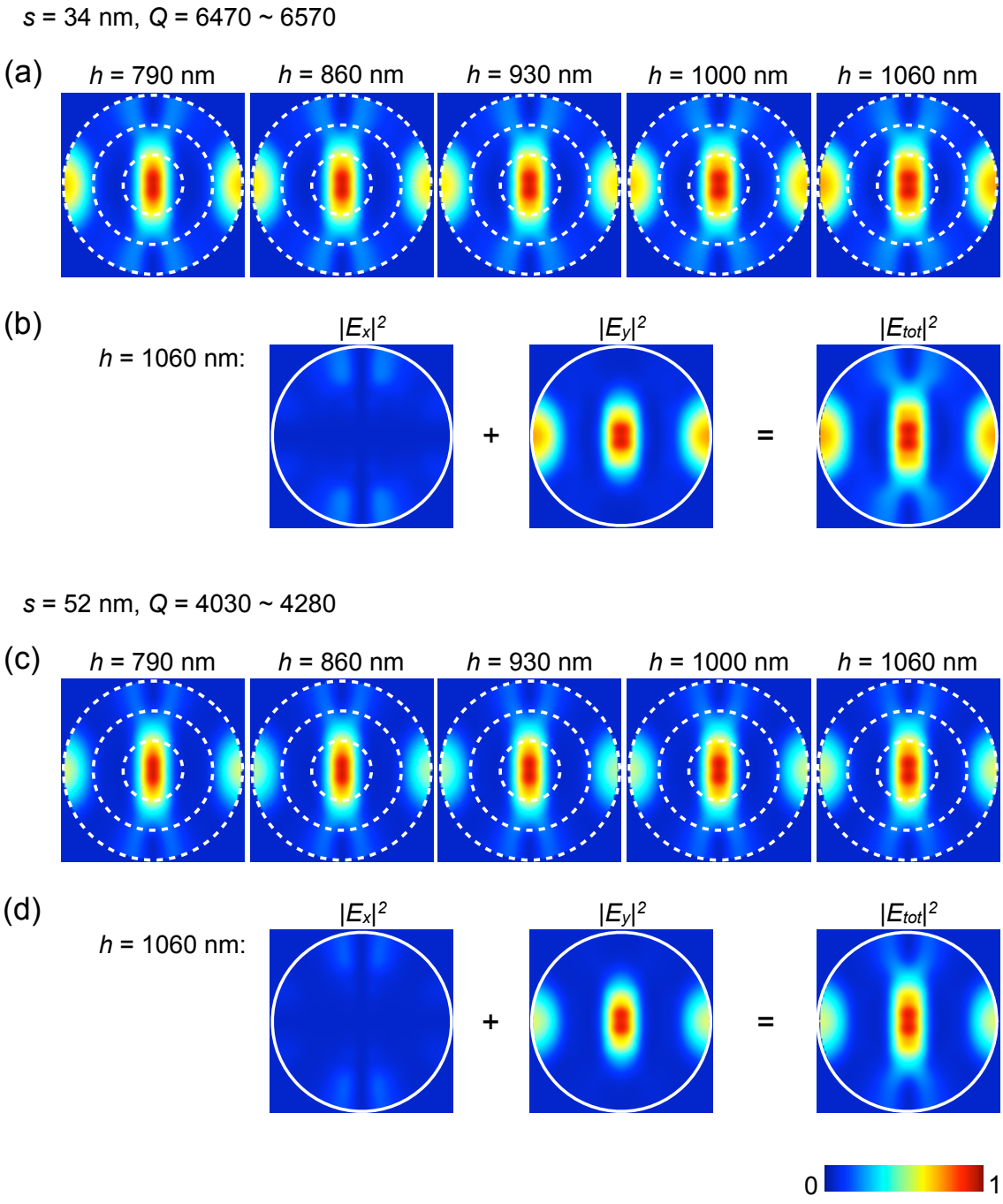

Figure 3.24: Effects of substrate on far-field radiation pattern from nanobeam photonic crystal lasers. (a) and (c) far-field pattern with different h; (b) and (d) linear polarization decomposition of far-field pattern when $h = 1060$ nm. (a) and (b) are for $s = 34$ nm, $Q = 6470 \sim 6570$. (c) and (d) are for $s = 52$ nm, $Q = 403 \sim 4280$. White dash lines indicate 30°, 60°, and 90° from surface normal, same as in Figure 3.20

Chapter 4

Device fabrication

The laser devices are made on epitaxially grown quantum well materials detailed in Table 4.1. The generalized sequence of device fabrication follows the standard planar lithography used in semiconductor device manufacturing, where we have two options for defining the etch mask—a photo- or electron-beam resist mask, or a hard mask such as SiO_x, SiON, or metal. Design of the fabrication process begins with the critical step of semiconductor dry etch using ion beam or plasma. The other process materials and parameters evolve from how well they work with the dry etch recipe at hand.

4.1 Dry etch indium III-V compound semiconductors

Compared with disk laser structures, which involve open-space etching with relaxed requirement on etch verticality [83, 114], photonic crystals have a particular intolerance for fabrication errors that deviate from the design [147, 148]. To etch III-V compounds involving indium, we can use either chlorine or iodine as the halogen reagent. The main by-product $InCl_3$ has a melting point of 586 °C and a boiling point of 800 °C [152, 153], resulting in a passivating layer on the surface, unless it is heated to increase volatility and evaporate off of the substrate during the etch[1]. An iodide etch chemistry forms In_xI_y as by-products, of which InI_3 has a melting point of 210 °C and a boiling point of 500 °C, InI has a melting point of 350 °C and a boiling point of 710 °C, and InI_2 a melting point of 225 °C [152, 154]. The In_xI_y by-products have enough volatility due to local heating during the etch, so that we can carry out the etch without the need for a heated substrate stage. We were

[1] InCl and $InCl_2$ have a lower melting point, at 225 °C and 262 °C, respectively [152].

Table 4.1: Epitaxial quantum well material designs

(a) InGaAsP quantum wells for 1.3 μm emission wavelength, slab thickness = 606 nm

Layer	Description	Thickness (Å)
8	$In_{0.85}Ga_{0.15}As_{0.32}P_{0.68}$ (1.12Q) lattice matched	2400
7	InGaAsP half-barrier (1.12Q), -0.3% tensile	60
6	Active region: PL emission peak at 1300 nm, InGaAsP well x7 (1.0% comp.) InGaAsP barrier 1.12Q x6 (-0.3% tens.)	Well: 60, barrier: 120
5	InGaAsP half-barrier (1.12Q), -0.3% tensile	60
4	$In_{0.85}Ga_{0.15}As_{0.32}P_{0.68}$ (1.12Q) lattice matched	2400
3	InP sacrificial	6500
2	InGaAs etch stop	1000
1	InP	3000
0	InP substrate	

(b) InAsP/InP quantum wells for 1.55 μm emission wavelength, slab thickness = 240 nm

Layer	Description	Thickness (Å)
6	InP cladding	600
5	InP half-barrier	200
4	Active region: PL emission peak at 1550 nm, InAsP well x4 InP barrier x3	Well: 50, barrier: 200
3	InP half-barrier	200
2	InP cladding	600
1	InGaAs sacrificial	11600
0	InP substrate	

able to implement these etch chemistries using either inductively-coupled plasma reactive ion etch (ICP-RIE) or chemically-assisted ion beam etch (CAIBE). The basic operations of both ICP-RIE and CAIBE are laid out in the following sub-sections, followed by details of our optimized etch recipes.

We developed three options to etch our indium-compound quantum well material: first, ICP-RIE without heated stage using $Ar/H_2/HI$ gas chemistry; second, ICP-RIE with heated stage using $CH_4/H_2/Cl_2$ gas chemistry; third, CAIBE with heated stage using Ar/Cl_2 chemistry. Most etch recipe calibration is in essence striking a balance between physical milling and chemical etching to optimize side wall verticality and etch rate, and a balance between semiconductor etch rate and mask erosion rate. However, we would like to add a word of caution for high temperature CAIBE. First, when Cl_2 flow is too high, the sample will undergo spontaneous chemical etch when at elevated temperatures of $135 \sim 160$ °C, even in the absence of any ion beam, as shown in Figure 4.1(a). Etch temperature can be as high as 190 °C to avoid solid In_xCl_y micromasking the device. The solution to curb spontaneous isotropic etch is to reduce the Cl_s flow rate. Second, when Cl_2 is introduced through small nozzles in the chamber, the gas may not diffuse evenly over the sample, resulting in non-uniform etch rates and profiles, shown in Figure 4.1(b). One can carefully center the sample below the Cl_2 nozzle, or use a ring-shaped *shower head* gas inlet to evenly distribute Cl_2 in the chamber.

After many etch calibrations and sad-looking samples, we arrived at the optimized recipes and results shown in Table 4.2 and Figure 4.2.

4.2 High-contrast etch mask

Next, an appropriate etch mask meeds to be developed to use with one of the etch recipes. Criteria for the etch mask include high etch resistance giving high etch rate contrast and vertical sidewalls to minimize signs of mask erosion on the resulting device. Figure 4.3(a) and (b) show problems with mask deformation due to local heating and etch artifact due to mask erosion, respectively. Photonic crystals' small air-holes pose an additional challenge. Gas species exchange is limited in small holes

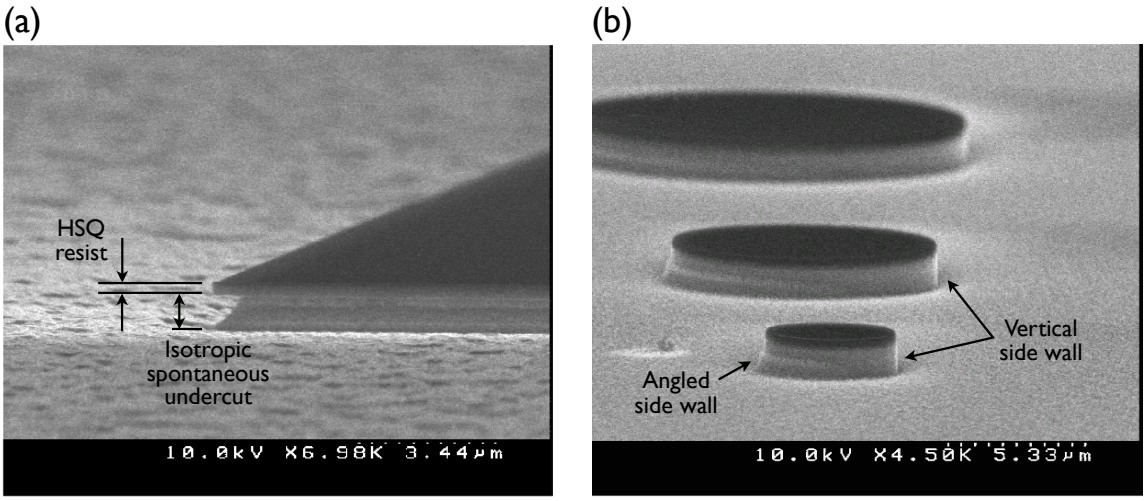

Figure 4.1: Potential problems in not well-calibrated CAIBE etch: (a) spontaneous isotropic etch when the sample is at 135 $\sim$ 160 ° in Cl_2 environment with no ion beam, Cl_2 exposure time is 10 min; (b) asymmetric etched side wall due to uneven Cl_2 flow.

Table 4.2: Calibrated etch recipes for III-V compounds with In, including InP, InGaAsP, InAsP, AlGaInP

(a) $Ar/H_2/HI$ ICP-RIE

Parameter	Value
Ar flow	3 sccm
H_2 flow	10 sccm
HI flow	30 sccm
Chamber pressure	10 mT
Forward power	90 W
ICP power	900 W
Stage temperature	Not controlled
He backing flow	0

(b) $CH_4/H_2/Cl_2$ ICP-RIE

Parameter	Value
CH_4 flow	8 sccm
H_2 flow	14 sccm
Cl_2 flow	18 sccm
Chamber pressure	4 mT
Forward power	180 W
ICP power	2200 W
Stage temperature	120 °C
He backing flow	10 Torr

(c) Ar/Cl_2 CAIBE

Parameter	Value
Ar flow	5 sccm
Cl_2 flow	1.4 sccm
Cathode	5.9 A / 6.0 V
Discharge	0.34 A / 40 V
Beam	30 mA / 750 V
Acceleration	2.6 mA / 100 V
Neutralization	22 mA
Stage temperature	190 °C

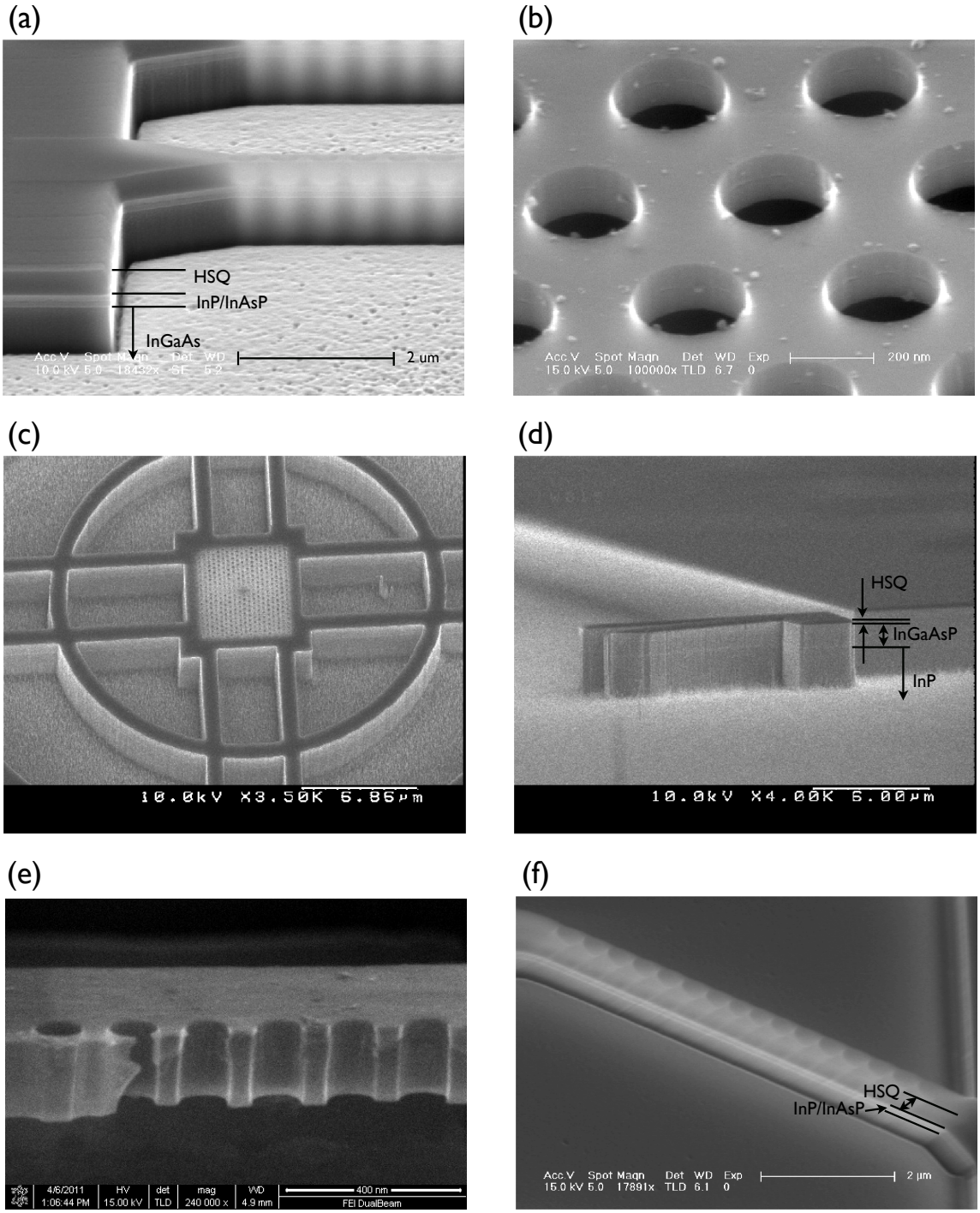

Figure 4.2: Etch results from optimized recipes: (a)–(b) InP with InAsP QWs etched using CAIBE; (c)–(d) InGaAsP etched using CAIBE; (e) AlGaInP etched using ICP-RIE with $Ar/H_2/HI$ chemistry; (f) InP etched using ICP-RIE with $CH_4/H_2/Cl_2$ chemistry.

in the substrate compared with large open areas, and so etch rate decreases as is evident in Figure 4.3(c).

The high ICP power or high etch temperature required in the dry etch makes polymer resists with a carbon backbone, such as the commonly used poly(methyl methacrylate) (PMMA) or even ZEP520[2], extra vulnerable to deformation and erosion. The absence of a good SiO_x or SiON etch recipe at the time dissuaded the use of dielectric hard masks. Metal masks tend to distort the local electromagnetic field and temperature profile, resulting in artifacts such as undercut and not-very-vertical side walls (Figure 4.4) that proved difficult to eliminate. Our best option came when we developed a high-contrast e-beam lithographic process on very thick hydrogen silsesquioxane (HSQ) resist—a high resolution negative tone resist that can be exposed using extreme ultraviolet (EUV) [155] or electron beam [156, 157, 158]. It consists of a network of Si-O-H polymer, whose monomer structure is shown in Figure 4.5(a) [159]. Upon exposure to electron beam and immersion in tetramethylammonium hydroxide (TMAH), the resist gives up H_2 and becomes an amorphous Si_xO_y; unexposed resist dissolves completely in TMAH. Exposed and developed HSQ has an etch resistance slightly lower than thermally grown or plasma-enhanced chemical vapor deposition (PECVD) grown SiO_2, but much higher than any carbon-based polymer. Moreover, our high-contrast lithography gives vertical side walls regardless of pattern feature size (Figure 4.5)

The etch resistance of HSQ mask depends on the amount of ion milling and plasma power in the etch. We found that high power plasma, predominant in ICP-RIE etches, is much more efficient at resist thinning than high power ion milling that is predominant in CAIBE. Moreover, ICP-RIE etch rate appears to decrease much more rapidly with decreasing air-hole size, thus reducing etch selectivity in small device features.

4.3 Wet-etch of the sacrificial layer

Following the dry etch, a wet-etch is needed to remove the sacrificial InP or InGaAs layer. To remove InP from 1.12Q and 1.3Q InGaAsP, we use 4:1 HCl:H_2O at 4 °C [160]. To remove InGaAs from

[2]A high etch resistant e-beam resist manufactured by Zeon Corporation, Tokyo, Japan

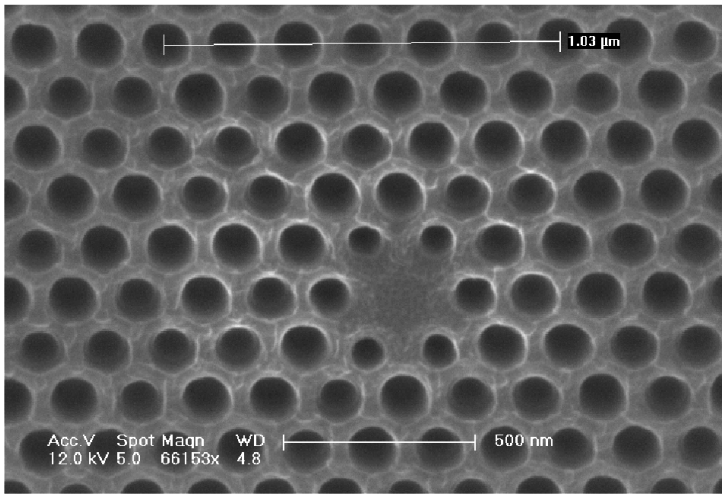

(a)

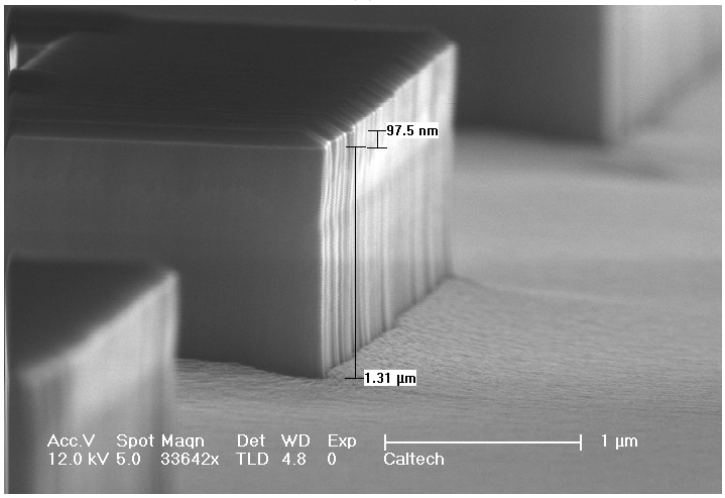

(b)

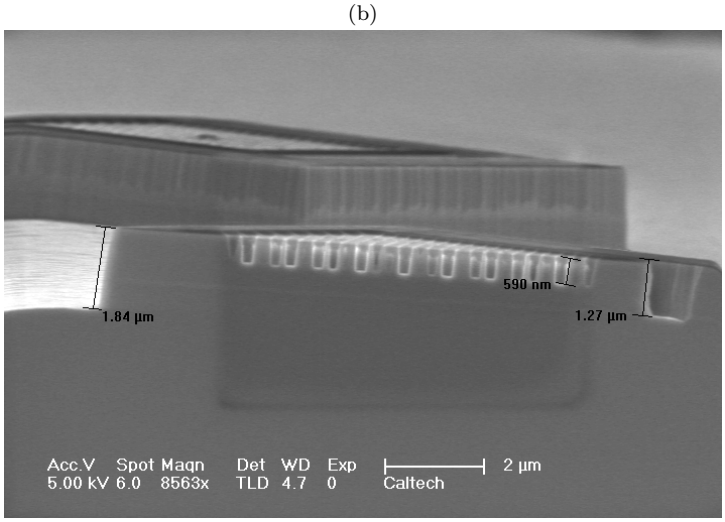

(c)

Figure 4.3: Common dry etch problems encountered in etching photonic crystals in In-based III-V compound: (a) air-hole non-uniformity due to PMMA mask deformation during etch; (b) rough side wall due to mask erosion; (c) non-uniform etch rate due to device feature size.

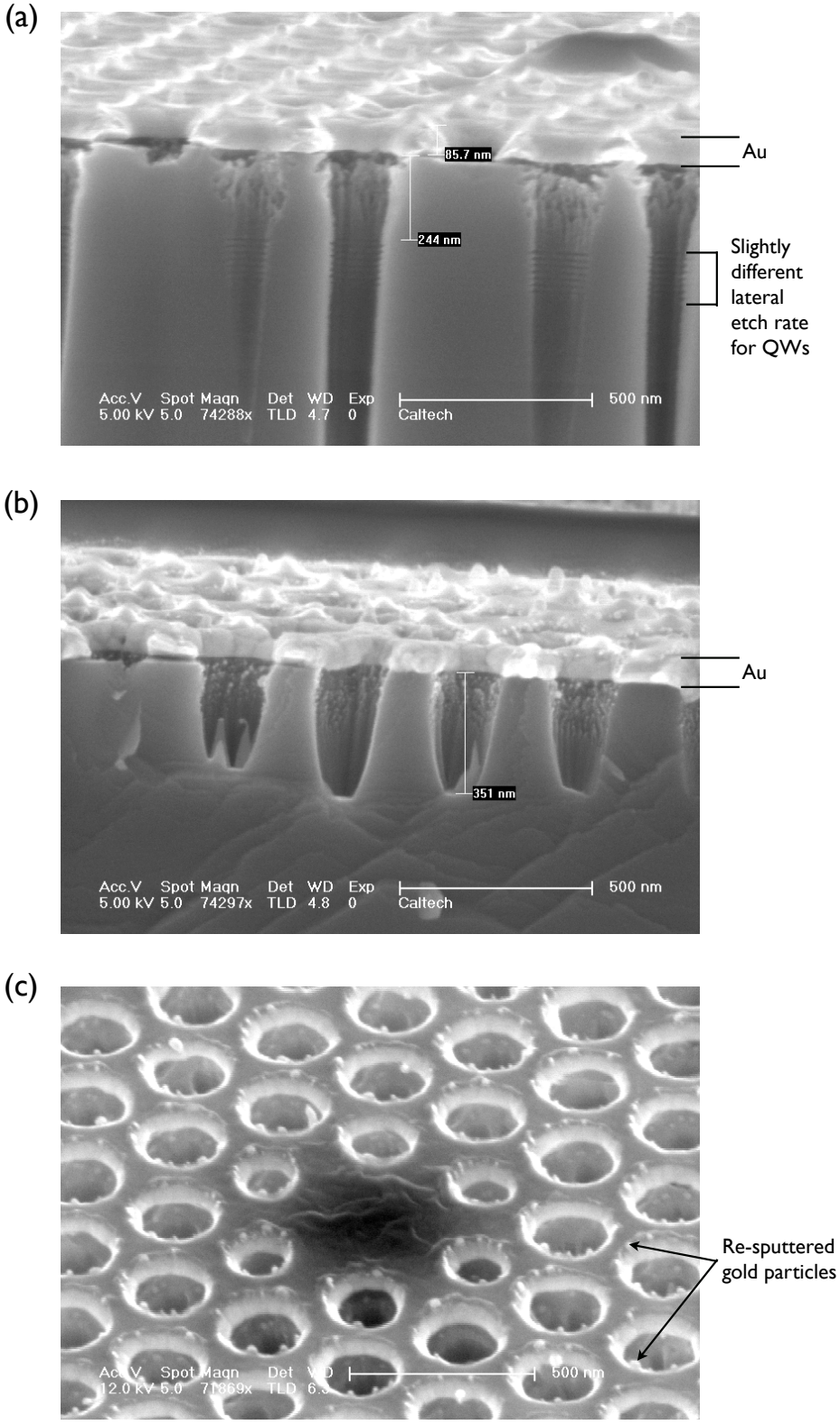

Figure 4.4: Etch deformation due to the presence of a metal mask: (a) local undercut and micro-masking due to mask re-sputtering in CAIBE; (b) etch profile change due to metal mask in ICP-RIE; (c) metal re-sputtering in ICP-RIE, the wrinkled top layer is PMMA resist, bright mid-layer is Au. The substrate is 600 nm InGaAsP on InP.

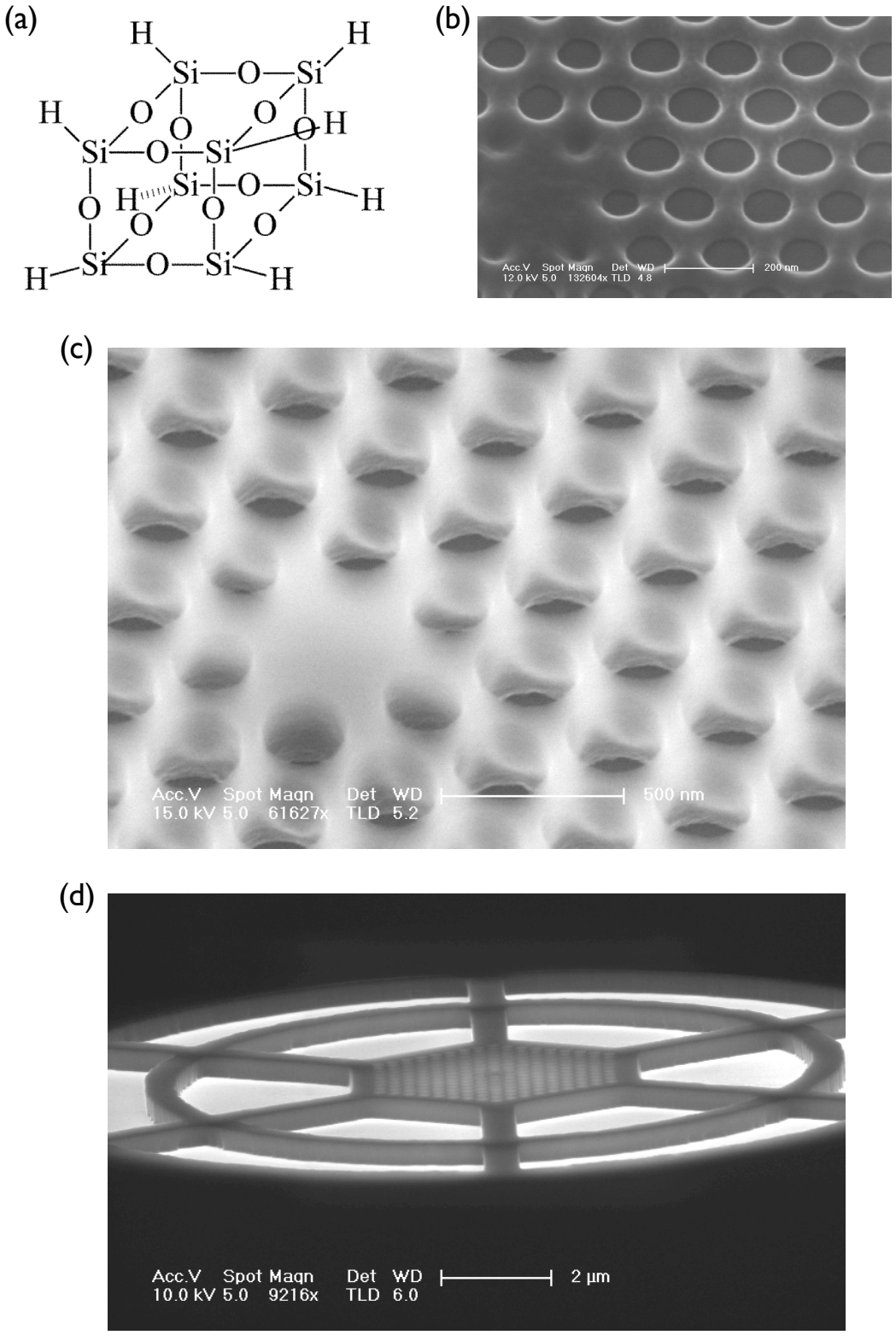

Figure 4.5: HSQ resist: (a) molecular structure; (b) SEM images of developed resist after low contrast electron-beam lithography; (c)–(d) SEM image of a developed resist with vertical side walls to enhance etch quality of the underlying III-V semiconductor.

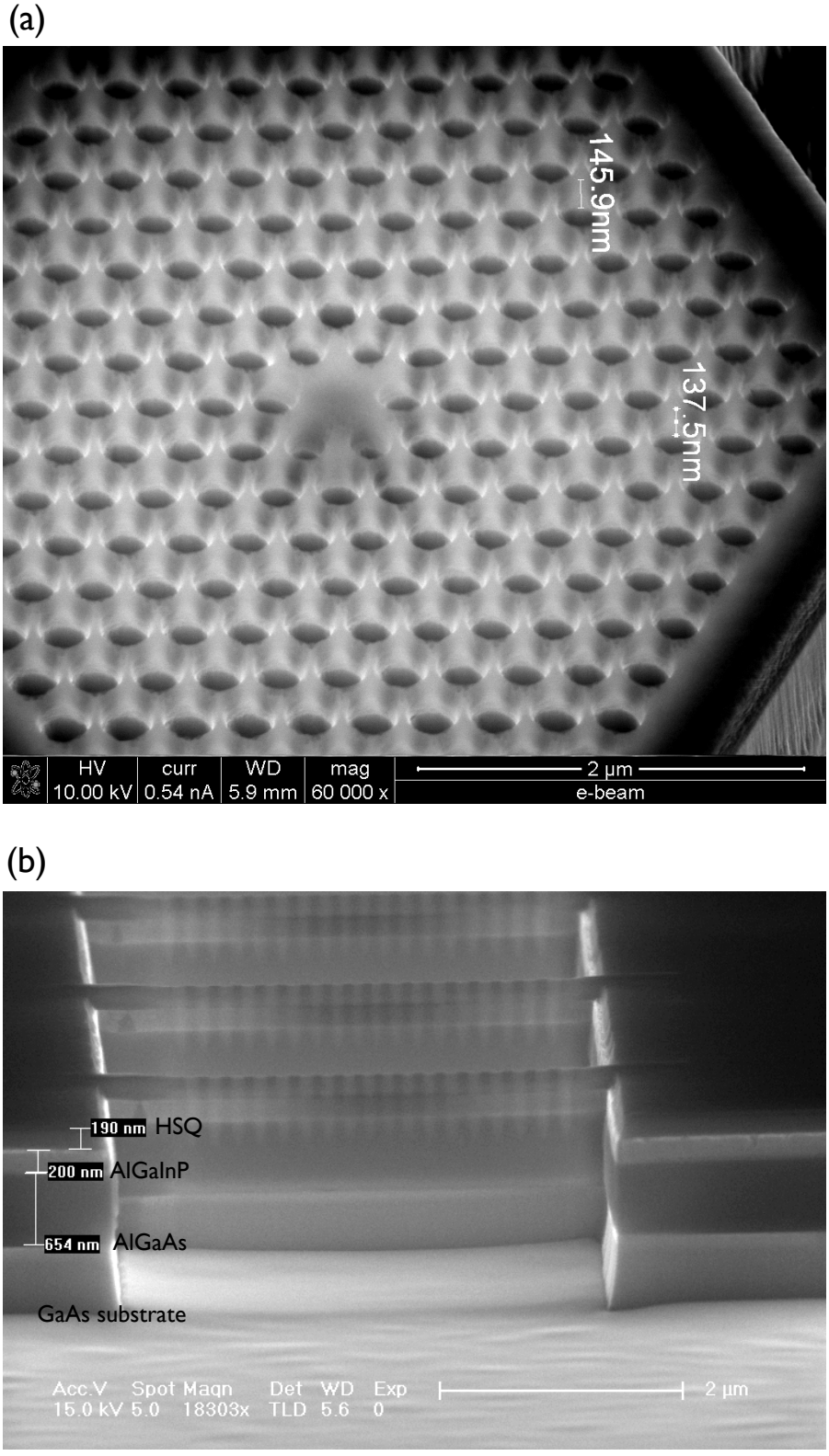

Figure 4.6: SEM images of HSQ mask after dry etch: (a) 140 nm of HSQ resist remains after CAIBE; (b) 190 nm of resist remains after $Ar/H_2/HI$ ICP-RIE.

InP and InGaAsP, we developed a version of the H_2CrO_4:HF etchant mentioned in [161], diluted in H_2O and used at room temperature. Its etch rate depends on the dilution and whether the solution is freshly made. Regardless of etch rate, however, the wet-etch selectivity against 1.12Q InGaAsP is about 30:1, 40:1 against 1.3Q InGaAsP. Selectivity of InGaAs against InAsP and InP is near infinite; by that we mean that in undiluted H_2CrO_4:HF, we were able to undercut into >30 μm of InGaAs when the epitaxial layer is only 100 nm thick, all the while with no visible damage to InP/InAsP. SEM image from H_2CrO_4:HF:H_2O etch rate and selectivity test are shown Figure 4.7.

4.4 Complete device fabrication procedure

After developing and optimizing each step of the fabrication procedure, our final process is summarized here. Finished devices are shown in Figures 4.8–4.10.

4.4.1 E-beam lithography

- Beam voltage: 100 kV
- Resist: FOx-16 from Dow Corning
- Spin at 4000 RPM for 375 nm resist thickness
- Bake at 170 °C for 2 min
- Expose at $250 \sim 700$ μC/cm^2, depending on substrate material and feature size
- Develop in AZ 300MIF at 70 °C for 4 min, rinse in H_2O, N_2 blow dry

4.4.2 Dry etch

- Use recipes in Table 4.2
- For deep etch, use CAIBE: InP/InAsP/InGaAsP etch rate is 1.8 μm/min, HSQ resist erosion rate is 80 nm/min
- For III-V slab thickness of $\leq$250 nm, ICP-RIE can be used without resist erosion artifact

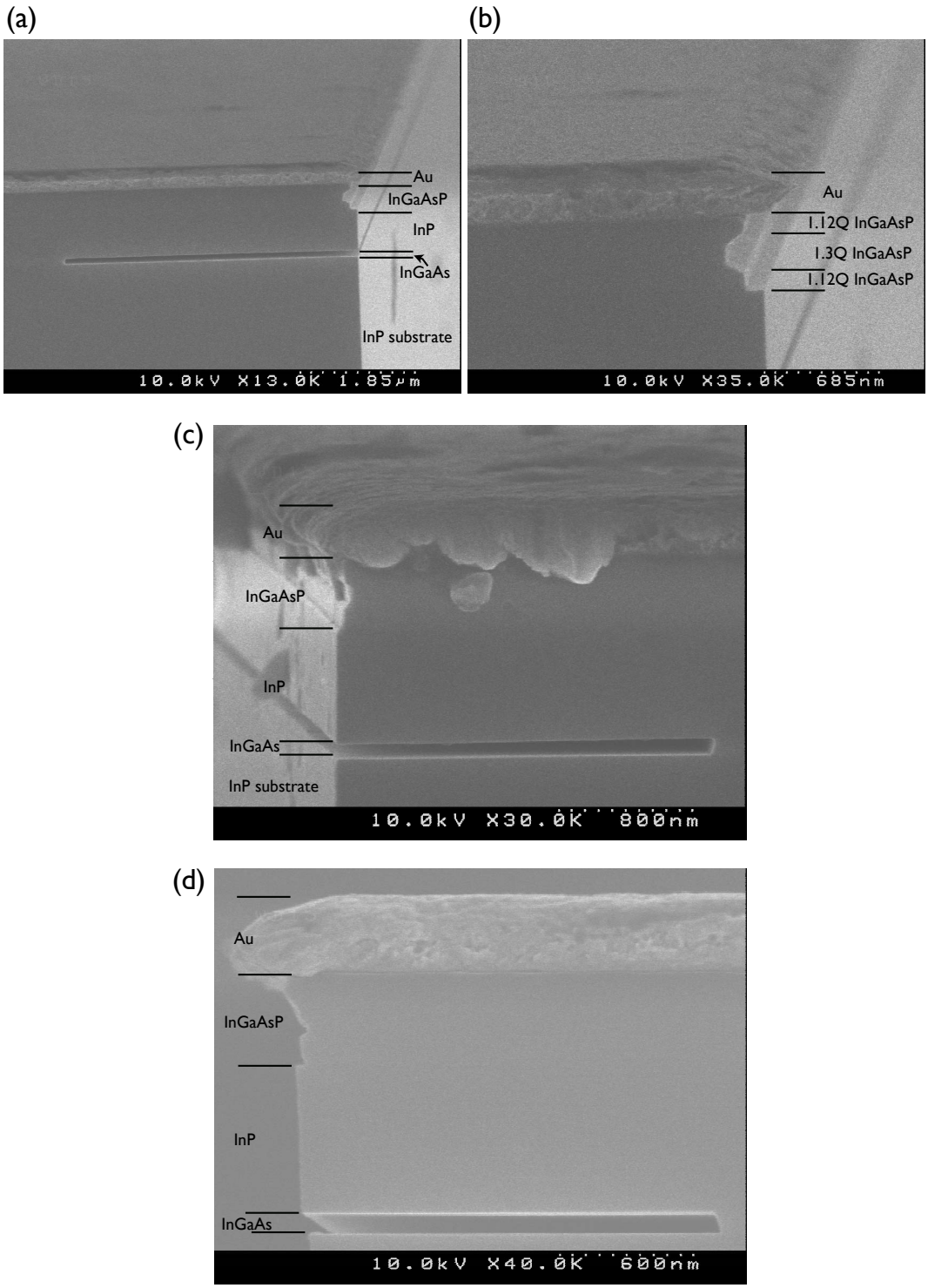

Figure 4.7: H_2CrO_4:HF:H_2O etched InGaAs against remaining InGaAsP and InP. The material layers are, from top, gold, 1.12Q InGaAsP, 1.3Q InGaAsP, 1.12Q InGaAsP, InP, InGaAs, and InP substrate. (a) Solution ratio is 1:1:40, etched at 4 °C for 5 seconds. Etch depth for InGaAs, 1.3Q InGaAsP, and 1.12Q InGaAsP are 4.7 μm, 225 nm, and 90 nm. (b) Solution ratio is 1:1:460, etched at room temperature for 10 seconds. InGaAs etch depth is 2.25 μm. (c) Same solution as (b), etched at 4 °C for 10 sec. InGaAs etch depth is 1.84 μm, compared with 40 nm for 1.3Q InGaAsP and 60 nm for 1.12Q InGaAsP.

4.4.3 H_2CrO_4:HF:H_2O wet-etch

- Dissolve 10 g CrO_3 in 100 g H_2O
- Mix H_2CrO_4 solution, 48% HF, and H_2O with ratio 1:1:460
- At 4 °C, InGaAs to 1.12Q InGaAsP selectivity is 30:1, InGaAs to 1.3Q InGaAsP selectivity is 40:1, InGaAs to InP selectivity is >5000:1.

4.4.4 Drying after wet-etch

- For 2D photonic crystal, rinse in H_2O, N_2 blow dry
- For nanobeam photonic crystal, rinse in filtered IPA, critical-point drying required

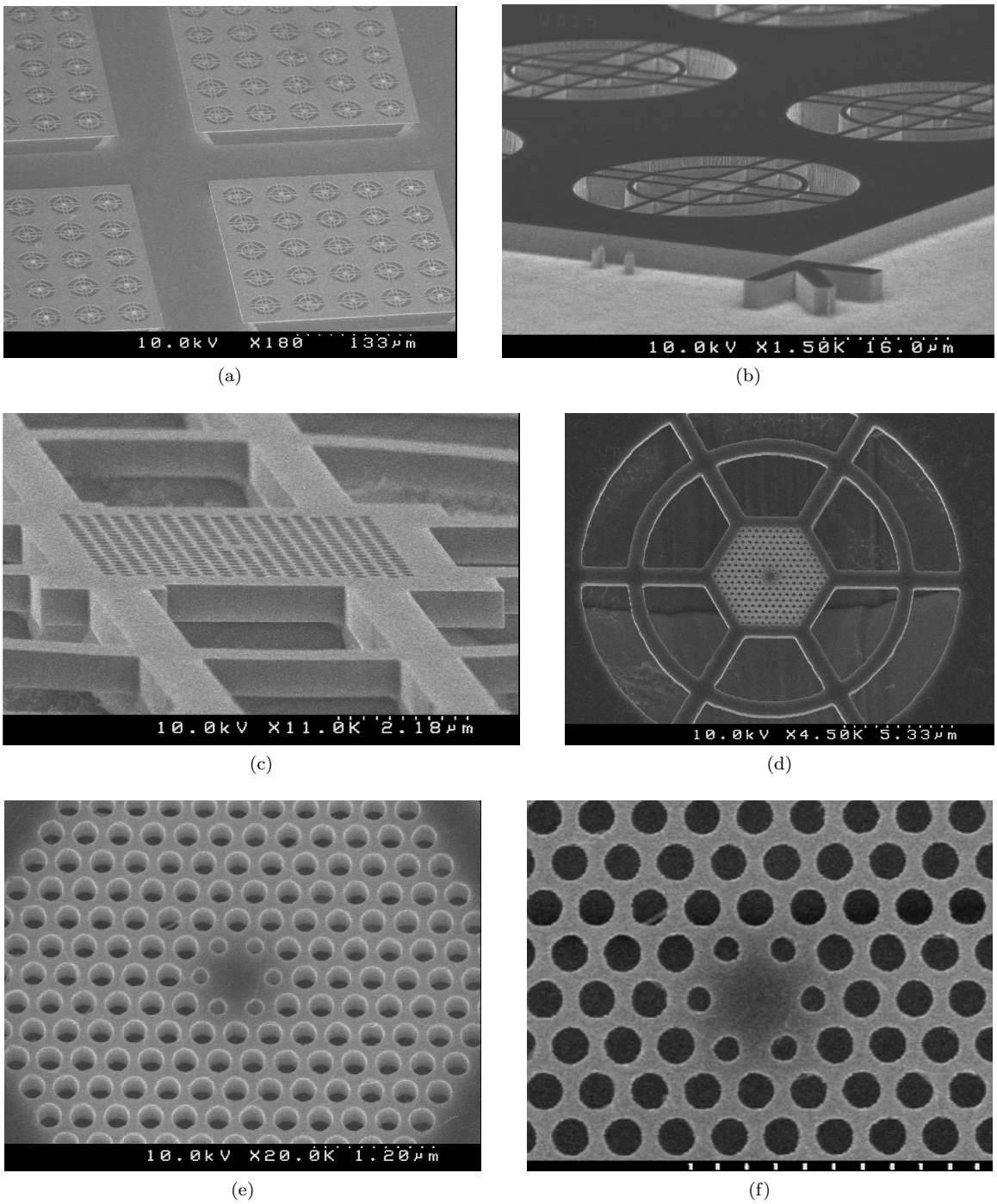

Figure 4.8: SEM images of finished thick-slab microlasers, active material is 1.3Q InGaAsP quantum wells in 1.12Q InGaAsP cladding, in order of progressive zoom-in: (a) arrays of thick-slab lasers ready for testing; (b) after CAIBE etch before wet etch, etch depth is 3 μm; (c) glancing angle view of a finished device, slab thickness is 606 nm; (d) top view of an undercut device; (e) a tilted view of the air-holes, showing straight CAIBE etched sidewalls and very little damage from wet etch; (f) top view close of the cavity region, air-hole periodicity is 305 nm.

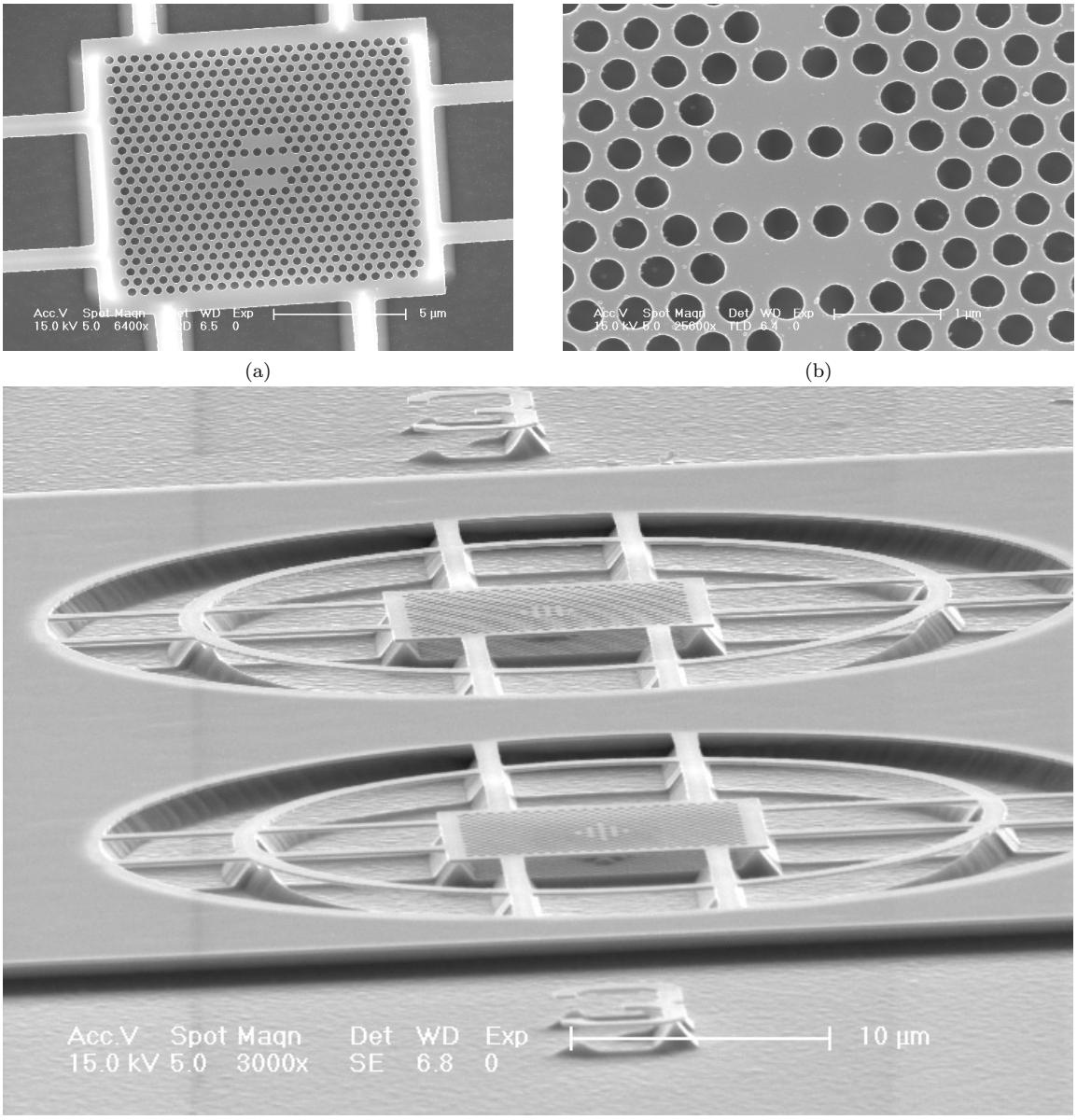

(a) (b)

(c)

Figure 4.9: SEM images of finished coupled-cavity microlasers, active material is InAsP quantum wells in InP cladding.

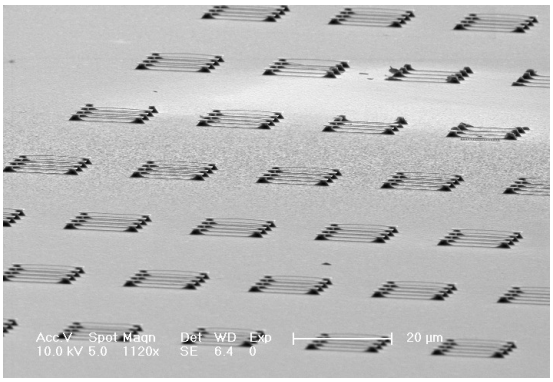

(a)

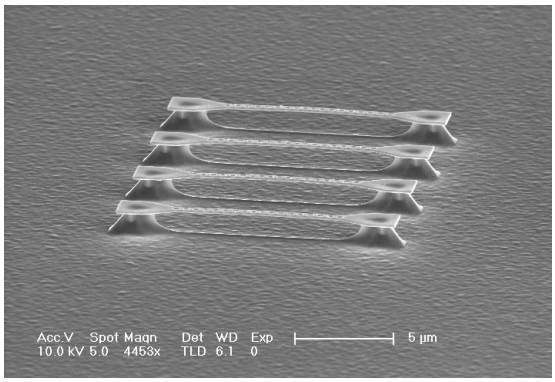

(b)

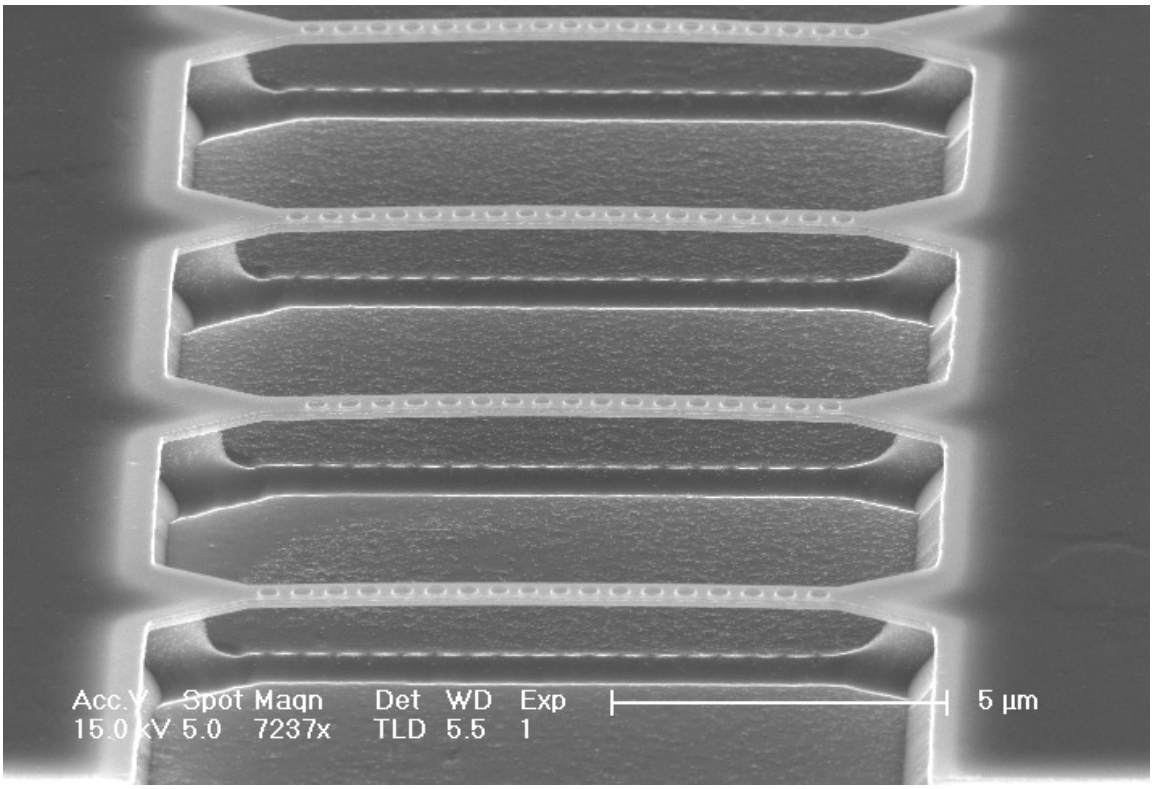

(c)

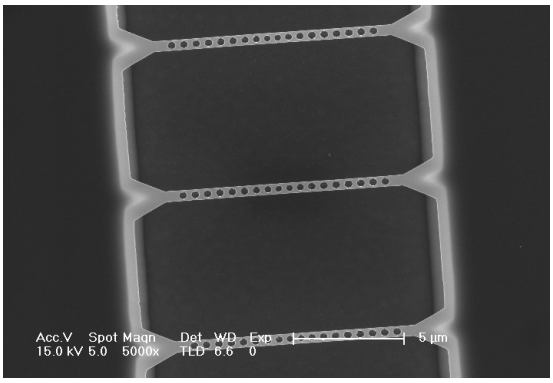

(d)

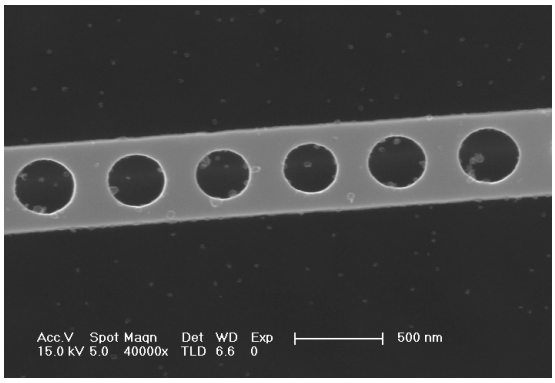

(e)

Figure 4.10: SEM images of finished nanobeam photonic crystal microlasers, active material is InAsP quantum wells in InP cladding.

Chapter 5

Microlaser characterization

5.1 Photoluminescence measurement

In the absence of an electrical current path through the laser cavity, such as a p-i-n doping profile to allow current injection to the QW or QD layers [17, 162, 163], optical pumping is used to excite the laser cavity. A light source with shorter emission wavelength than that of the gain material generates electron-hole pairs that recombine to give off spontaneous emission or coherent light when lasing is achieved in the microcavity. By analyzing the optical pump power absorbed and the power, spectrum, mode pattern, and polarization of light emitted by the cavity, we can evaluate our numerical simulation and theoretical prediction, and parse out details of the microlaser's characteristics.

In the measurement, the sample is mounted on an xyz stage. A 830 nm pump laser light is collimated, then focused through a long working distance 50$\times$ microscope objective to a 4-μm diameter spot on the sample at an angle normal to the surface. The pump laser is actuated by a function generator, which tunes the pump light duty cycle from 1% to 100% CW. A small percentage of it is split off by a low reflection beam splitter to a broad area Si photodetector for measuring pump laser power at the particular operating voltage and duty cycle. Emitted light from the sample is collected by the same objective lens, re-directed by the 50-50 beam splitter to a lower power objective, which focuses the signal into a multimode optical fiber connected to an optical spectrum analyzer (OSA). A collimated white light, a flip mirror, and a CCD camera are integrated into the measurement set-up for visual alignment of the pump spot and the microcavity devices. A long pass

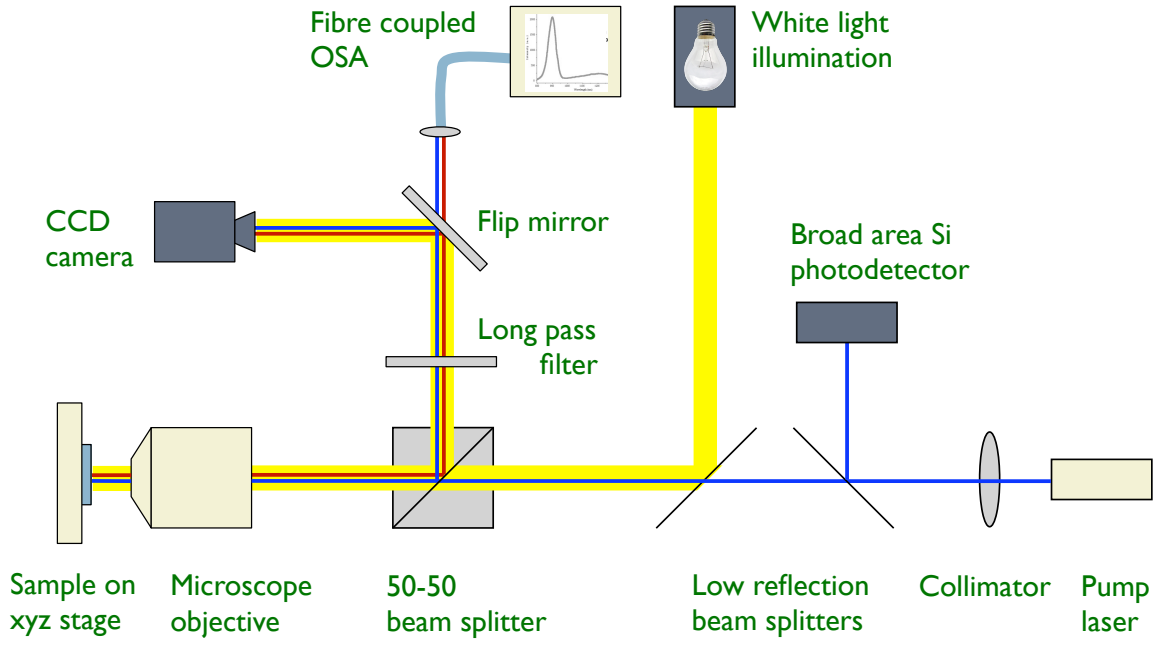

Figure 5.1: Photoluminescence measurement set-up used to characterize microlasers. Blue lines indicate pump laser path, red lines indicate path of light emitted from the microlaser device. Thick yellow line is the path of the while light illumination.

filter with a cut-off wavelength of 1150 nm is placed in the beam path after the 50-50 beam splitter to block most of the 830 nm pump light from the CCD camera and the OSA. The microlasers studied in this work emit at $\lambda = 1.3$ or 1.55 μm. A schematic of the photoluminescence measurement set-up is shown in Figure 5.1.

5.2 Signatures of a laser

When we scan the sample by passing the pump laser spot over the arrays of microcavities, it is not difficult to distinguish lasing devices from the non-lasing ones. On the CCD camera, incoherent light from non-lasing devices appears as a diffuse spot, while coherent light is much brighter and shows distinct fringe patterns that result from the interference of a monochromatic light. In fact, for devices operating at its longest lasing duty cycle, we see its emitted light turn to a diffuse spot when duty cycle is increased and return to a fringed pattern when duty cycle is turned down again. The

fringe pattern mentioned above is itself a manifestation of coherence [26]. In spectral measurement, it is characterized by sharp peaks with narrow linewidths—<100 pm in CW lasers and can be a few nm in pulsed operation when widened by thermally induced wavelength chirping [86]—and peak intensity much above the background noise.

Then, the device's output power as a function of the input pump power is recorded. The result is a light-in versus light-out (L-L) curve. Most lasing devices so far experimentally realized still have a moderate $F_p\beta$ value, such that the L-L curve has a discernible threshold, beyond which output power increases linearly with much higher differential efficiency dL_{out}/dL_{in} than below threshold. More than an evidence of lasing action, the L-L curves can be fitted to the laser rate equations to extract more quantitative data about the device, especially β and N_{tr}. We will delve into the details of rate equation analysis in Section 5.3.

When the devices achieve CW lasing, linewidth narrowing as pump power increases is another signature of lasing. Turning up the pump power from zero, the below-threshold linewidth narrows as described by the Schawlow-Townes linewidth formula. When the pump power reaches the threshold region, linewidth broadens slightly with increasing power due to gain-refractive index coupling. Then as pump power rises beyond the threshold, laser linewidth narrows again, given by $\left(1+\alpha^2\right)/2$ times the non-modified Schawlow-Townes formula, where α here is the linewidth enhancement factor [164]. The threshold region thus represents a kink in the decreasing trend of linewidth as a function of power. Linewidth measurements are not quite applicable when the devices operate in pulsed mode; thermal chirping brings overwhelming phase noise and results in linewidth widening with increasing pump power [86].

Lastly, a direct proof of lasing action is given by coherence measurement of photon correlation functions [165, 166]. The second order function

$$g^{(2)}(\tau=0)=\frac{\langle I\left(t\right)I\left(t+\tau\right)\rangle}{\langle I(t)\rangle\langle I(t)\rangle} \tag{5.1}$$

as a function of pump power L_{in}, where $\langle I(t)\rangle$ is the expectation value of intensity at time t, has

been experimentally implemented [124, 167]. Second order photon correlation measurements were not performed in this work. However, it becomes increasingly important in proving above-threshold lasing and determining threshold pump power as the research field gets closer to demonstrating high $F_p\beta$ laser with *thresholdless*-like L-L behavior.

In the subsequent sections where we present results from device characterization, we pay particular attention to several metrics to quantify the quality of our microcavity lasers: (1) room temperature CW operation, (2) threshold pump power, (3) far-field emission directionality, (4) thermal resistance manifested by the emission wavelength as a function of input power, and (5) comparative differential quantum efficiency measured by the slope of L-L curve above threshold. The devices' sensitivity to feedback from surrounding structures is also a characteristics of concern; however, this is so far addressed in design by numerical simulation only in Chapter 3.

5.3 Rate equation analysis

Microlasers with wavelength-scale optical confinement have only recently began to demonstrate reliable room temperature CW operation with adequate output power [86, 19, 168, 169]. Therefore, L-L curves showing threshold transition and rate equation analysis have been the primary method to demonstrate a lasing device. In their book, Coldren and Corzine used the *reservoir picture* to illustrate the derivation of laser rate equations [71]. The analogy is in essence a conservation of energy picture. We have modified it to include Purcell enhancement F_p and spontaneous emission coupling factor β. Our rate equations are derived from keeping count of carriers and photons as shown in Figure 5.2. The lasing process begins with carrier injection into the device with a rate of I/e for electrical pumping or $L_{in}/\hbar\omega_p$ for optical pumping, where I is the injected current and e is the elementary charge. Only a fraction of the carriers $\eta_i(I/e)$ reach the active region that has a volume V_a, where η_i is the device's internal efficiency. While current injection adds to carrier number in V_a, the processes of non-radiative recombination, stimulated emission, and spontaneous emission deplete it. Stimulated emission and a portion β of spontaneous recombination events contribute to photon count in the lasing mode, thus β is called the spontaneous emission coupling efficiency.

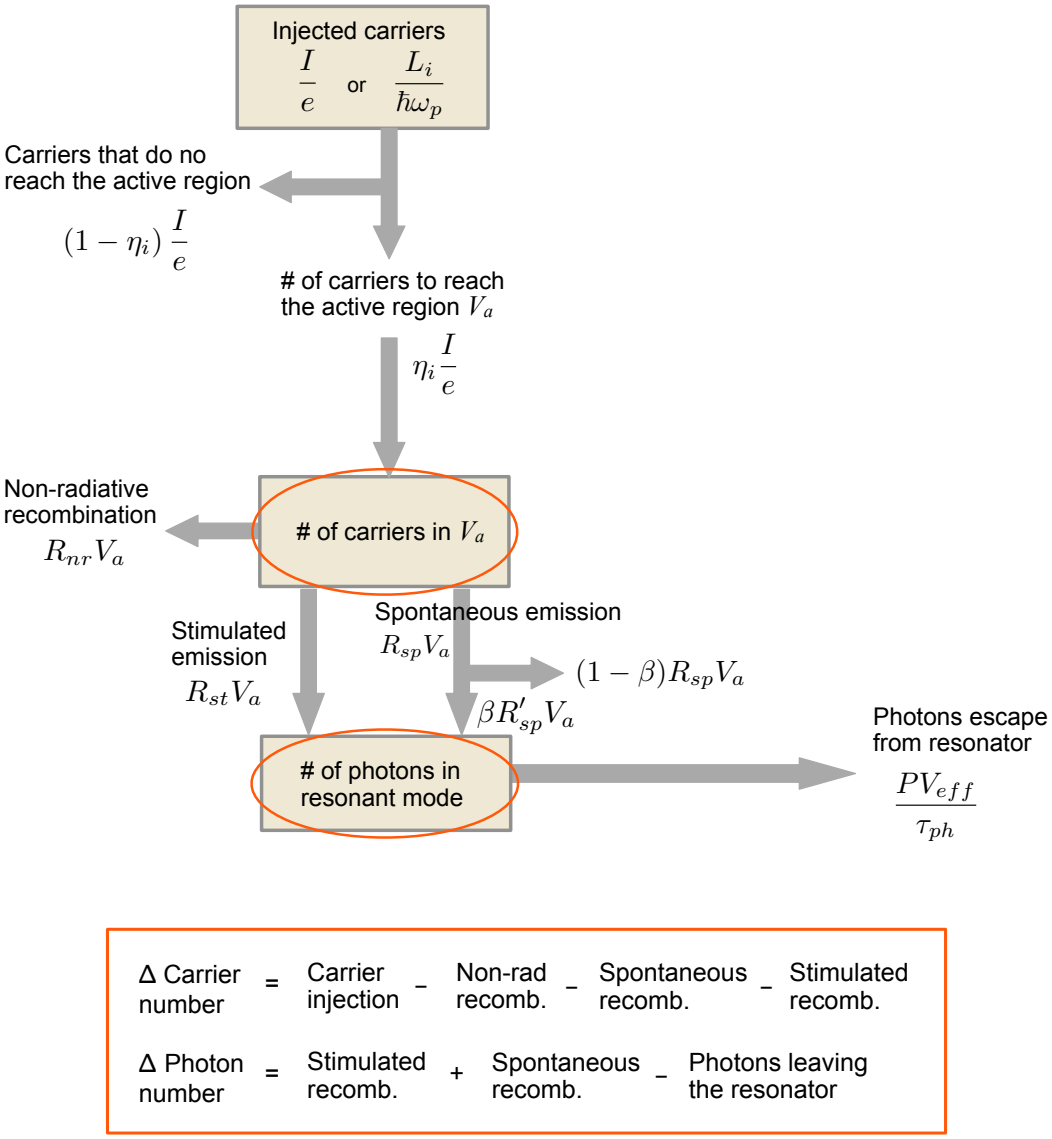

Figure 5.2: Conservation of energy picture to derive the laser rate equations.

Finally, photons radiate from the device with a rate dictated by the photon lifetime in the cavity $\tau_{ph} = Q/\omega_l$, where ω_l is the frequency of the lasing mode. From this picture, we can count the change in carrier numbers in the active region $d\hat{N}/dt$ and the change in photon numbers in the lasing mode $d\hat{P}/dt$ at the nodes circled in Figure 5.2.

$$\begin{array}{lcl} \text{Change in} \\ \text{carrier number} \end{array} = \begin{array}{l} \text{Carrier} \\ \text{injection} \end{array} - \begin{array}{l} \text{Non-radiative} \\ \text{recombination} \end{array} - \begin{array}{l} \text{Spontaneous} \\ \text{recombination} \end{array} - \begin{array}{l} \text{Stimulated} \\ \text{recombination} \end{array} \tag{5.2}$$

$$\begin{array}{lcl} \text{Change in} \\ \text{photon number} \end{array} = \begin{array}{l} \text{Stimulated} \\ \text{recombination} \end{array} + \begin{array}{l} \text{Spontaneous} \\ \text{recombination} \end{array} - \begin{array}{l} \text{Photons leaving} \\ \text{the resonator} \end{array} \tag{5.3}$$

In optically pumped devices, carriers are excited by the material's absorption of the pump laser light. The expression for current injection rate is thus $L_{in}/\hbar\omega_p$ instead of I/e. L_{in} is the input optical power, ω_p is the frequency of the pump laser. Thus the rate equations take the form

$$\frac{d\hat{N}}{dt} = \frac{\eta_i L_{in}}{\hbar\omega_p} - \hat{R}_{sp} - \hat{R}_{nr} - \hat{R}_{st} \tag{5.4}$$

$$\frac{d\hat{P}}{dt} = \hat{R}_{st} - \frac{\hat{P}}{\tau_{ph}} + \hat{R}'_{sp} \tag{5.5}$$

Caret indicates total number quantities that are not normalized by volume. However, the recombination rates that one would measure experimentally as metrics should be normalized by device volume. Therefore, we rewrite the above *number* rate equations into *density* rate equations by substituting $number = density \times volume$.

$$V_a \frac{dN}{dt} = \frac{\eta_i L_{in}}{\hbar\omega_p} - R_{sp}V_a - R_{nr}V_a - R_{st}V_a \tag{5.6}$$

$$V_{eff} \frac{dP}{dt} = R_{st}V_a - \frac{PV_{eff}}{\tau_{ph}} + R'_{sp}V_a \tag{5.7}$$

Note that carriers and photons contributing to the lasing mode occupy different spatial volumes; the former are confined in the active region V_a, while the latter density is normalized by the effective

mode volume V_{eff}. Rewrite the equations using the confinement factor $\Gamma = V_a/V_{eff}$, we have

$$\frac{dN}{dt} = \frac{\eta_i L_{in}}{\hbar\omega_p V_a} - R_{sp} - R_{nr} - R_{st} \tag{5.8}$$

$$\frac{dP}{dt} = \Gamma R_{st} - \frac{P}{\tau_{ph}} + \Gamma R'_{sp} \tag{5.9}$$

Spontaneous emission rate is usually modeled as $R_{sp} = N/\tau_{sp}$ in conventional semiconductor lasers, where τ_{sp} is the measurable quantity, spontaneous emission lifetime.[1] We want to distinguish it from R'_{sp} the spontaneous emission rate coupled to the lasing mode and enhanced by Purcell effect when cavity conditions are right. Thus,

$$R_{sp} = (N/\tau_{sp})\,(1 - \beta + F_p\beta) \tag{5.10}$$

$$R'_{sp} = F_p\beta N/\tau_{sp} \tag{5.11}$$

Stimulated emission is related to the optical gain of the material g. More precisely, we define g as the proportional growth of photon density as it propagates in the cavity, in mathematical form, it is

$$g = \frac{1}{P}\frac{dP}{dz} = \frac{1}{P}\frac{dP}{dt}\frac{dt}{dz} = \frac{1}{v_g}\frac{dP}{dt} = \frac{R_{st}}{v_g P} \tag{5.12}$$

where v_g is the group velocity of the optical mode. $g(N)$ can be calculated using theory of optical gain in semiconductors [170] or measured experimentally; the two methods can agree quite well [171, 172]. Although we have a good theoretical model, it is an over-complication to use it for the rate equation. If we focus our attention to when $g \geq 0$, as is the case for rate equation analysis, $g(N)$ curves can be accurately fitted to a simple logarithmic formula [71]

$$g(N) = g_0 \ln\frac{N}{N_{tr}} \tag{5.13}$$

[1] R_{sp} is also known to be modeled as BN^2, where B is the bimolecular recombination coefficient. B characterizes conduction band to valence band recombination, thus it depends on both electron and hole densities $R_{sp} = BN_{e^-}N_{h^+}$. Since the laser active region is charge neutral, $N_{e^-}N_{h^+} = N^2$. In building high $F_p\beta$ microlasers, we are particularly concerned with the spontaneous emission lifetime; moreover, it is a readily measurable quantity. Therefore, we chose to model R_{sp} using N/τ_{sp}.

where g_0 is an empirical gain coefficient and N_{tr} is the transparency carrier density, i.e. the minimum carrier density at which $g > 0$.

Non-radiative recombination counts its main contribution from surface recombination and Auger recombination, $R_{nr} = R_{sr} + R_{Auger}$. Surface recombination can have considerable effects on nanodevices, particularly pronounced in e.g. GaAs/AlGaAs transistors and lasers, for which surface passivation techniques have been developed with dramatic performance improvement [173, 174, 175]. The problem is exacerbated by the high surface to volume ratio in microlaser cavities, especially in photonic crystals [71, 176, 177]. Surface recombination arises when dangling bonds at the termination of the crystal lattice form a miniband in the bandgap, causing carrier recombinations similar to those caused by mid-gap energy levels caused by dopants. A simple but intuitive picture of surface recombination rate begins with the results of the Shockley-Read-Hall theory, which describes defect or impurity induced recombination[2] [71, 178, 179]

$$R_d = \frac{N_{e^-} N_{h^+} - N_i^2}{N_{e^-} \tau_h + N_{h^+} \tau_e} \tag{5.14}$$

where N_{e^-} and N_{h^+} distinguish the electron and hole densities, N_i is the intrinsic carrier density, τ_e is the time required to capture an electron from the conduction band assuming empty defect traps, similarly τ_h is the hole capture time. Unlike other trap-assisted recombination, which are distributed throughout the material, surface recombination capture rate is defined as carriers within a *capture length* l_c from the surface with a capture lifetime τ_c, that is, *capture velocity* $= l_c/\tau_c$. Using this concept, rewrite Equation (5.14) with capture velocity using $v_{sr,e} = l_c/\tau_e$ and $v_{sr,h} = l_c/\tau_h$, and make sure that R_sr is still normalized by volume, we have

$$\begin{aligned} R_{sr} &= \left(\frac{a_s l_c}{V_a}\right)\left(\frac{N_{e^-} N_{h^+} - N_i^2}{N_{e^-} l_c/v_{sr,h} + N_{h^+} l_c/v_{sr,e}}\right) \\ &= \left(\frac{a_s}{V_a}\right)\left(\frac{N_{e^-} N_{h^+} - N_i^2}{N_{e^-}/v_{sr,h} + N_{h^+}/v_{sr,e}}\right) \end{aligned} \tag{5.15}$$

where a_s is the surface area. In the charge-neutral laser cavity, $N_{e^-} = N_{h^+} = N$. At high current

[2]This equation is a simplified version by assuming deep-level traps, that is, the surface state induced miniband is near the middle of the bandgap.

injection levels in which a laser operates, $N \gg N_i$. Apply these conditions, we have our final express for R_{sr},

$$\begin{aligned} R_{sr} &= \left(\frac{a_s}{V_a}\right)\left(\frac{v_{sr,h}v_{sr,e}}{v_{sr,h}+v_{sr,e}}\right)N \\ &= \frac{a_s}{V_a}v_{sr}N \\ &= AN \end{aligned} \tag{5.16}$$

where v_{sr} is the surface recombination velocity, and A is the surface recombination coefficient.

While surface recombination garners much attention in the microlaser research community, Auger recombination should not be ignored; it has comparable or higher contribution to non-radiative events when carrier density is high $> 10^{18}$ cm^{-3}, a level easily reached in lasers [180]. The process involves the collision of two electrons/holes in the conduction/HH band, knocking one electron/hole to the valence/conduction band while sending the other deeper into the conduction/valence (LH or SO) band, which then thermalizes back to the edge of the conduction/valence band. The complexity of this process means that accurate theoretical modeling is challenging; it is indeed still a work in progress. A common method of estimating the extend of Auger recombination uses experimentally obtained Auger recombination coefficients in the form [71]

$$R_{Auger} = C_n N_{e^-}^2 N_{h^+} + C_p N_{e^-} N_{h^+}^2 \tag{5.17}$$

In lightly doped laser active regions, $N_{e^-} = N_{h^+} = N$,

$$R_{Auger} = CN^3 \tag{5.18}$$

where C is the Auger recombination coefficient.

Now that we have addressed all of the recombination processes, we substitute them into Equations (5.8) and (5.9) and obtain rate equations [19, 71] that we can use to evaluate the laser devices we build and measure,

$$\frac{dN}{dt} = \frac{\eta_i L_{in}}{\hbar\omega_p V_a} - v_g g(N)P - N\left(\frac{1-\beta+F_p\beta}{\tau_{sp}}\right) - AN - CN^3 \tag{5.19}$$

$$\frac{dP}{dt} = -\frac{P}{\tau_{ph}} + \Gamma F_p \beta \frac{N}{\tau_{sp}} + \Gamma v_g g(N) P \tag{5.20}$$

where gain is approximated by $g(N) = g_0 \ln(N/N_{tr})$. Typical values of coefficients and material parameters for III-V semiconductors emitting at 1.3 to 1.5 μm are listed in Table 5.1. Since precise data may not exist for the InGaAsP or InAsP/InP QWs we use in this work, approximations based on published values for similar materials are used in our rate equation analysis.

Table 5.1: Values used in rate equation calculations

Parameter	**Symbol**	**Value**	**Notes**
Surface recombination coefficient	A	$3.5 \sim 4.5 \times 10^7$ s^{-1}	1.3 μm InAsP
Surface recombination velocity	v_{sr}	$4 \sim 6 \times 10^5$ cm.s^{-1} $1 \sim 2 \times 10^5$ cm.s^{-1} $\leq 10^4$ cm.s^{-1}	GaAs bulk and QW [181] InGaAs/GaAs QW [171] InP bulk [182]
Auger recombination coefficient	C	$3.4 \sim 5.1 \times 10^{-29}$ cm^6.s^{-1} 5×10^{-29} cm^6.s^{-1}	1.3um InAsP [183] 1.55um InGaAsP [184]

The rate equations we have derived rest on several assumptions. First, we model the device as a two-level system, as the most probable carrier transitions in semiconductor lasers are the valence and conduction bands. This is certainly not the case when the gain material has more complex energy levels, such as with gas lasers. Second, the above rate equations are for single-mode devices, where stimulated emission into other modes are negligible. Third, non-radiative recombinations other than surface and Auger are negligible, for example, recombination due to defects or impurities in the crystal or at the epitaxial layer interfaces. While the rate equation analysis in this work, as well as those for similar devices by other researchers, shows that these assumptions are valid, we need to keep them in mind if future data questions their correctness.

To fit measured L-L curve to the rate equations, we find the steady-state solutions of Equations (5.19) and (5.20) by setting $dN/dt = 0$ and $dP/dt = 0$. Solving for steady-state photon density PN and input optical power $L_{in}(N)$, we have

$$P(N) = \frac{-\Gamma F_p \beta N}{\tau_{sp}\left[\frac{1}{\tau_{ph}} + \Gamma v_g g(N)\right]} \tag{5.21}$$

$$L_{in}(N) = \frac{\hbar\omega_l V_a}{\eta_i}\left[v_g g(N)P + N\left(\frac{1-\beta+F\beta}{\tau_{sp}}\right) + AN + CN^3\right] \tag{5.22}$$

At the same time, output optical power is given by $L_{out} = \hbar\omega_l P V_{eff}/\tau_{ph}$. It is convenient to think of N as the independent variable here, and calculate the corresponding photon density and input power accordingly.

We apply the definition of threshold for high $F_p\beta$ microlasers by Björk and colleagues [21]—*the threshold of a laser is described by the pump power (or current) needed to bring the mean cavity photon number to unity*—to Equation (5.21) to obtain the threshold carrier density N_{th} and threshold gain $g_{th} = g(N_{th})$. Assuming carrier density and gain above threshold are clamped at their threshold values [71], we can obtain expressions for threshold power and fit the stead-state solutions to measured L-L curves.

One more useful metric of laser characteristics that is embedded in the rate equations is the differential quantum efficiency η_d, defined as the number of photons out per electron measured in the above-threshold regime of laser operation. In electrically pumped lasers, it is [71]

$$\eta_d = \frac{e}{\hbar\omega_l}\frac{\Delta L_{out}}{\Delta I} \tag{5.23}$$

In optically pumped lasers, we can redefine it as the number of photons out per photon in,

$$\eta_d = \frac{\Delta L_{out}}{\Delta L_{in}} \tag{5.24}$$

5.4 Thick-slab lasers

We discussed in Section 3.3 the feasibility of making a photonic crystal laser in an optically-thick slab. Based on the cavity design outlined earlier, we fabricate the thick-slab lasers in an InGaAsP slab with thickness $T = 606$ nm. The wafer's epitaxial design is shown in Table 4.1. We defined the photonic crystal cavities using high-contrast electron-beam lithography with thick HSQ resist and high temperature Ar/Cl_2 CAIBE. The sacrificial InP layer was removed in a selective wet chemical

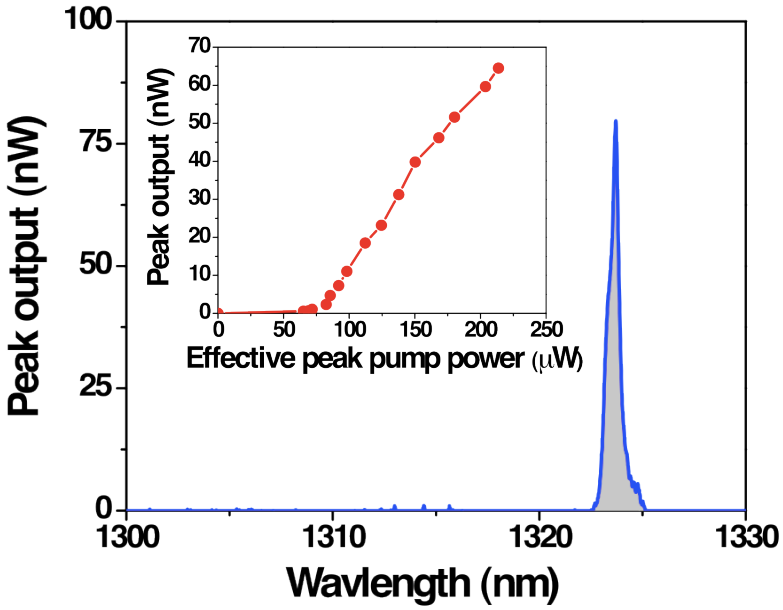

Figure 5.3: Characteristics of the thick-slab laser: single mode spectrum, inset is the L-L curve when the device is pumped at 1 MHz and 2% duty cycle.

etch of $H_2CrO_4/HF/H_2O$. Particulars of the fabrication recipes are detailed in Section 4.4. SEM images of finished devices are shown in Figure 4.8.

The thick-slab microlasers are photopumped at room temperature using a 832 nm laser diode with a 1 MHz repetition rate and 2% duty cycle. L-L curve and lasing spectrum for one of the devices is shown in Figure 5.3. We compare the lasing wavelength of 1323.7 nm with the resonance wavelength from FDTD simulations, and confirm that the laser emission comes from one of the degeneracy-split dipole modes. The linewidth in the figure may seem wider than should be for a laser, although a resolution of 0.1 nm was used in the spectral scan. The reason is that when pumped at 2% duty cycle, thermal chirping in the cavity results in significant frequency noise [86, 185]. We assume that the pump light undergoes multiple reflections at the slab and substrate interfaces and the fraction that overlaps with the cavity area is absorbed. Thus, 20% of the incident power contributes to carrier generation in the slab; the effective peak pump power is estimated to be 78 μW [101].

With these results, we show that photonic crystal cavities in optically-thick slabs can have enough Q to achieve room temperature lasing. Although the present work only demonstrates optically pumped devices in pulsed operation, we believe that improvement in material quality—such as

InAsP/InP QWs used coupled-cavity and nanobeam photonic crystal laser presented in subsequent sections—can help us achieve CW lasing, and that we can take advantage of the increased slab thickness to better design p-i-n doped epitaxial layers for more efficient current injection.

5.5 Coupled-cavity lasers

We show experimental measurements of fabricated devices and fit the measured data to laser rate equations to estimate the lasers threshold, spontaneous emission coupling factor β, as well as the 1.5 μm wavelength emitting InAsP/InP QW material properties for future nanolaser designs in this not yet commonly used material system.

Our devices are formed in an InP slab with a thickness T of 240 nm on top of a 1.16 μm thick sacrificial InGaAs layer. The InP slab contains 4 InAsP QWs with the photoluminescent emission peak at 1550 nm. The samples are fabricated using electron beam lithography on PMMA resist, followed by CAIBE with Ar/Cl_2 to form the air holes and an oxygen plasma to remove the residual resist. Finally, the InGaAs layer is etched away in a dilute H_2CrO_4/HF mixture to suspend the InP/InAsP PhC slab. The best performing devices have a lattice period of a = 470 nm and air hole radius of r = 0.3a. Figure 4.9 shows SEM images of finished devices.

5.5.1 L-L curve and rate equation analysis

The coupled-cavity lasers are measured in a photoluminescence set-up at room temperature, pumped continuously with a $\lambda_p = 832$ nm diode laser. The pump laser beam is focused to an approximately 4 μm diameter spot on the sample surface using a 50$\times$ microscope objective. Emitted light from the devices is collected through the same objective and recorded using an optical spectrum analyzer (OSA). Finite-difference-time-domain (FDTD) simulations reveal that the coupled-cavities in Design A have several resonance modes within the InP/InAsP QW material's gain spectrum, among which the highest Q mode has a Q of 3100, while all other modes have Q of a few hundred to 1300. In Design B, the highest Q mode within the photoluminescence bandwidth is 1700, all other modes have Qs of below 1000. Only the highest Q mode, whose mode profile is shown in Figure 3.19, tends to achieve

the lasing threshold condition, making our devices single-mode lasers, as is evidenced in measured lasing spectra shown in Figure 5.4. CCD camera images of lasing devices are shown in insets. They represent vertically directed Poynting energy flux P_z from the lasing mode at approximately one lasing wavelength above the devices' top surface. The corresponding FDTD simulations of this Poynting flux distribution, i.e. $(\omega_l/2\pi)\int_0^{2\pi/\omega_l} P_z(x,y,z\approx\lambda_l)dt$, where ω_l is the angular frequency of the lasing mode, confirm the main features in the lobed patterns seen on CCD: Design A has two major side lobes, Design B has a bright center with four minor lobes.

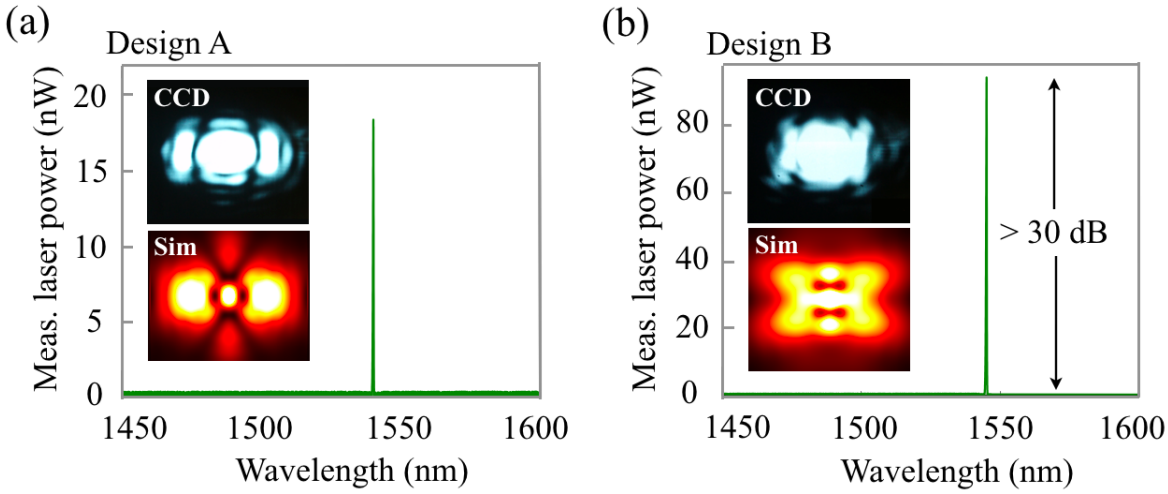

Figure 5.4: Lasing spectra of coupled-cavity lasers, insets show CCD camera image of the lasing device and the corresponding FDTD simulation results: (a) Design A; (b) Design B.

InAsP/InP QWs have the potential advantage of higher temperature and lower threshold operation, due to their greater band-edge offset and thus better carrier confinement compared with the commonly used InGaAsP/InP QW slabs [186]. However, this material system has not received much attention for 1.55 μm wavelength-scale lasers. We proceed to characterize our best performing device using Design B to provide more insight into device performance and material properties. First, we analyze the measured light-in versus light-out (L-L) curve using the rate equations derived in Section 5.3, Equations (5.19) and (5.19), reproduced below

$$\frac{dN}{dt} = \frac{\eta L_{in}}{\hbar\omega_p V_a} - v_g g(N)P - N\left(\frac{1-\beta+F_p\beta}{\tau_{sp}}\right) - AN - CN^3$$

$$\frac{dP}{dt} = -\frac{P}{\tau_{ph}} + \Gamma F_p \beta \frac{N}{\tau_{sp}} + \Gamma v_g g(N) P$$

where gain is approximated by $g(N) = g_0 \ln(N/N_{tr})$. The ratio of pump power that generates carriers in the active region η, the transparency carrier density N_{tr}, β, the spontaneous recombination lifetime τ_{sp}, and Purcell factor F_p are variables in the fit, from which the carrier density N, the photon density P, the pump power L_{in}, and the device output power L_{out} are calculated. The independent variables and their respective values are summarized in Table 5.2.

Table 5.2: Material and device parameters used in rate equation analysis [71]

Parameter	Value
Effective modal volume V_{eff}	0.223 μm^3
Confinement factor Γ	0.0966
Surface recombination velocity v_s	10^4 cm/s
Propagation distance to suface d_a	2×10^{-5}
Surface recom. rate $A = v_s/d_a$	5×10^8 /s
Auger recombination rate C	4.25×10^{-29} cm^6/s

We fit the L-L curve to a range of likely gain coefficient $g_0 = 1000 \sim 2000$ cm^{-1}. The rate equation fit results are consistent despite changes in g_0. Lasing threshold is 14.6 μW, very low for a 4-QW device with an effective mode volume V_{eff} of $1.9(\lambda/n)^3$. Transparency carrier density is about 1×10^{18} cm^{-3}. τ_{sp} is $4 \sim 7$ ns. Purcell factor F_p is between 1 and 1.5 due to InP/InAsP QW material's homogeneous broadening at room temperature and the coupled-cavity's somewhat large V_{eff} [19]. $F_p\beta \approx 0.01$. The fit with $g_0 = 1500$ cm^{-1} is shown in Figure 5.5(a). In measuring the coupled-cavity laser's L-L curve, the device was pumped to over 100 nW as recorded by the OSA, and we expect it to operate stably at even higher powers. The lasing peak is easily ≥ 30 dB above noise level in our measurement. We estimate that about 1 percent of the laser's output power is coupled to the OSA due to loss through optical elements in the optical path from the device to the OSA. Thus the coupled-cavity laser's output power is on the order of 10 μW.

5.5.2 Linewidth narrowing

One important consequence of high power, room temperature CW laser operation is that the lasing linewidth $\Delta\lambda_l$ is not smeared by phase noise from thermal chirping and narrows as output power

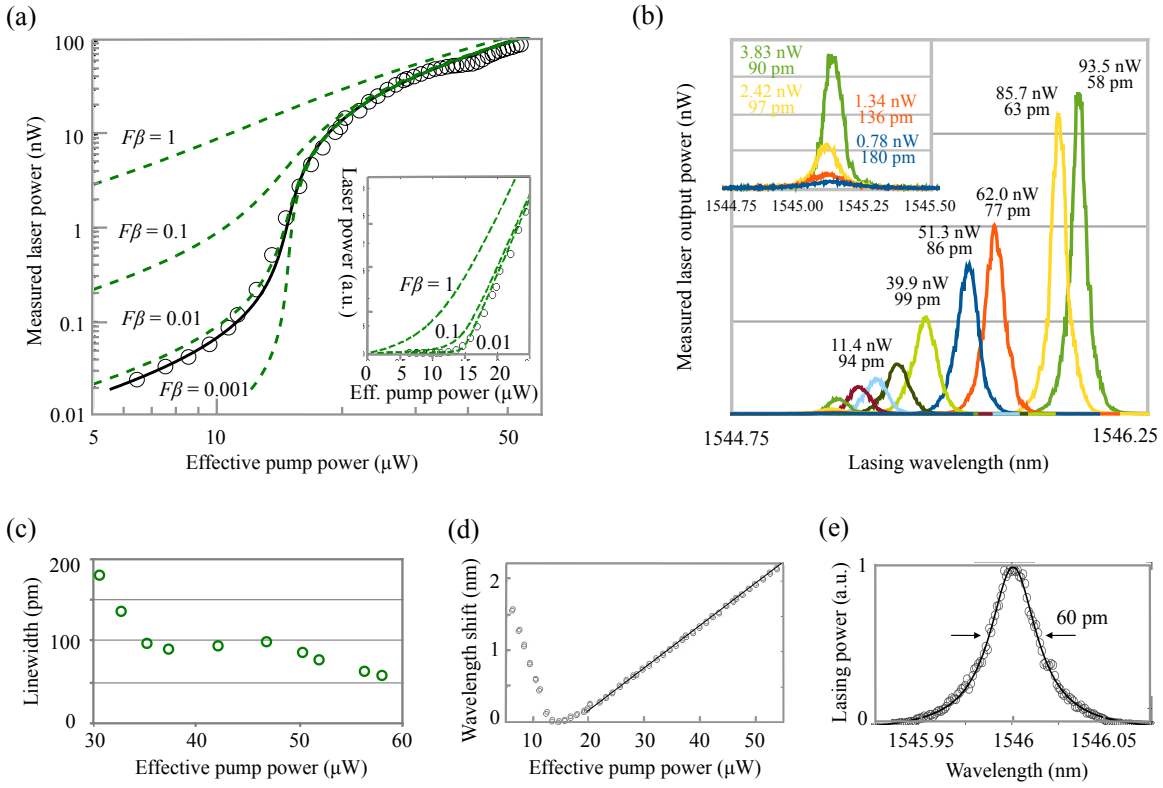

Figure 5.5: Design B device measurements: (a) rate equation fitted L-L measurement on log-log scale, circles represent measured data, solid black line is the fit, calculated $F_p\beta = 1$, 0.1, 0.01, and 0.001. L-L curves using the fit data are in green dashed lines. Inset shows a zoom-in at the threshold in linear scale. (b) Linewidth narrowing and wavelength shift at different pump powers. (c) Lasing linewidth as a function of pump power. (d) Measured wavelength shift versus effective pump power, solid line is the above-threshold $d\lambda/dW$ fit. (e) Measured linewidth, solid line shows the Lorentzian fit.

increases [71, 86]. This ability to obtain narrow linewidth directly influences the device's performance in applications such as spectroscopy and coherent optical communication. We measure the lasing spectrum at different pump powers and overlay the data in Figure 5.5(b), which shows both a linewidth narrowing and a wavelength red-shift when the effective pump power increases from 30 μW to 60 μW. $\Delta\lambda_l$ as a function of pump power is extracted and plotted in Figure 5.5(c). At threshold, phase transition into lasing results in a pronounced kink in the linewidth decrease [164]. To determine the actual achievable linewidth when the coupled-cavity device is pumped at high powers, Figure 5.5(e) shows a single linewidth measurement when the device is pumped at 3 times the threshold pump power. The data is fitted to a Lorentzian. We find that the FWHM $\Delta\lambda_l$ is 60 pm. Measurement accuracy is limited by the OSA's minimum achievable resolution of 15 pm.

5.5.3 Device thermal resistance

Another feature seen in Figure 5.5(b) is that lasing frequency shifts with increasing pump intensity as the combined result of blue shift due to carrier plasma effect with increased free carrier density in the cavity and red shift due to device heating. A more detailed measurement of lasing wavelength shift versus effective pump power is plotted in Figure 5.5(d), clearly showing free carrier dominant blue-shift below threshold and heating dominant red-shift above threshold. The red-shift measures to be 0.059 nm/μW. From this data, one can estimate the device's thermal resistance

$$R_{th} = \frac{dT}{dW} = \frac{d\lambda}{dW}\left(\frac{d\lambda}{dT}\right)^{-1} \tag{5.25}$$

where $d\lambda/dW$ is the pump power dependence of emission wavelength, and $d\lambda/dT$ is the temperature dependence of wavelength. We further decompose the temperature dependence into

$$\frac{d\lambda}{dT} = \frac{d\lambda}{dn}\frac{dn}{dT} \tag{5.26}$$

$d\lambda/dn$ is easily calculated using FDTD simulation. For the coupled cavity in Design B, it is 456.5 nm/RIU.[3] dn/dT is the temperature dependence of the refractive index of InP, which has been well documented. At $\lambda \sim 1.5$ μm and $T = 350$ K, $dn/dT = 2.2 \times 10^{-4}$ K^{-1} [187, 188]. Thus the thermal resistance of our device is

$$R_{th} = \frac{d\lambda}{dW}\left(\frac{d\lambda}{dn}\right)^{-1}\left(\frac{dT}{dn}\right) = 6.15 \times 10^5 \text{ K/W} \tag{5.27}$$

or 0.615 K/μW, a value comparable to devices of the same dimensions made in InGaAsP QW materials [96]. This lead us to conjecture that the low N_{tr} and high thermal tolerance of InP/InAsP QW materials contribute significantly to the low threshold, high power room temperature CW operation achieved here.

5.5.4 Conclusion

The coupled-cavity lasers demonstrate very stable and high power room temperature CW single-mode operation on the order of 10 μW, with a very low threshold of 14.6 μW despite having 4 QWs as the gain material and a larger cavity area compared with single-defect cavities. They have directional emission with 40% of the light emitted from the lasers top surface and have a FWHM beam divergence of $\pm 20^\circ$ in the x-direction and $\pm 8^\circ$ in the y-direction. The devices exhibit one of the narrowest linewidths reported so far in photonic crystal lasers. For comparison, Kita and colleagues reported a linewidth of 60 pm for point-shift lasers suspended in air [86]. This makes the coupled-cavity lasers useful for applications ranging from refractive index sensing to being the light source for potential on-chip optical signal processing. The larger area coupled-cavity will be advantageous in applications where both the laser output power and the threshold are of concern.

However, the cavity's large V_{eff} of $1.9(\lambda/n)^3$ precludes it from showing enhanced spontaneous emission—a sharp threshold transition remains. Moreover, the 2D photonic crystal slab experiences significant influence from substrate feedback, partially evidenced by the obvious modification of far-field radiation pattern by the size of the underlying air-gap h (Figure 3.20). In the next section, we

[3] RIU is an acronym for refractive index unit.

proceed to address these two weaknesses using a nanobeam photonic crystal laser design.

5.6 Nanobeam photonic crystal lasers

The nanobeam photonic crystal cavities are designed in hope of showing lasing with enhanced spontaneous emission due to their high $F_p\beta$, and of finding out more about the InP/InAsP QW material's thermal tolerance as nanobeams are expected to have much higher thermal resistance than the 2D slab photonic crystal cavities. Our devices are made in the InP/InAsP QW material detailed in Chapter 4. They are defined using e-beam lithography with FOx resist, followed by Ar/Cl_2 CAIBE, dipped in HF to remove residual resist, and finished with $H_2CrO_4/HF/H_2O$ wet etch and critical point drying to remove the sacrificial 1.06 μm thick InGaAs layer. The devices we fabricated include a range of design parameters: $a = 430 \sim 480$ nm in steps of 10 nm, $W = 1.06a$, $s = 0$, 18, 34, and 52 nm. SEM images of the finished devices are shown in Figure 4.10.

5.6.1 Lasing at different duty cycles

Using the photoluminescence set-up described in Section 5.1, we excite the nanobeam photonic crystal cavities at room temperature with a $\lambda_p = 830$ nm pump laser. FDTD simulation predicts a single resonant mode within the InP/InAsP QWs' gain spectrum. Modulating the pump laser at 1 MHz, we tune the duty cycle from 5% through to 100% CW. At $\leq$10%, lasing is observed in all of the devices, with emission wavelength λ_l ranging from 1314 nm to 1524 nm depending on their design geometries a and s as well as variation in dosage during e-beam lithography. Although the InP/InAsP material exhibits such a large gain spectrum, only single mode operation is observed for each individual nanobeam device. Because the QW material is designed for peak gain at $\sim$1550 nm, devices lasing at shorter wavelengths have higher threshold, lower output power, and many stop lasing when the pump duty cycle increases. Devices with $\lambda_l > 1500$ nm have noticeably better performance.

We focus our attention on two of the best performing devices, whose parameters are detailed in Table 5.3, to further analyze their characteristics. Pumping the devices at 5% $\sim$ 15%, we can

measure a bright single-mode laser peak within a 1250 nm to 1650 nm spectrum span. We note that at 15%, the pump pulse width of 150 ns is already much longer than any recombination time scale in the device, corresponding to a quasi-CW regime of operation. The laser signal is $\geq$ 17 dB above background noise. As we turned up the pump power, the devices showed little sign of thermal degradation at higher powers. The *L-L* curves at these duty cycles show a soft turn-on at threshold transition that is a trait of high $F_p\beta$ lasers with enhanced spontaneous emission into the lasing mode [19, 21, 22]. Examples of *L-L* curves and broadband spectra measured on Device B are shown in Figure 5.6. In all of the *L-L* plots in this section, peak effective pump powers are reported. Peak pump power is the time-averaged power measured with a photodiode divided by the duty cycle. Effective power points to the fact that the 4-μm diameter pump spot size is much larger than the nanobeam photonic crystal cavities' footprint on chip. Peak pump power is then multiplied by the fraction of the pump spot that overlaps the device to obtain *peak effective pump power*. This method provides an estimate of the upper bound of pump power, since not all of the light incident on the cavity is absorbed. Due to the >10 dB transmission loss in the optical path from the device to the OSA, we are unable to obtain much data below the threshold.

Table 5.3: Design parameters of two select devices for further characterization

Device	a (nm)	W (nm)	s (nm)	Q	V_{eff} (μm^3)	V_{eff} $(\lambda/n)^3$	λ_l (nm)
A	480	510	52	4050	0.0908	0.720	1514
B	480	510	34	6500	0.0810	0.646	1510

We then turn up the duty cycle to 30%, 50%, 70%, and 90%. Fringed radiation patterns as seen on CCD camera remain, though dimmer at higher duty cycles. The single-mode peak remains on the spectral measurement, however with decreasing contrast until 10 dB above background noise at 90% duty, see Figure 5.6(c)–(e). The *L-L* plots show threshold transitions indicative of lasing. When we pump the device in CW condition, however, the fringe pattern disappears, a diffuse spot of light from the cavity is seen on the CCD instead. In spectra measured by the OSA, the single-mode peak all but disappears. Eliminating the 100 ns turn-off time in going from 1 MHz 90% duty cycle to CW pumping, the devices cease to show any sign of lasing.

It would seem then the nanobeam photonic crystal cavities show quasi-CW operation up to 90%.

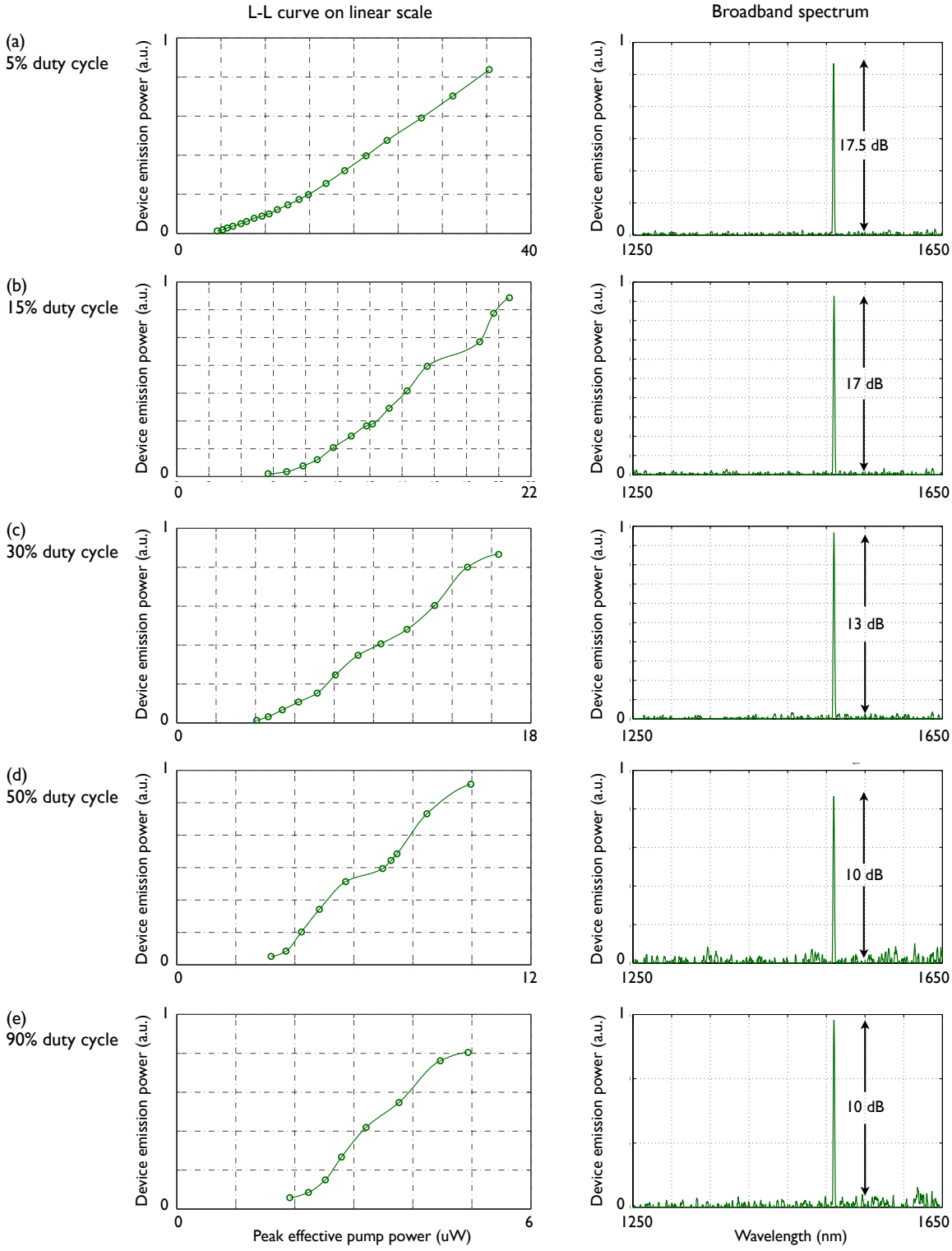

Figure 5.6: L-L curves and broadband spectra of Device B optically pumped at various duty cycles. Duty cycles are (a) 5%, (b) 15%, (c) 30%, (d) 50%, and (e) 90%. $Q = 6500$ from FDTD simulation, $V_{eff} = 0.646(\lambda/n)^3$.

When we overlay each device's L-L curves at different duty cycles as shown in Figure 5.7, however, we immediately see large differences in the dL_{out}/dL_{in} efficiency between lower and higher duty cycles. dL_{out}/dL_{in} is the differential quantum efficiency η_d [71]. In fact, η_d at 5% duty cycle is 16 times that with 90% duty cycle for Device A, and 10 times for Device B. This much decrease in efficiency would be due to increased heating at higher duty cycles. Similar temperature dependent effects have been observed InGaAsP diode lasers [189]. As a comparison, the dL_{out}/dL_{in} contrast between below and above threshold should be much greater, for example, the coupled-cavity laser in Section 5.5 has an above-threshold dL_{out}/dL_{in} 350 times that of below-threshold. Another characteristics of higher duty cycles of 50% and above, the devices are pumped to a saturated output power at less than three times the apparent threshold, beyond which any extra pump power results in the same output level or lower. In Figure 5.7, L-L curves of $30\% \sim 90\%$ end at the pump power where the device begins to show saturated output power. While it is likely that the nanobeam devices are lasing at duty cycles up to 90%—second order photon correlation experiments would be needed to validate the coherence of the devices' emission—we believe that their low η_d and output power saturation renders them unsuitable for device applications including refractive index sensing, spectroscopy, or optical signal processing.

The nanobeam photonic crystal cavities are designed for small V_{eff} and single resonant mode within the InP/InAsP QWs' gain spectrum, in hope to experimentally realize characteristics of high $F_p\beta$ lasers. The L-L curves in Figure 5.6 show reasonably soft turn-on at threshold transitions. We proceed to fit the data to the laser rate equations, Equations (5.19) and (5.20) in Section 5.3, to extract values of threshold $L_{in,th}$ and β.

The InP/InAsP QW material is not as well characterized as commonly used materials such as InGaAsP, we estimate its material parameters based on several assumptions: first, surface and Auger recombination coefficients A and C are similar to those of InP, detailed in Table 5.2; second, g_0 is similar to other III-V indium compound semiconductors, in the range of $1000 \sim 2000$ cm^{-1}; third, $\tau_s p$ should be on the order of a few ns. If we assume that the spectral linewidth $\Delta\lambda$ of the InAsP QWs is similar to the 4.3 meV in InGaAsP, then we can use Equation (2.28) to calculate F_p. We

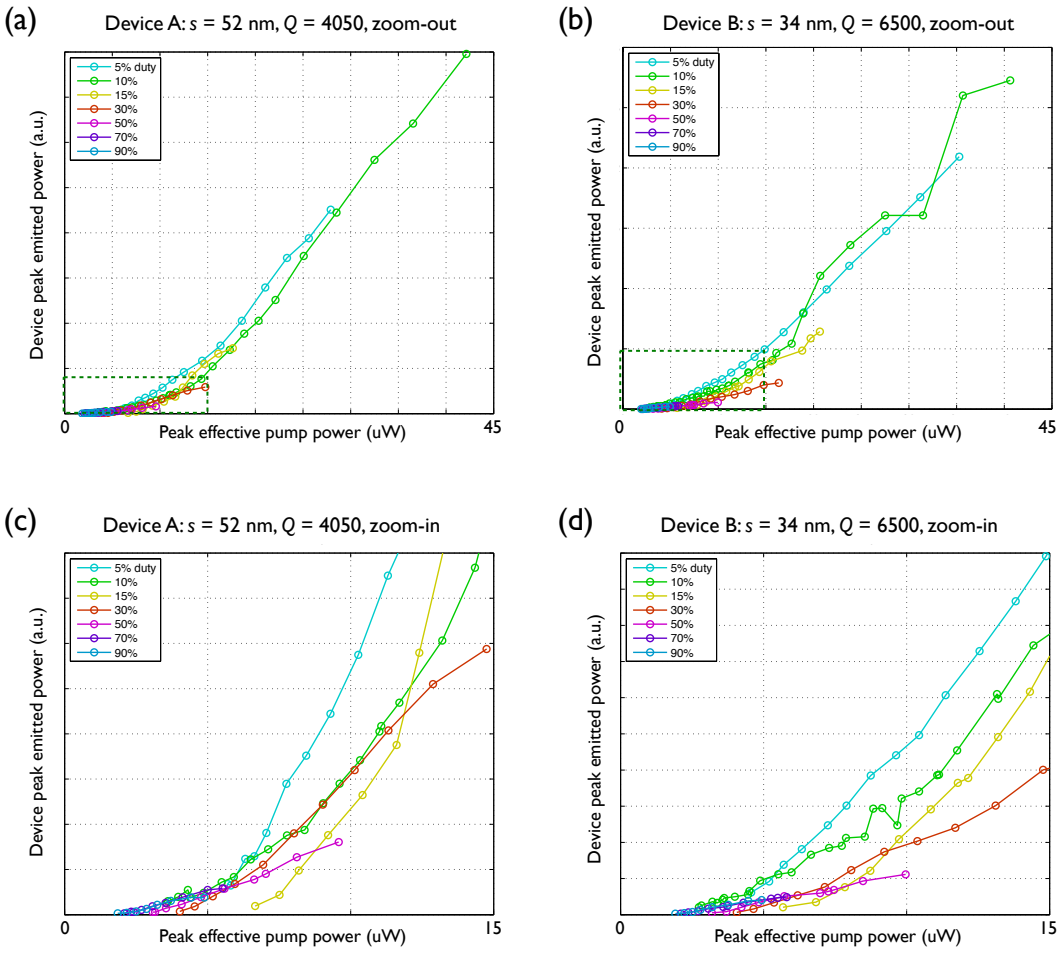

Figure 5.7: *L-L* curves of Devices A and B on linear scale. (a) and (b) shows all measured data. (c) and (d) are zoom-ins of when pump power is low. They correspond to the area enclosed by the green dotted line in (a) and (b), respectively.

use the F_p value thus obtained as the upper bound, and vary F_p between it and 1 in the process of rate equation fit. Unlike the coupled-cavity lasers, where the threshold is a pronounced kink in the linear L-L plot and the data on log-log scale is a distinct S-shape, the soft threshold transition of the nanobeam devices means that their log-scale L-L curve is a shallow S-shape. Moreover, due to the devices' low threshold, we could not gather data much below threshold. These two reasons, plus the large number of fit variables in the rate equation analysis (N_{tr}, τ_{sp}, β, and η), result in a range of values for the fit variables that all give similar goodness of fit. Nevertheless, fitted values for $F_p\beta \approx 0.25 \sim 0.45$ and $L_{in,th} \approx 6 \sim 8$ μW are consistent regardless of other fit parameters' values. An example rate equation fit with minimized fit error and reasonable parameter values is shown in Figure 5.8 for Device B pumped at 30% duty cycle.

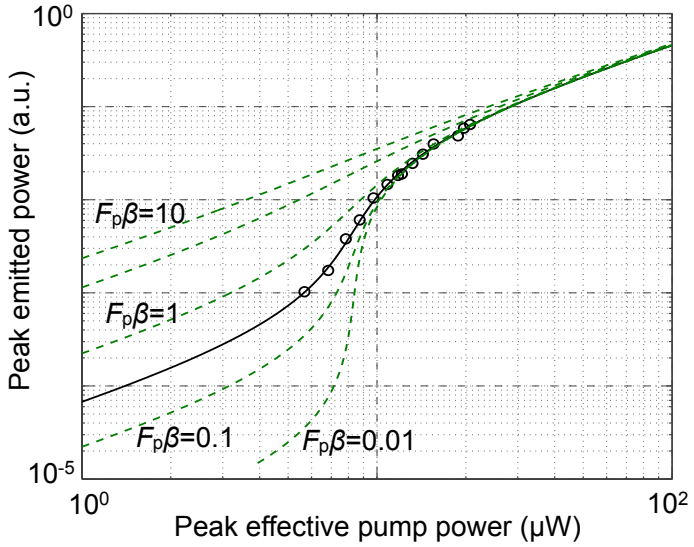

Figure 5.8: Rate equation fitted to measured L-L curve for Device B pumped at 30% duty cycle. Values of fitted rate equation variables are $N_{tr} = 7.4 \times 10^{17}$ cm$^(-3)$, $\tau_{sp} = 6 \times 10^{-9}$ s, $F_p\beta = 0.3$, $L_{in,th} = 6.8$ μW.

5.6.2 Device thermal resistance

We expect the main reason that we were not able to push the nanobeam photonic crystal lasers to CW operation is high thermal resistance R_{th}. Even larger area lasers such as microdisk or

H7 photonic crystal cavity[4] can have thermal resistance as high as 10^6 K/W. The air-suspended nanobeams confine light into an even smaller volume that is connected to less semiconductor material for heat dissipation; the device thermal resistance must be higher. We estimate R_{th} using the same method elaborated in Section 5.5.3. We measure $d\lambda/dW$ and plot the data in Figure 5.9. Unsurprisingly, $d\lambda/dW$ increases monotonically with pump duty cycle. At 90% duty cycle, $d\lambda/dW$ is 0.2446 nm/μW for $s = 52$ nm and 0.2948 nm/μW for $s = 34$ nm. For both designs, FDTD simulations give $d\lambda/dn \approx 442$ nm/RIU. Using Equation (5.27), R_{th} of the nanobeam photonic crystal lasers is 2.63 $\sim$ 3.18 K/μW, five times higher than the coupled-cavity lasers. Moreover, dT/dW at 90% duty only gives us an estimate, R_{th} for true CW operation would be even higher and, in our devices, seems to be the last straw that prevents room temperature CW lasing.

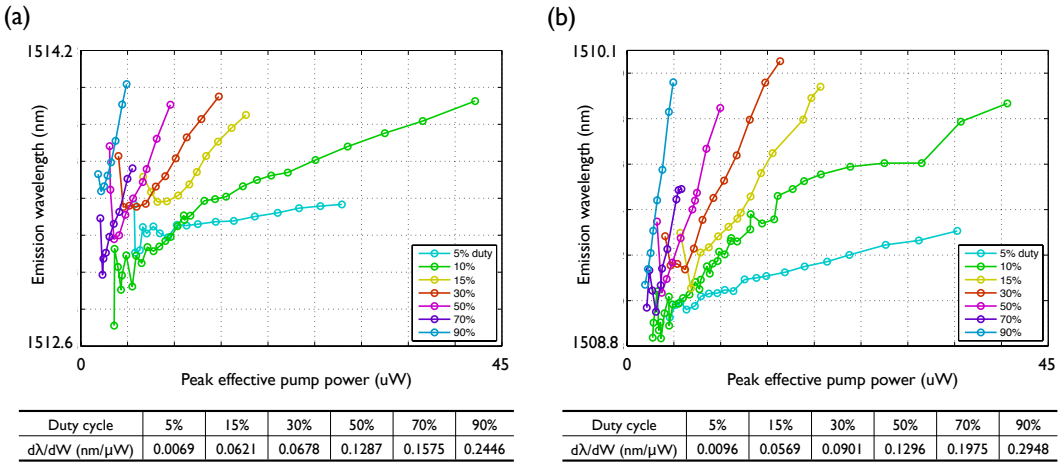

Duty cycle	5%	15%	30%	50%	70%	90%
dλ/dW (nm/μW)	0.0069	0.0621	0.0678	0.1287	0.1575	0.2446

Duty cycle	5%	15%	30%	50%	70%	90%
dλ/dW (nm/μW)	0.0096	0.0569	0.0901	0.1296	0.1975	0.2948

Figure 5.9: $d\lambda/dW$ measurements at different pump duty cycles: (a) $s = 52$ nm, $Q = 4050$, $V_{eff} = 0.720(\lambda/n)^3$; (b) $s = 34$ nm, $Q = 6500$, $V_{eff} = 0.646(\lambda/n)^3$.

5.6.3 Emission directionality

We notice obvious difference in the radiation pattern from devices with different s. We calculated the far-field radiation pattern of the nanobeam photonic crystal lasers in Section 3.5 and showed that emission directionality can vary significantly when $s = 0$ versus $s \geq 18$ nm, see Figure 3.24. This effect is clearly seen in the CCD camera image of lasing devices. In Figure 5.10(a), the left most

[4] An H7 cavity in a triangular photonic crystal lattice is formed by removing a center air-hole and six layers of air-holes surrounding the center[96].

image is that of a device with $s = 0$. Its emission pattern as seen on the CCD has left and right lobes, corresponding to the two intensity local maxima near $\pm 30^\circ$ in the x-direction in the corresponding far-field radiation pattern in Figure 5.10(b). The two bright spots north of the two-lobed main spot are light reflected from an adjacent nanobeam 6 μm away. They disappear in devices well isolated from other structures in the y-direction. In contrast, the CCD images of s = 18, 34, and 52 nm devices all show a bright oval center spot, corresponding to the intensity maximum within $\pm 15^\circ$ from surface normal in their corresponding FFT calculated far-field pattern in Figure 5.10(b). The respective emission directionality of devices with different s is further confirmed by large domain FDTD simulation, shown in Figure 5.10(c), where even finer features of the emission pattern, such as decreasing amount of light emitted to $>60^\circ$ in the x-direction when s increases from 18 nm to 52 nm, is clearly seen. The fabricated nanobeam lasers confirm our simulation results that increasing s at the center of the cavity vastly improves the emission directionality and the amount of laser output power collected.

5.6.4 Conclusion

We designed nanobeam photonic crystal cavities with small V_{eff} of $0.44 \sim 0.72\,(\lambda/n)^3$ and single resonant mode with the gain spectrum of the In/InAsP QW material used in this study, with the goals to experimentally realize high $F_p\beta$ lasing with soft threshold transition and to investigate the behavior of the InP/InAsP material in these high thermal resistance devices. We demonstrate reliable room temperature single-mode lasing with up to 30% duty cycle at 1 MHz repetition rate, a threshold of $6 \sim 8$ μW effective peak pump power, and $F_p\beta$ of $0.25 \sim 0.45$. Laser-like L-L behavior and single-mode emission spectrum are observed up to 90% duty cycles; however, the differential quantum efficiency becomes 10% of the value at lower duty cycles and output power saturates quickly due to thermal effects. Based on measurements of emission wavelength as a function of pump power, we estimate the devices' thermal resistance at 90% to be about 3 K/μW. Lastly, we confirm in experiment that emission directionality is much improved by introducing a small distance s in the middle of the cavity, as predicted in FDTD and FFT calculations in Section 3.5.

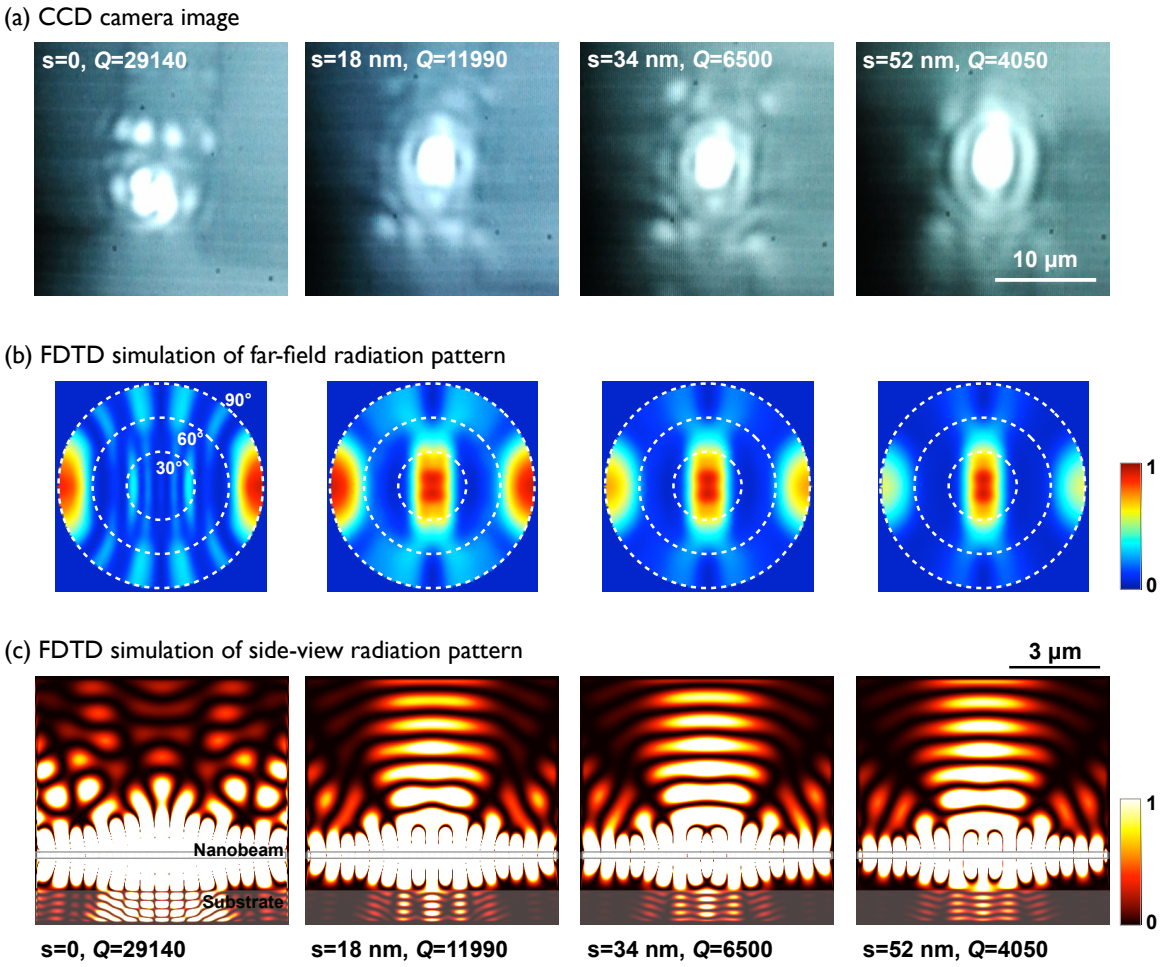

Figure 5.10: Radiation directionality of nanobeam photonic crystal cavities, tuned by varying s: (a) seen on CCD camera; (b) FFT calculation of far-field radiation pattern based on FDTD near-field simulation, dotted white lines indicate 30°, 60°, and 90° from surface normal; (c) y-z plane side-view of radiation patterns from the devices from FDTD simulation, locations of the nanobeam and the substrate are indicated. Columns 1 to 4 correspond to $s = 0$, 18, 34, and 52 nm, respectively. Scale bars for (a) and (c) are shown.

Concurrent with this work, room temperature nanobeam photonic crystal lasers were achieved by other researchers in the field, with InGaAsP QWs under 0.27% [190] and 1% duty cycle pulsed operation [60] as well as with InAs/InGaAs QDs embedded in GaAs under CW pumping using λ_p that is below the bandgap of GaAs [191].

Chapter 6

Integrated silicon waveguide devices

Applications of strong light confinement are not limited to laser cavities; another important class of device applications is on-chip photonic networks using low-power nonlinear optics. With high concentration of light in a small volume, material nonlinearity becomes a stronger influence on the optical modes it carries. A wide array of lower-power nonlinear operations have been under intense investigation, most on the CMOS-compatible silicon-on-insulator (SOI) platform, including all-optical modulators [192, 193, 194, 195], electro-optic modulators [196, 197, 198, 199, 200], memories [201, 202], receivers [203], and parametric amplifiers [204].

Devices that generate or process optical signals with high speed and large bandwidth are much in demand as we seek to transmit and process information faster and in higher volume in both the telecommunication and computer industries [205, 206, 207]. In this picture, lasers are useful for signal generation and electrical-to-optical signal conversion. At the same time, passive devices on the SOI platform find large potential in optical signal processing. Concurrent with the laser work presented in previous chapters, we too ventured to study a few silicon photonic devices. We begin this chapter with theory of strip and slot SOI waveguide designs. Relevant fabrication methods are explained and recipes used to make the silicon photonic devices in work are detailed. We then proceed to discuss our work to realize low V_π polymer-clad electro-optic modulators. Lastly, we characterize the nonlinear loss particular to the small dimensions of silicon strip waveguides, which should find application in the design and optimization of all devices with similar waveguide dimensions.

6.1 Single-mode silicon waveguide

Silicon photonic devices begin with waveguide construction on a SOI wafer. Most of the SOI wafers have a 110 $\sim$ 250 nm Si device layer on top of a 1 $\sim$ 3 μm thick low-index SiO_2 cladding, which rests on a 300 $\sim$ 900 μm thick Si handle wafer. The wafers we use have a 110-nm thick device layer and the SiO_2 layer is 1-μm thick. The waveguide takes the form of a strip waveguide where light is guided by the Si strip's high refractive index, a slot waveguide where light is guided by the sub-100 nm narrow slot between two silicon strips, or a photonic crystal waveguide where the guided modes have a frequency that is in the background photonic crystal's PBG. Figure 6.1(a)–(c) show the geometry of these three designs. We will only concern ourselves with the strip and slot waveguides that are used in this work.

Strip waveguides confine light in the high refractive index silicon, $n_{Si} = 3.48$ compared with $n_{SiO_2} = 1.53$ at λ=1.55 μm. The lowest order guided mode is a quasi-TE mode with the E-field mainly in the x-direction. Its E_x mode profile by FDTD simulation is shown in Figure 6.1(d). To contain light in an even smaller volume, the slot waveguide is designed. Boundary conditions that result from Maxwell's equations dictate that, at the interface of two media and in the absence of surface free charge, the perpendicular components of **D**-field and the parallel components of **E**-field are continuous across the boundary [208],

$$D_{Si}^{\perp} - D_{air}^{\perp} = \varepsilon_{Si} E_{Si}^{\perp} - \varepsilon_{air} E_{air}^{\perp} = 0 \tag{6.1}$$

$$E_{Si}^{\parallel} - E_{air}^{\parallel} = 0 \tag{6.2}$$

Then for quasi-TE modes, the major component of E-field is perpendicular to the Si-air-Si interfaces in the slot, and $E_{air} = n_{Si}^2 E_{Si} = 12.1 E_{Si}$. This strong confinement of E-field in the air-slot is shown by the FDTD results in Figure 6.1(e).

The fabrication procedure of silicon waveguide is much simpler than structures in III-V materials, because by-products of a silicon etch using common Group VII compounds such as fluorides

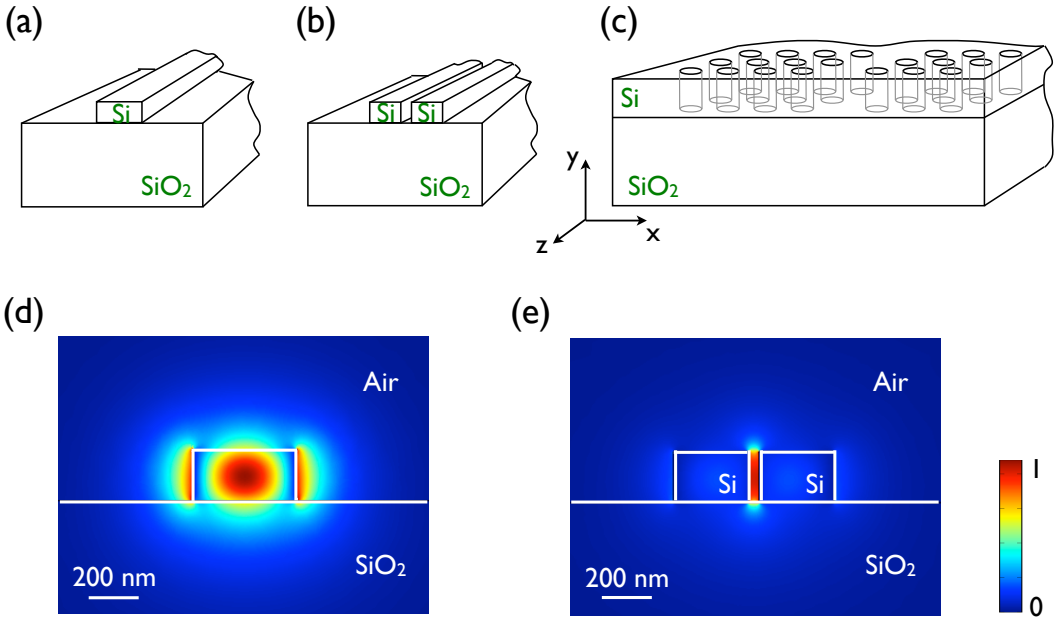

Figure 6.1: Types of Si waveguide on the SOI platform: (a) strip waveguide; (b) slot waveguide; (c) photonic crystal waveguide; (d) FDTD simulation results of transverse E-field in a strip waveguide; (e) FDTD simulations transverse E-field in a slot waveguide.

and chlorine are readily volatile. Silicon tetrafluoride is a gas at room temperature, and silicon tetrachloride has a melting point of -70 °C and a boiling point of 57.6 °C [152]. Thus, lithography and dry etching of silicon structures do not impose as much requirement on sample temperature or etch mask's etch resistance compared with our discussions in Chapter 4.

The silicon waveguides fabricated in this work are first defined using electron beam lithography using ZEP520A or HSQ resist. ZEP520A is spun at 4000 RPM, then baked at 180 °C for 3 minutes. It requires a dosage of 190 μC/cm^2 under 100 kV electron beam acceleration voltage. 6% HSQ dissolved in methyl isobutyl ketone (MIBK)[1] is spun at 3000 $\sim$ 4000 RPM and baked at 170 °C for 2 minutes. The required dosage is 900 $\sim$ 1100 μC/cm^2. Etches are carried out with either reactive-ion etch (RIE) using SF_6 or ICP-RIE using SF_6/C_4F_8 chemistry. Residual resist is removed by oxygen plasma in the case of ZEP520A and a very quick buffered HF dip for HSQ.

To test single-mode waveguide devices, we need to couple light from a laser into the waveguide via either free-space collimation and focusing with lenses or fiber optics. All of the silicon photonic

[1]Purchased from Dow Corning Silicones.

devices presented in this thesis are fiber optically interrogated with the use of grating couplers [209].

6.2 Low V_π polymer-clad on-chip electro-optic modulators

Electro-optic (EO) modulators are useful devices to increase the speed and bandwidth of telecommunication and potentially of on-chip interconnects in computers [210, 211]. They most often take the shape of a Mach-Zehnder modulator (MZM)—the input laser beam is split equally into two arms, one or both of which have an index of refraction that can be altered by an electrical voltage, and then recombined with constructive or destructive interference to give high or low intensity output optical signal. When the electrical voltage equals the device's half-wave voltage V_π, the split laser beams undergo a π-phase shift with respect to each other and recombine with destructive interference. Consequently, V_π, $V_\pi L$, power consumption, modulation speed, and bandwidth are the main figures of merit to quantify the performance of an MZM with waveguide length L and active material EO coefficient r_{ijk} defined as [23]

$$\Delta\eta_{ij} = \eta(\mathbf{E}) - \eta(0) = \Delta\left(\frac{1}{n^2}\right)_{ij} = r_{ijk}E_k \tag{6.3}$$

where $\eta = \varepsilon_0/\varepsilon$ is the impermeability tensor, ε here is the dielectric tensor, and $\mathbf{E}$ is the applied electric field. Summation is taken over repeated subscript indices.

Commercial EO modulators use nonlinear crystals that exhibit Pockels effect, most notably lithium niobate $LiNbO_3$. Intrinsic silicon is a poor source of EO activity; its crystal structure has inversion symmetry and precludes Pockels effect. EO activity in silicon can come from carrier injection to obtain free-carrier dispersion effect [212]. Polymeric materials including liquid crystals and chromophore doped EO polymers have attracted attention as cheaper and easier materials to integrate on to the SOI platform. Lastly, there are modulators based on Frank-Keldysh or quantum confined Stark effects.

Prior to and concurrent with this work, researchers have pursued several approaches to minimize V_π. Commercial fiber-coupled lithium niobate EO modulators have the high bit rate frequency of

40 Gb/s, bandwidth of 40 GHz, and a typical V_π of about 4 V [213]. Green and colleagues utilized free-carrier dispersion effect to achieve a low V_π of 1.8 V with a 10 Gb/s bit rate frequency and RC cut-off at 16 GHz [200]. EO polymers in sol-gel geometries seek to integrate the high EO coefficient nonlinear polymers in on-chip waveguide form. Enami and colleagues demonstrated V_π of 0.65 V by implementing this design [214, 215].

In this project, we aimed to build low V_π, low power consumption modulators by integrating chromophore doped EO polymers on to the SOI platform. Our material choice has several reasons. First, unlike nonlinear crystals, polymers are easy to integrate with on-chip silicon photonic devices, often by spin casting. Second, synthesized EO polymers have shown a large bandwidth of about 100 GHz [216] and a high EO coefficient of $r_{33} = 100 \sim 180$ pm/V [214]. Lithium niobate has $r_{33} \approx 30$ pm/V [23]. Third, compared with carrier injection devices, EO polymers allow for electrostatic operation and thus lower power consumption. Fourth, they have extremely fast response time to external E-field [194, 217]. Lastly, synthetic polymers are relatively cheap materials to manufacture and process.

6.2.1 Device design

To design polymer-integrated silicon photonic devices, we must first understand how the EO polymers work. The polymers we worked with are active chromophores doped in an inert host polymer with cross-linkers [217]. When the chromophores are aligned and locked in that orientation in the host polymer, their collective response to an external E-field results in Pockels effect. We used a chromophore labeled YLD_124 doped 25% by weight in an amorphous polycarbonate poly[bisphenol A carbonate-co-4,4'-(3,3,5-trimethylcyclohexylidene) diphenol carbonate] [218].

One way to integrate the EO polymer into the SOI waveguide is to dissolve the polymer in a solvent, trichloroethylene (TCE) in our case, spin cast the solution on to fabricated silicon waveguide, and bake at and elevated temperature but below the polymer's glass transition temperature T_g to evaporate the solvent. Refer to Figure 6.1(d)–(e), where the waveguide is exposed to air will be covered in the polymer. We face two main requirements for effective device design. First, there should

be a large overlap between the optical mode and the polymer. In the simplest strip waveguide, most of the light is confined in the silicon, little of the optical signal sees the EO polymer, thus requiring a large V_π or much longer devices to achieve the π phase difference in the MZM's two arms. In comparison, slot waveguide is a suitable design that concentrates the optical mode in what is to be a polymer-filled slot. The final device has waveguide dimensions of 300×110 nm^2 cross-section for each silicon strip and a slot width of 120 nm.

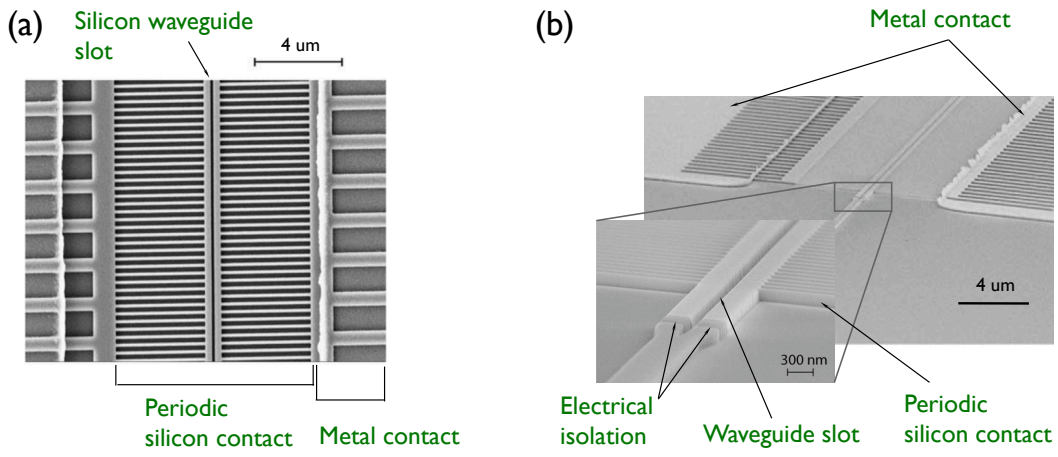

Figure 6.2: SEM images of devices after fabrication and before EO polymer application: (a) top view; (b) tilted view.

Second, the EO polymer has a very high resistivity of 10^{11} Ω-cm [219], so the two silicon strips that form the slot waveguide can also be used as electrodes for modulation. This has the advantage that the externally applied voltage drop will be across the 120 nm slot instead of across the several microns between electrodes that is typically required for polymer waveguide implementation of EO polymers [215, 220]. The challenge presented, however, is to bring the voltage to the silicon waveguide without bringing conductors too close to the optical mode. Conductors, whether in the form of metal contact or highly doped silicon, can cause excessive optical absorption. A strip-loaded geometry has been developed for carrier-injection modulators [196, 198, 199]; however, this requires a two-step dry etch with aligned electron-beam lithography. Our solution is to link the waveguide to metal contacts via a periodic set of thin silicon contact arms. With a periodicity of 300 nm and

arm width of 100 nm, the contact arms are largely transparent to the optical mode in the waveguide [221]. The metal contacts are then placed 4 μm away from the slot waveguide. SEM images of the slot waveguide with period contact arms are shown in Figure 6.2.

The modulators are made on SOI wafers using electron-beam lithography and dry etching methods outlined in Section 6.1. Aluminum contacts are added using aligned photolithography and lift-off. The YLD_124 chromophore and the amorphous polycarbonate host polymer are weighed out, dissolved in TCE, and spun on to the fabricated SOI chip. The sample is baked to evaporate the solvent, and the excess polymer covering the electrical probe contacts is wiped off with a solvent soaked cotton swab. The procedure is summarized in Figure 6.3(a). The sample is now ready for poling to align the chromophores. In our design, voltage drop across the two MZM arms can be independently adjusted. We apply poling voltage with anti-symmetry as shown in Figure 6.3(b)1, where $V_{pole} = 150$ V/μm. Thus, we can apply symmetric voltage to drive the modulator in a push-pull configuration to minimize V_π. As the poling voltage is applied and held constant, the device is slowly heated up while closely monitoring the current between the ground and V_{pole} electrodes and between V_{pole} and $2V_{pole}$ electrodes. As the device temperature reaches the poling temperature, the monitored current begins to increase rapidly. At this point, we fix the temperature and maintain the device in the current condition for a length of time before rapid cooling to room temperature to lock in the molecular structure. This heated poling process is summarized in Figure 6.3(b)2.

6.2.2 Modulation characterization

We operate the EO modulator in push-pull configuration by applying the driving voltage V_{drive} symmetrically, as shown in Figure 6.4(b), given a poling voltage set-up as shown in Figure 6.4(a). First, a DC voltage is applied; the transmission spectra for different V_{drive} are shown in Figure 6.4(c)–(d). Our MZM are designed to have slightly unbalanced arm lengths of 2 cm and 2.01 cm, resulting in a transmission spectrum with about 10 nm periodicity. The spectra in black are when $V_{drive} = 0$, and red is when $V_{drive} = 0.2$ or 0.4 V is applied. These spectra show that V_π is between 0.2 and 0.3 V.

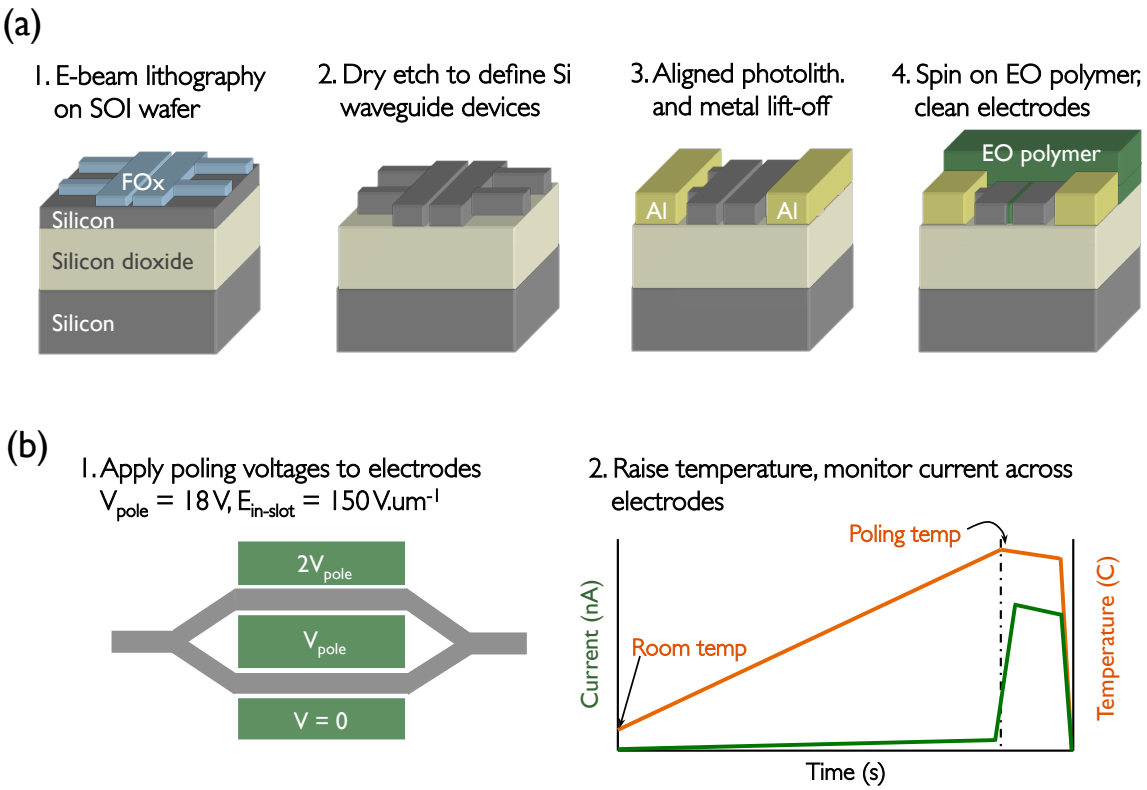

Figure 6.3: Fabrication sequence of polymer-clad EO modulators: (a) waveguide and electrode fabrication; (b) EO polymer poling.

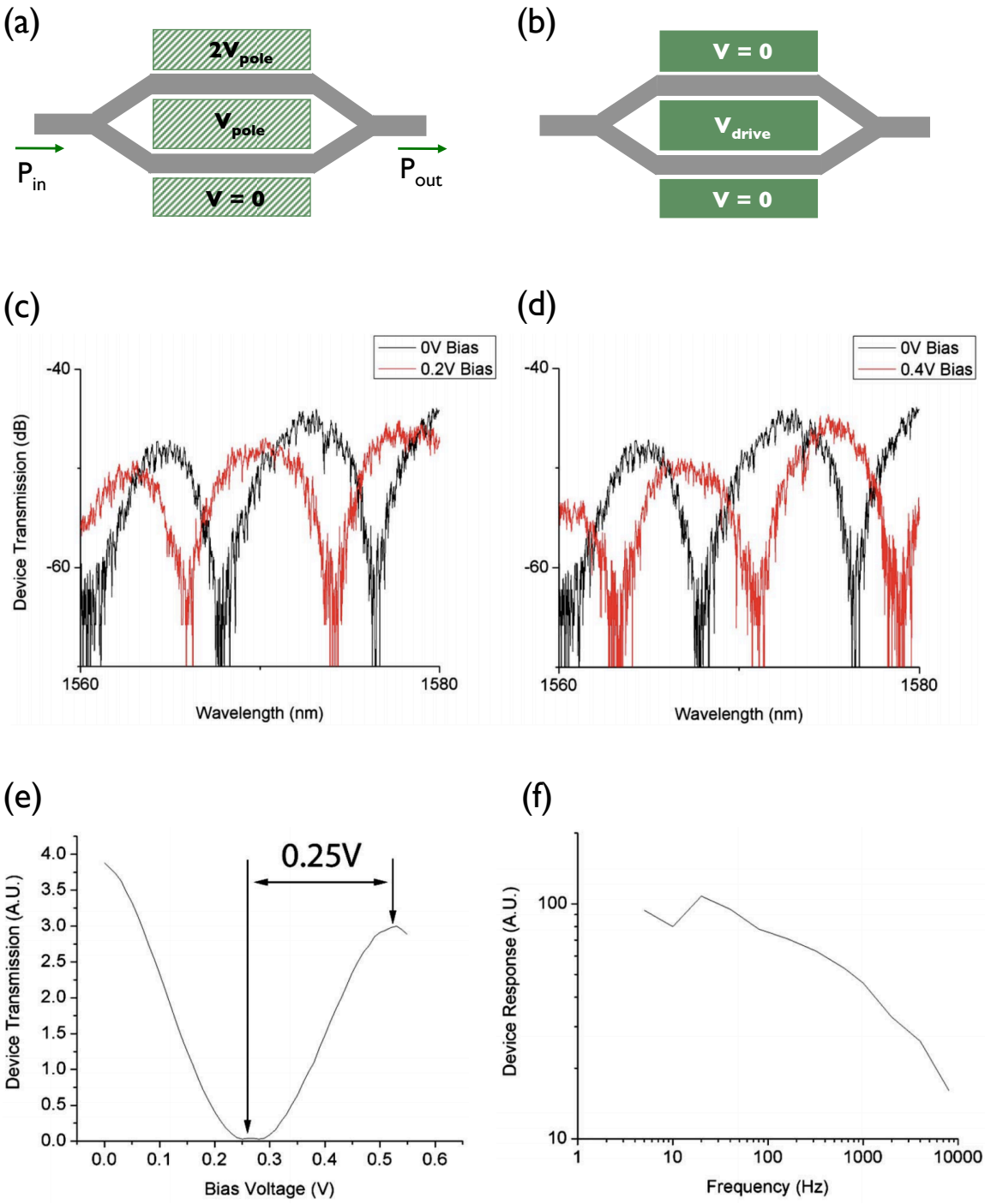

Figure 6.4: Modulator characterization: (a) Voltages applied during device poling; (b) Push-pull voltage configuration during device operation; (c) Optical transmission spectra when $V_{drive} = 0$ and 0.2V DC; (d) Transmission spectra when $V_{drive} = 0$ and 0.4V DC; (e) Device transmission at a fixed wavelength, as V_{drive} is varied between 0 to 0.55 V; (f) Frequency response of the EO modulation.

To precisely determine V_π, the laser is fixed at a constant wavelength, and the transmission signal is measured as a function of V_{drive}. The resulting data in Figure 6.4(e) clearly shows that the voltage difference between constructive and destructive interference in the MZM is $V_\pi = 0.25$ V.

We then measure the EO modulator's frequency response. A sinusoidal AC signal is applied for V_{drive} and also tee'd to the reference of a lock-in amplifier. Output signal from the modulator is detected by a photodetector, whose electrical signal is measured by the lock-in with reference to the AC voltage signal. The lock-in spectrum is given in Figure 6.4(f) and shows severe fall-off at around 1 kHz. We believe the main cause is the RC time constant due to the under-optimized electrical systems. The thin slot in a 2-cm long waveguide implies a large capacitance; the lightly doped silicon and unoptimized silicon-aluminum contact can present significant resistance. In fact, electrical measurement with control device structures reveal that resistance across a 400 μm long waveguide can be over $10^9\,\Omega$. Capacitance on the same 400 μm long segment is 12 fF. Thus, the combined RC time constant can be on the order of millisecond. Calculations show that the speed limit in electrically optimized devices using the current geometry can be 70 GHz [221].

Given the device length of $L = 2$ cm, $V_\pi L$ is 0.5 V-cm. From this, we can calculate that the EO activity from the polymer is $r_{33} \approx 30$ pm/V. This is much lower than the optimal value of 100 pm/V for this particular chromophore [217]. A likely cause is that the polymer in the waveguide slot was not fully poled and aligned [215]. Lastly, we can measure little electrical current across the waveguide slot during EO modulation, indicating negligible power consumption.

In conclusion, we have shown EO modulation by integrating synthetic EO polymers on to the silicon photonic platform with the lowest V_π demonstrated at the time of this work. Optimization of the electrical path to minimize device resistance will significantly bring up the device's operating speed. Improvements in the polymer poling procedure to realize the material's full r_{33} potential will further decrease V_π and $V_\pi L$.

6.3 Nonlinear loss in silicon strip waveguide

Silicon is considered suitable for waveguiding at the telecommunication wavelengths of $1.3 \sim 1.55$ μm, because it is largely a linear material. Its centro-symmetric crystal structure precludes second order nonlinearity of Pockels effect. Third order nonlinearity arises from Kerr effect and two-photon absorption (TPA). Thermo-optic effect causes a change in silicon's refractive index n though not its extinction coefficient κ (imaginary part of the complex index of refraction $\hat{n} = n + i\kappa$). It is by far the largest nonlinearity; its speed is limited to sub-GHz due to the long thermal lifetime on the order of ns. However, we noticed significant nonlinear loss in our experiments with silicon strip waveguides, whose magnitude seems too large to be explained by TPA alone. In this section, we present our investigation into the cause of nonlinear loss in silicon strip waveguide. Measurements are made on silicon strip waveguide of various lengths from 2.6 mm to 1.06 cm. A top-view optical microscope image of a sample waveguide device is shown in Figure 6.5(a). The silicon strip cross-section is 500 nm wide by 110 nm high, forming a single-mode waveguide whose mode profile is similar to that shown in Figure 6.1(d). Our experiments divide into two parts: first, a input versus output power measurement to determine the amount of linear and nonlinear loss in the waveguide; second, a frequency-modulated pump-probe lock-in amplified measurements to ascertain the origin and speed of the nonlinear loss mechanism(s).

6.3.1 Nonlinear loss model by input versus output power measurements

We measure the output power (L_{out}) from a length of waveguide as the input power (L_{in}) is tuned from 20 to 140 mW. The experimental set-up is shown in Figure 6.5(b). An erbium-doped fiber amplifier (EDFA) is used, since our laser diode by itself has a maximum output power of 10 mW. The $L_{out}(L_{in})$ data from two sample devices is plotted in green in Figure 6.6; the waveguide loss is clearly nonlinear. We can fit the data to a generalized nonlinear loss equation,

$$\frac{\partial L}{\partial z} = -\alpha_1 L - \alpha_2 L^2 - \alpha_3 L^3 \tag{6.4}$$

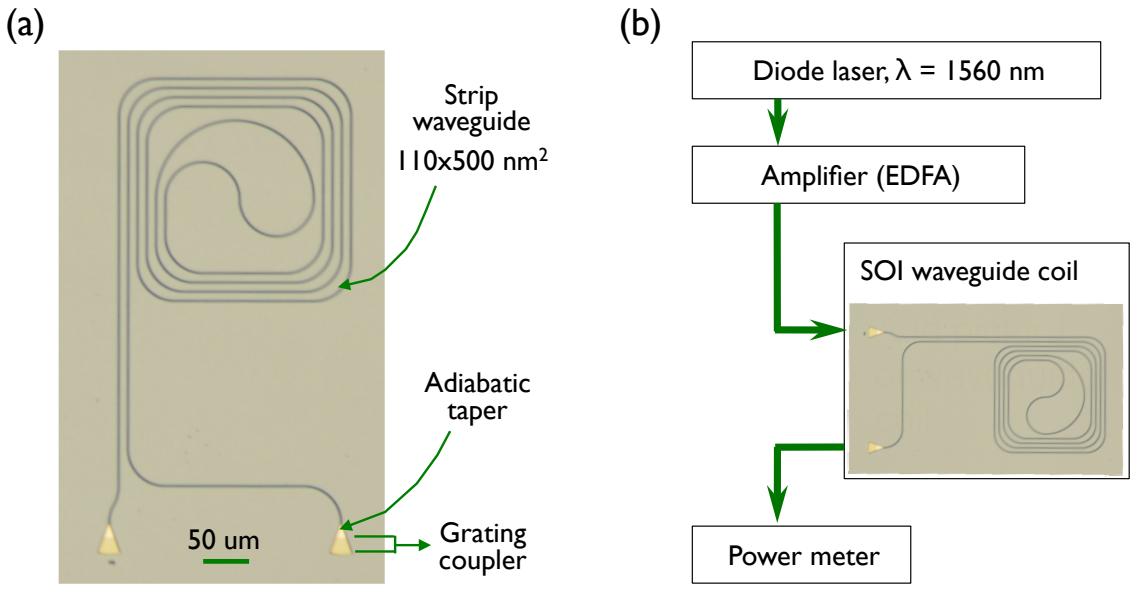

Figure 6.5: Device and experimental set-up used in nonlinear loss measurement: (a) optical microscope image of the waveguide spool device; (b) schematic of the experimental set-up.

where L is optical power. To attribute meanings to the loss coefficients α_1, α_2, and α_3, we need to look at the possible causes of loss.

Loss in silicon strip waveguides can be attributed to four main factors: TPA, free carrier absorption (FCA), radiation loss due to surface roughness, and surface states where the Si crystal lattice terminates. Radiation loss due to surface roughness is expected to be linear. Surface state absorption is usually deemed negligible, and TPA and FCA are the dominant nonlinear losses.

$$\begin{aligned} \frac{\partial L}{\partial z} &= -\text{ Linear loss} - \text{TPA} - \text{FCA} \\ &= -\alpha L - \frac{\beta_{TPA}}{A_{eff}} L^2 - \sigma_{FCA} N L \end{aligned} \tag{6.5}$$

where L is the optical power in the waveguide, α is the linear loss coefficient, β_{TPA} is the two-photon absorption coefficient, A_{eff} is the waveguide effective area, σ_{FCA} is the free carrier absorption cross-section, and carrier density N is caused by TPA and is thus given by

$$N = \frac{\tau_{FCA}\beta_{TPA}}{2\hbar\omega A A_{eff}} L^2 \tag{6.6}$$

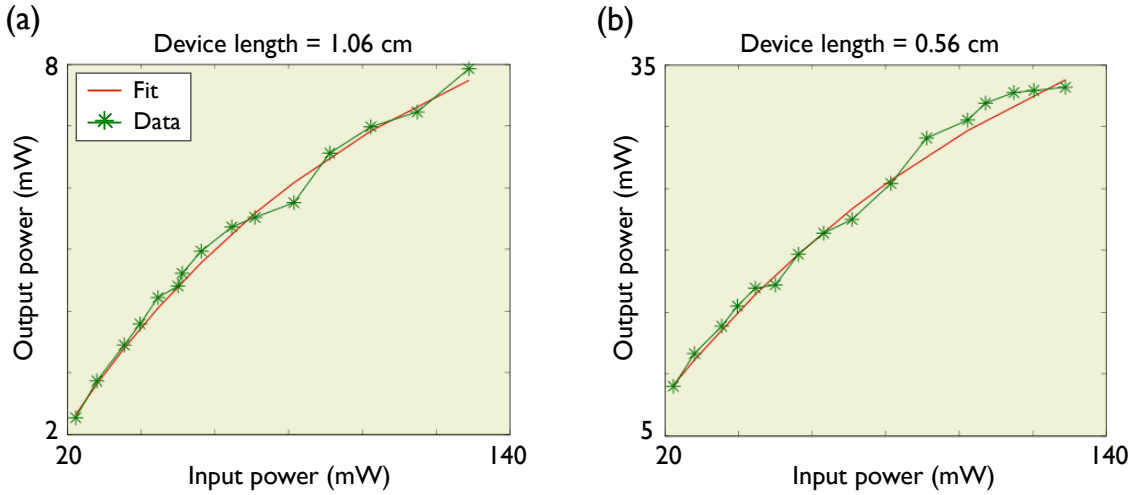

Figure 6.6: Measured and fitted output versus input power from devices with length of (a) 1.06 cm and (b) 0.56 cm.

Therefore, attenuation of a laser signal in a silicon strip waveguide can be modeled as a third order process:

$$\begin{aligned} \frac{\partial L}{\partial z} &= -\alpha_1 L - \alpha_2 L^2 - \alpha_3 L^3 \\ &= -\alpha_1 L - \frac{\beta_{TPA}}{A_{eff}} L^2 - \frac{\sigma_{FCA}\tau_{FCA}}{2\hbar\omega A}\frac{\beta_{TPA}}{A_{eff}} L^3 \end{aligned} \tag{6.7}$$

Fit to the above expression is quite consistent for $L_{out}(L_{in})$ data taken from devices of different lengths: $\alpha_1 = 1.3 \sim 1.9 \times 10^{-4}$ μm^{-1}, $\alpha_2 = 1 \sim 1.5 \times 10^{-6}$ μm^{-1} mW^{-1}, $\alpha_3 = 3 \sim 6 \times 10^{-9}$ μm^{-1} mW^{-2}. Fit curves to data from sample devices are shown in red in Figure 6.6.

Using published material data in our nonlinear loss model Equation (6.7), we obtain the following values for α_2 and α_3 [222, 223, 224, 225],

$$\alpha_2 = \frac{\beta}{A_{eff}} = \frac{5 \sim 9 \times 10^{-12}\,\text{m/W}}{0.1\,\mu\text{m}} = 5 \sim 9 \times 10^{-8}\,\mu\text{m}^{-1}\,\text{mW}^{-1} \tag{6.8}$$

$$\alpha_3 = \frac{\left(\sigma_{FCA} \approx 10^{-17}\,\text{cm}^2\right)\left(\tau_{FCA} \approx 10^{-10} \sim 10^{-8}\,\text{s}\right)}{2\,(0.8\,\text{eV})\,(0.05\,\mu\text{m}^2)}\frac{\beta_{TPA}}{A_{eff}} \approx 10^{-10} \sim 10^{-8}\,\mu\text{m}^{-1}\,\text{mW}^{-2} \tag{6.9}$$

Compare this result with the fit results, we see that the values of α_3 agree, however, the experimentally measured α_2 representing TPA loss is much higher than expected; there is extra loss

contribution that our current nonlinear loss model does not take into account. Published experimental results show that silicon photonic waveguide loss is a strong function of mid-bandgap defects in the crystalline silicon [226, 227]. We postulate that the extra α_2 loss is due to free carriers generated by single photon absorption (SPA) at mid-bandgap defects, mostly surface states in our intrinsic silicon waveguide. The modified nonlinear loss model thus becomes

$$\begin{aligned} \frac{\partial L}{\partial z} &= -\alpha_1 L - \alpha_2 L^2 - \alpha_3 L^3 \\ &= -\alpha_1 L - \left(\frac{\beta_{TPA}}{A_{eff}} + \frac{\sigma_{FCA}\tau_{FCA}}{\hbar\omega A}\alpha_{SPA} \right) L^2 - \frac{\sigma_{FCA}\tau_{FCA}}{2\hbar\omega A}\frac{\beta_{TPA}}{A_{eff}} L^3 \end{aligned} \tag{6.10}$$

where α_{SPA} is the single-photon absorption coefficient, analogous to β_{TPA} for the two-photon process.

Thus far, the nonlinear loss characterization shows that in a single-mode silicon strip waveguide with a 500×110 nm^2 cross-section, nonlinear loss is comparable to linear loss at input power as low as 75 mW. At this power, linear loss is $\alpha_1 \approx 1.6 \times 10^{-4}$ μm^{-1}, while nonlinear loss is $\left(\alpha_2 L + \alpha_3 L^2\right) \approx 1.2 \times 10^{-4}$ μm^{-1}. To prove the contribution of SPA generated FCA to nonlinear loss, whose magnitude outnumbers TPA according to our model, we proceed to frequency-modulated pump-probe experiments in the next section.

6.3.2 Frequency-modulated pump-probe measurements

For pump-probe experiments, we connect a $\lambda_{pump} = 1565$ nm diode laser, whose signal is modulated by a function generator, to an EDFA for the high intensity pump signal. A second diode laser is tuned to $\lambda_{probe} = 1580$ nm for the probe signal. The two laser beams are merged through a fiber beam splitter and coupled into the silicon strip waveguide. The output signal is sent through an optical filter to cut out the pump laser signal, so that the probe signal alone reaches the photodetector. The electrical signal from the photodetector is then sent into a lock-in amplifier, which takes its reference from the same function generator that modulates the $\lambda_{pump} = 1565$ nm diode laser. A schematic of this experimental set-up is shown in Figure 6.7. The lock-in amplifiers cover a frequency range from 40 kHz to 10 MHz. For higher frequencies, a lightwave component analyzer (LCA) is used to

generate the modulated pump optical signal and the reference in measuring the lock-in amplified S-parameter.

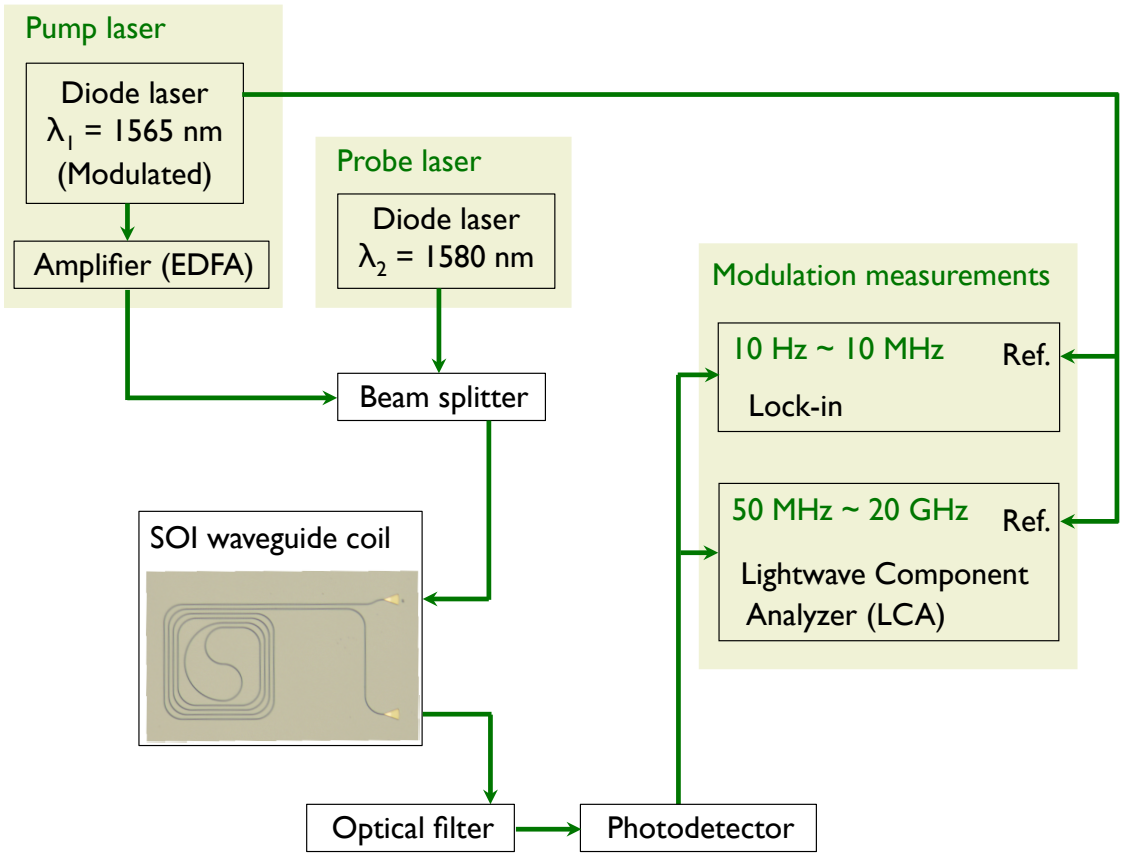

Figure 6.7: Experimental set-up used in pump-probe measurements.

When the high intensity, modulated pump laser and the constant intensity probe laser are sent into the silicon strip waveguide, photon absorption from the pump laser generates free carriers. The free carrier changes the complex index of refraction $\hat{n} = n + i\kappa$ of silicon, which is experienced by the probe laser. When pump laser modulation frequency is slower than $1/\tau_{FCA}$, probe signal modulation by $\Delta\hat{n}$ occurs at the same frequency. Changes in $n = \Re\{\hat{n}\}$ and absorption $\alpha = 4\pi\kappa/\lambda$ due to free carriers can be modeled by the following expressions [212],

$$\Delta n = -\left(e^2\lambda^2/8\pi^2c^2\varepsilon_0 n\right)\left[\Delta N_{e^-}/m^*_{ce} + \Delta N_{h^+}/m^*_{ch}\right] \tag{6.11}$$

$$\Delta\alpha = \left(e^3\lambda^2/4\pi^2c^3\varepsilon_0 n\right)\left[\Delta N_{e^-}/{m^*_{ce}}^2\mu_e + \Delta N_{h^+}/{m^*_{ch}}^2\mu_h\right] \tag{6.12}$$

where e is the elementary charge, ε_0 is the permittivity of free space, n is the refractive index of unperturbed silicon, ΔN_{e^-} is the change in electron density, $m^*_{ce} = 0.26m_0$ is the conductivity effective mass of electrons, ΔN_{h^+} is the change in hole density, $m^*_{ch} = 0.39m_0$ is the conductivity effective mass of holes, m_0 is the rest mass of an electron, μ_e is the electron mobility, and μ_h is the hole mobility. Alternatively, a numerical model can be constructed by fitting to the experimental data presented in the same manuscript [212],

$$\Delta n = -\left[8.8\times10^{-22}\Delta N_{e^-} + 8.5\times10^{-}-18\Delta N_{h^+}^{0.8}\right] \tag{6.13}$$

$$\Delta\alpha = 8.5\times10^{-18}\Delta N_{e^-} + 6\times10^{-18}\Delta N_{h^+} \tag{6.14}$$

With the pump-probe set-up, we seek to test two characteristics of SPA generated FCA, if it is indeed the dominant nonlinear loss factor: first, probe power attenuation has a linear dependence on pump laser power; second, the maximum modulation frequency of the nonlinear loss is limited by the free carrier lifetime in silicon τ_{FCA}. For the former, we measure output probe laser power as a function of input pump laser power at a constant modulation frequency. Collected data for 1 MHz and 10 MHz are shown in Figure 6.8(a). It is evident that the amount of probe laser attenuation is proportional to the pump power, indicating that SPA instead of TPA is the dominant free carrier generation mechanism. To measure τ_{FCA}, we determine the bandwidth of loss in the probe signal using lock-in measurements as the pump laser modulation is swept from 40 kHz to 1.5 GHz. For most of the frequency range, there is clear pump-probe modulation. The modulation signal is anomalously strong at very low frequencies of <1 MHz; we expect it to be due to heating by the pump laser. Further experiments are needed to ascertain this hypothesis. At high frequencies, the pump-probe modulation cuts off at $1 \sim 2$ GHz, giving a effective free career lifetime τ_{FCA} of $0.5 \sim 1$ ns, within the expected range of $0.7 \sim 200$ ns from published data [225, 228, 229, 230, 231, 232].

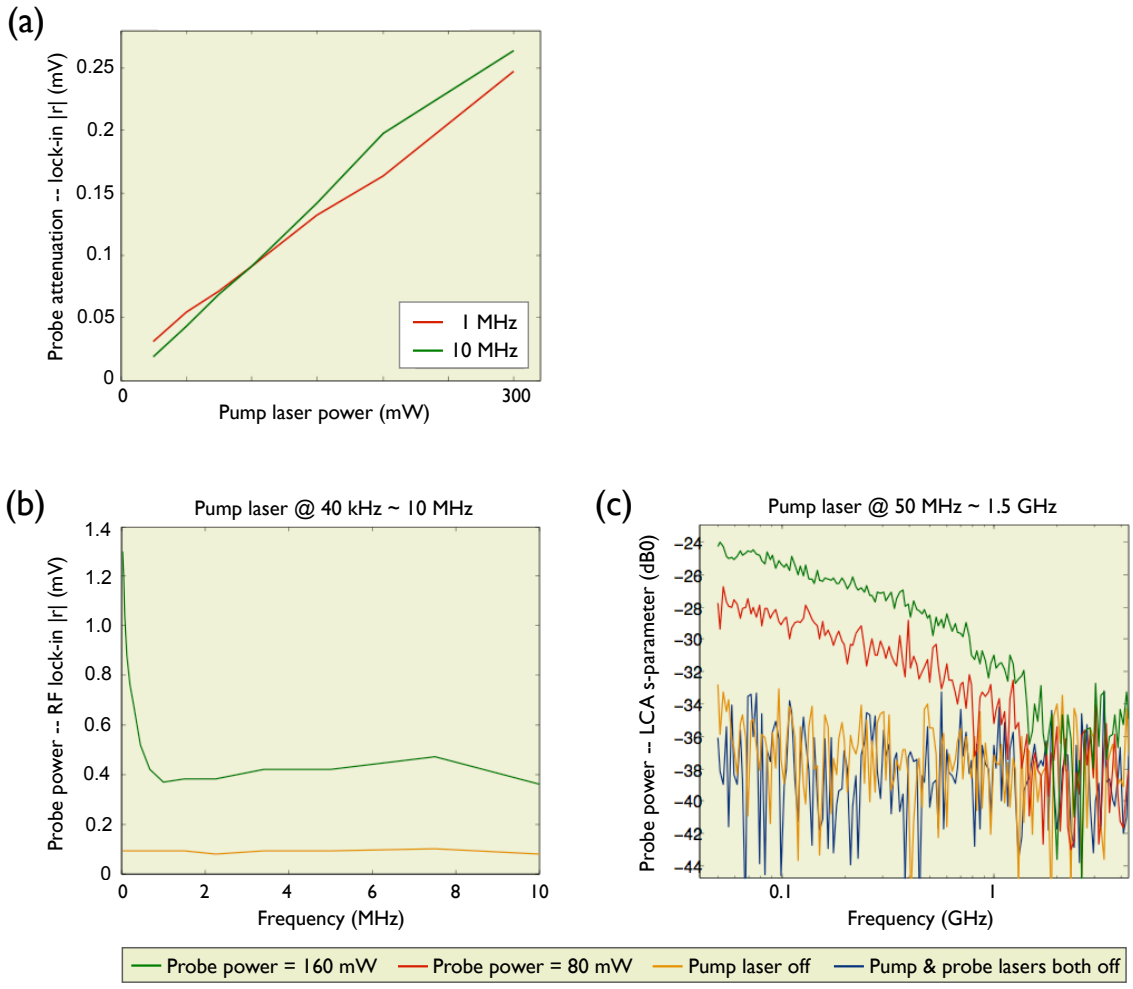

Figure 6.8: Data from pump-probe lock-in amplified measurements: (a) probe power attenuation as a function of pump laser power, measurements performed at 1 MHz and 10 MHz; (b) RF lock-in measurements of probe power at constant pump power, pump frequency is 40 kHz to 10 MHz; (c) LCA measurements of probe power at constant pump power, pump frequency is 50 MHz to 1.5 GHz.

6.3.3 Conclusion

Putting together the results from the nonlinear loss and pump-probe experiments above, we return to our modified nonlinear loss model, Equation (6.10), reproduced below,

$$\begin{aligned}\frac{\partial L}{\partial z} &= -\alpha_1 L - \alpha_2 L^2 - \alpha_3 L^3 \\ &= -\alpha_1 L - \left(\frac{\beta_{TPA}}{A_{eff}} + \frac{\sigma_{FCA}\tau_{FCA}}{\hbar\omega A}\alpha_{SPA}\right) L^2 - \frac{\sigma_{FCA}\tau_{FCA}}{2\hbar\omega A}\frac{\beta_{TPA}}{A_{eff}} L^3\end{aligned}$$

Linear loss coefficient is $\alpha_1 = 5.7 \sim 8.5$ dB/cm $= 1.3 \sim 1.9 \times 10^{-4}\,\mu\text{m}^{-1}$. Fitted value for TPA from the L^3 term gives $\beta_{TPA} = 5 \sim 10 \times 10^{-12}$ m/W, which agrees well with published values of $5 \sim 9 \times 10^{-12}$ m/W [222, 223, 224, 225]. Based on fitted values of β_{TPA} and σ_{FCA}, we can deduce that $\alpha_{SPA} = 7.5 \sim 12 \times 10^{-6}\,\mu\text{m}^{-1}$.

From these numbers, we find that SPA results in a small fraction of the linear loss in our 500×110 nm^2 silicon strip waveguide. However, it generates enough free carriers to cause significant nonlinear loss. Under the comparison, TPA is not the dominant loss mechanism. Our fitted values of β_{TPA} and σ_{FCA} agree well with published values.

Chapter 7

Summary and outlook

The majority of this work is on semiconductor lasers with wavelength-scale confinement of light. We evaluated possible designs to incorporate metals into disk and photonic crystal microcavities, with the goal of lessening thermal degradation, increasing efficiency, and providing an electrical path for current injection operation. We demonstrated very stable room temperature CW single-mode lasing from microcavities with wavelength-scale optical confinement. We showed that coupled-cavities can be used to facilitate single-mode lasing from a somewhat larger area cavity, with the benefits of high output power unhampered by thermal effects. We also experimented with nanobeam photonic crystal lasers that concentrate light in the semiconductor with mode volumes as small as have been reported for purely dielectric cavities. Our results showed room temperature quasi-CW single-mode operation with very soft threshold turn-on—a signature of Purcell enhancement and efficient spontaneous emission coupling into the lasing mode—and good emission directionality.

The objective of translating the optically pumped microlasers into electrically pumped ones still looms. With current injection operation, the lasers would find much wider applications, especially in optical communication and signal processing. The challenge remains to design and optimize the electrical path for minimized parasitic resistance and current leak, but without much compromise to the Q of the optical cavity mode.

In the process of building microlasers, we find that InAsP/InP quantum-confined materials have significant advantage to the commonly used InGaAsP materials for $1.3 \sim 1.55$ μm band light emission, namely, higher band edge offset for better carrier confinement and resistance to thermal degra-

dation, and decreased surface recombination by elimination of Ga that forms surface Ga_xO_y. Our results persuade further exploration of the InAsP/InP material system and development into quantum wires and QDs for future generation light sources.

As we push microlasers to tiny mode volumes and thresholdless-like behavior, we encounter new questions that beg for clarification. One is the measurement of threshold and coherence. Until recently, most of the lasers reported have a pronounced threshold in their light-in versus light-out (L-L) plots. Threshold pump power can be accurately determined by fitting the data to laser rate equations. However, the distinct threshold behavior blurs in high $F_p\beta$ devices. Depending on cavity Q, one can expect a sharp peak in emission spectrum for both below and above threshold. While a narrow linewidth is sufficient for refractive index sensing, applications such as telecom and quantum communication will require more rigorous coherence characterization, for example second order photon correlation function [124, 166] or interferometric coherence length measurements [233].

Another question is the effects of external feedback. Its influence on a diode semiconductor laser's phase noise is well documented [233, 234, 235, 236]. Our studies in this work reinforce that feedback changes microlasers' emission directionality. Moreover, both published results [19] and our experiments [87] advocate cavity Q of several thousand for efficient power output and reduced photon recycling. The modest Q-factor can make the device even more sensitive to external feedback. Smart designs to use external cavities for enhanced laser characteristics or to insulate devices from feedback would be an interesting and useful continuation of our work.

Bibliography

[1] J. D. Jackson, *Classical Electrodynamics*, 3rd ed. Wiley, New York, 1998.

[2] A. Yariv, *Quantum Electronics*, 3rd ed. John Wiley & Sons, Inc., 1989.

[3] E. M. Purcell, "Spontaneous emission probabilities at radio frequencies," *Phys. Rev.*, vol. 69, p. 681, 1946.

[4] G. Björk and Y. Yamamoto, "Analysis of semiconductor microcavity lasers using rate equations," *IEEE J. Quantum Electron.*, vol. 27, p. 2386, 1991.

[5] T. Yoshie, M. Lončar, A. Scherer, and Y. M. Qiu, "High frequency oscillation in photonic crystal nanolasers," *Appl. Phys. Lett.*, vol. 84, p. 3543, 2004.

[6] H. Altug, D. Englund, and J. Vučković, "Ultrafast photonic crystal nanocavity laser," *Nat. Physics*, vol. 2, p. 484, 2006.

[7] J. L. Jewell, J. P. Harbison, A. Scherer, Y. H. Lee, and L. T. Florez, "Vertical-cavity surface-emitting lasers: design, growth, fabrication, characterization," *IEEE J. Quantum Electron.*, vol. 27, p. 1332, 1991.

[8] J. M. Gérard, D. Barrier, J. Y. Marzin, R. Kuszelewicz, L. Manin, E. Costard, V. Thierry-Mieg, and T. Rivera, "Quantum boxes as active probes for photonic microstructures: The pillar microcavity case," *Appl. Phys. Lett.*, vol. 69, p. 499, 1996.

[9] M. Notomi, "Strong light confinement with periodicity," *Proc. IEEE*, vol. 99, p. 1768, 2011.

[10] J. M. Gérard, B. Sermage, B. Gayral, B. Legrand, E. Costard, and V. Tierry-Mieg, "Enhanced spontaneous emission by quantum boxes in a monolithic optical cavity," *Phys. Rev. Lett.*, vol. 81, p. 1110, 1998.

[11] J.-M. Gérard and B. Gayral, "Strong Purcell effect for InAs quantum boxes in three-dimensional solid-state microcavities," *J. Lightwave Technol.*, vol. 17, p. 2089, 1999.

[12] B. Gayral, J.-M. Gérard, B. Sermage, A. Lemaître, and C. Depuis, "Time resolved probing of the Purcell effect for InAs quantum boxes in GaAs microdisks," *Appl. Phys. Lett.*, vol. 78, p. 2828, 2001.

[13] G. S. Solomon, M. Pelton, and Y. Yamamoto, "Single-mode spontaneous emission from a single quantum dot in a three-dimensional cavity," *Phys. Rev. Lett.*, vol. 86, p. 3903, 2001.

[14] R. E. Slusher, A. F. J. Levi, U. Mohideen, S. L. McCall, S. J. Pearton, and R. A. Logan, "Threshold characteristics of semiconductor microdisk lasers," *Appl. Phys. Lett.*, vol. 63, p. 1310, 1993.

[15] O. Painter, R. K. Lee, A. Scherer, A. Yariv, J. D. O'Brien, P. D. Dapkus, and I. Kim, "Two-dimensional photonic band-gap defect mode laser," *Science*, vol. 284, p. 1819, 1999.

[16] P. Michler, A. Kiraz, L. Zhang, C. Becher, E. Hu, and A. Imamoglu, "Laser emission from quantum dots in microdisk structures," *Appl. Phys. Lett.*, vol. 77, p. 184, 2000.

[17] H.-G. Park, S.-H. Kim, S.-H. Kwon, Y.-G. Ju, J.-K. Yang, J.-H. Baek, S.-B. Kim, and Y.-H. Lee, "Electrically driven single-cell photonic crystal laser," *Science*, vol. 305, p. 1444, 2004.

[18] H. Y. Ryu, M. Notomi, E. Kuramoti, and T. Segawa, "Large spontaneous emission factor (> 0.1) in the photonic crystal monopole-mode laser," *Appl. Phys. Lett.*, vol. 84, p. 1067, 2004.

[19] K. Nozaki, S. Kita, and T. Baba, "Room temperature continuous wave operation and controlled spontaneous emission in ultrasmall photonic crystal nanolaser," *Opt. Express*, vol. 15, p. 7506, 2007.

[20] M. T. Hill, Y.-S. Oei, B. Smalbrugge, Y. Zhu, T. de Vries, P. J. van Veldhoven, F. W. M. van Otten, T. J. Eijkemans, J. P. Turkiewicz, H. de Waardt, E. J. Geluk, S.-H. Kwon, Y.-H. Lee, R. Nötzel, and M. K. Smit, "Lasing in metallic-coated nanocavities," *Nat. Photonics*, vol. 1, p. 589, 2007.

[21] G. Björk, A. Karlsson, and Y. Yamamoto, "Definition of a laser threshold," *Phys. Rev. A*, vol. 50, p. 1675, 1994.

[22] M. P. V. Exter, G. Nienhuis, and J. P. Woerdman, "Two simple expressions for the spontaneous emission factor β," *Phys. Rev. A*, vol. 54, p. 3553, 1996.

[23] A. Yariv and P. Yeh, *Photonics: Optical Electronics in Modern Communications*. Oxford University Press, USA, 2007.

[24] S.-W. Chang and S. L. Chuang, "Normal modes for plasmonic nanolasers with dispersive and inhomogeneous media," *Opt. Lett.*, vol. 34, p. 91, 2009.

[25] ——, "Fundamental formulation for plasmonic nanolasers," *IEEE J. Quantum Electron.*, vol. 45, p. 1014, 2009.

[26] B. E. A. Saleh and M. C. Teich, *Fundamentals of Photonics*, 2nd ed. John Wiley & Sons, Inc., Hoboken, NJ, 2007.

[27] J. Huang, S.-H. Kim, and A. Scherer, "Design of a surface-emitting, subwavelength metal-clad disk laser in the visible spectrum," *Opt. Express*, vol. 18, p. 19581, 2010.

[28] E. D. Palik, ed., *Handbook of Optical Constants of Solids I*. Academic, San Diego, Calif., 1998.

[29] N. W. Ashcroft and N. D. Mermin, *Solid State Physics*. Thomson Learning, Inc., 1976.

[30] M. Dressel and G. Grüner, *Electrodynamics of Solids: Optical Properties of Electrons in Matter*. Cambridge University Press, 2002.

[31] S.-H. Kim, "Reference Manual for pFDTD," 2011, unpublished document.

[32] S.-H. Kim, J. Huang, and A. Scherer, "From vertical-cavities to hybrid metal/photonic-crystal nanocavities: towards high-efficiency nanolasers," *J. Opt. Soc. Am. B*, vol. 29, p. 577, 2012.

[33] J. W. S. Rayleigh, "On the maintenance of vibrations by forces of double frequency and on the propagation of waves through a medium endowed with a periodic structure," *Phil. Mag.*, vol. 24, p. 145, 1887.

[34] ——, "On the reflection of light from a regularly stratified medium," *Proc. R. Soc. A*, vol. 93, p. 565, 1917.

[35] J. C. Slater, *Microwave Electronics*. Dover, New York, NY, 1969.

[36] L. Brillouin, *Wave Propagation in Periodic Structures*, 2nd ed. Dover Publications, Inc., Mineola, NY, 1953.

[37] S. L. McCall, P. M. Platzman, R. Dalichaouch, D. Smith, and S. Schultz, "Microwave propagation in two-dimensional dielectric lattices," *Phys. Rev. Lett.*, vol. 67, p. 2017, 1991.

[38] H. A. Harris and C. V. Shank, "Antisymmetric taper of distributed feedback lasers," *IEEE J. Quantum Electron.*, vol. 15, p. 532, 1976.

[39] P. Yeh, A. Yariv, and C.-S. Hong, "Electromagnetic propagation in periodic stratified media. i. general theory," *J. Opt. Soc. Am.*, vol. 67, p. 423, 1976.

[40] P. Yeh, A. Yariv, and E. Marom, "Theory of Bragg fiber," *J. Opt. Soc. Am.*, vol. 68, p. 1196, 1978.

[41] E. Yablonovitch, "Inhibited spontaneous emission in solid-state physics and electronics," *Phys. Rev. Lett.*, vol. 58, p. 2059, 1987.

[42] S. John, "Strong localization of photons in certain disordered dielectric superlattices," *Phys. Rev. Lett.*, vol. 58, p. 2486, 1987.

[43] S. Y. Lin, J. G. Fleming, D. L. Hetherington, B. K. Smith, R. Biswas, K. M. Ho, M. M. Sigalas, W. Zubrzycki, S. R. Kurtz, and J. Bur, "A three-dimensional photonic crystal operating at infrared wavelengths," *Nature*, vol. 394, p. 251, 1998.

[44] S. Noda, K. Tomoda, N. Yamamoto, and A. Chutinan, "Full three-dimensional photonic bandgap crystals at near-infrared wavelengths," *Science*, vol. 289, p. 604, 2000.

[45] K. Aoki, D. Guimard, M. Nishioka, M. Nomura, S. Iwamoto, and Y. Arakawa, "Coupling of quantum-dot light emission with a three-dimensional photonic-crystal nanocavity," *Nature Photonics*, vol. 2, p. 688, 2008.

[46] A. Tandaechanurat, S. Ishida, K. Aoki, D. Guimard, M. Nomura, S. Iwamoto, and Y. Arakawa, "Demonstration of high-Q ($>$ 8600) three-dimensional photonic crystal nanocavity embedding quantum dots," *Appl. Phys. Lett.*, vol. 2009, p. 171115, 2009.

[47] J. P. Zhang, D. Y. Chu, S. L. Wu, W. G. Bi, R. C. Tiberio, R. M. Joseph, A. Taflove, C. W. Tu, and S. T. Ho, "Nanofabrication of 1-D photonic bandgap structures along a photonic wire," *IEEE Photon. Tech. Lett.*, vol. 8, p. 491, 1996.

[48] J. S. Foresi, P. R. Villeneuve, J. Ferrera, E. R. Thoen, G. Steinmeyer, S. Fan, J. D. Joannopoulos, L. C. Kimerling, H. I. Smith, and E. P. Ippen, "Photonic bandgap microcavities in optical waveguides," *Nature*, vol. 390, p. 143, 1997.

[49] Y. Akahane, T. Asano, B.-S. Song, and S. Noda, "High-Q photonic nanocavity in a two-dimensional photonic crystal," *Nature*, vol. 425, p. 944, 2003.

[50] K. Nozaki and T. Baba, "Laser characteristics with ultimate-small modal volume in photonic crystal slab point-shift nanolasers," *Appl. Phys. Lett.*, vol. 88, p. 211101, 2006.

[51] S.-H. Kim, S.-K. Kim, and Y.-H. Lee, "Vertical beaming of wavelength-scale photonic crystal resonators," *Phys. Rev. B*, vol. 73, p. 235117, 2006.

[52] H.-Y. Ryu, M. Notomi, and Y.-H. Lee, "High-quality-factor and small-mode-volume hexapole modes in photonic-crystal-slab nanocavities," *Appl. Phys. Lett.*, vol. 83, p. 4294, 2003.

[53] M. Notomi, T. Tanabe, A. Shinya, E. Kuramochi, H. Taniyama, S. Mitsugi, and M. Morita, "Nonlinear and adiabatic control of high-Q photonic crystal nanocavities," *Opt. Express*, vol. 15, p. 17458, 2007.

[54] M. Palamaru and P. Lalanne, "Photonic crystal waveguides: out-of-plane losses and adiabatic modal conversion," *Appl. Phys. Lett.*, vol. 78, p. 1466, 2001.

[55] P. Lalanne and J. P. Hugonin, "Bloch-wave engineering for high Qs, small Vs microcavities," *IEEE J. Quantum Electron.*, vol. 39, p. 1430, 2003.

[56] B.-S. Song, S. Noda, T. Asano, and Y. Akahane, "Ultra-high-q photonic double-heterostructure nanocavity," *Nat. Mater.*, vol. 4, p. 207, 2005.

[57] E. Kuramochi, M. Notomi, S. Mitsugi, A. Shinya, and T. Tanabe, "Ultrahigh-q photonic crystal nanocavities realized by the local width modulation of a line defect," *Appl. Phys. Lett.*, vol. 88, p. 041112, 2006.

[58] P. B. Deotare, M. W. McCutcheon, I. W. Frank, M. Khan, and M. Lončar, "High quality factor photonic crystal nanobeam cavities," *Appl. Phys. Lett.*, vol. 94, p. 121106, 2009.

[59] M. Notomi, E. Kuramochi, and H. Taniyama, "Ultrahigh-Q nanocavity with 1D photonic gap," *Opt. Express*, vol. 16, p. 11095, 2008.

[60] B.-H. Ahn, J.-H. Kang, M.-K. Kim, J.-H. Song, B. Min, K.-S. Kim, and Y.-H. Lee, "One-dimensional parabolic-beam photonic crystal laser," *Opt. Express*, vol. 18, p. 5654, 2010.

[61] T. Tanabe, M. Notomi, E. Kuramochi, A. Shinya, and H. Taniyama, "Trapping and delaying photons for one nanosecond in an ultrasmall high-Q photonic-crystal nanocavity," *Nat. Photonics*, vol. 1, p. 49, 2007.

[62] W. L. Barnes, A. Dereux, and T. W. Ebbesen, "Surface plasmon subwavelength optics," *Nature*, vol. 424, p. 824, 2003.

[63] W.-D. Li, F. Ding, J. Hu, and S. Y. Chou, "Three-dimensional cavity nanoantenna coupled plasmonic nanodots for ultrahigh and uniform surface-enhanced raman scattering over large area," *Opt. Express*, vol. 19, p. 3925, 2011.

[64] H. J. Lezec, J. A. Dionne, and H. A. Atwater, "Negative refraction at visible frequencies," *Science*, vol. 316, p. 430, 2007.

[65] J. Valentine, S. Zhang, T. Zentgraf, E. Ulin-Avila, D. A. Genov, G. Bartal, and X. Zhang, "Three-dimensional optical metamaterial with a negative refractive index," *Nature*, vol. 455, p. 376, 2008.

[66] J. D. Joannopoulos and S. G. Johnson, *Photonic Crystals: Molding the Flow of Light*, 2nd ed. Princeton University Press, Princeton, NJ, 2008.

[67] K. Ishizaki and S. Noda, "Manipulation of photons at the surface of three-dimensional photonic crystals," *Nature*, vol. 460, p. 367, 2009.

[68] H.-J. Chang, S.-H. Kim, Y.-H. Lee, E. P. Kartalov, and A. Scherer, "A photonic-crystal optical antenna for extremely large local-eld enhancement," *Opt. Express*, vol. 18, p. 24163, 2010.

[69] M. Notomi, "Theory of light propagation in strongly modulated photonic crystals: Refraction like behavior in the vicinity of the photonic band gap," *Phys. Rev. B*, vol. 62, p. 10696, 2000.

[70] M. I. Stockman, "Nanofocusing of optical energy in tapered plasmonic waveguides," *Phys. Rev. Lett.*, vol. 93, p. 137404, 2004.

[71] L. A. Coldren and S. W. Corzine, *Diode Lasers and Photonic Integrated Circuits*. John Wiley & Sons, Inc., 1995.

[72] S.-W. Chang, T.-R. Lin, and S. L. Chuang, "Theory of plasmonic fabry-perot nanolasers," *Opt. Express*, vol. 18, p. 15039, 2010.

[73] M. Fujita, A. Sakai, and T. Baba, "Ultrasmall and ultralow threshold GaInAsP-InP microdisk injection lasers: design, fabrication, lasing characteristics, and spontaneous emission factor," *IEEE J. Sel. Top. Quantum Electron.*, vol. 5, p. 673, 1999.

[74] W. W. Chow, P. M. Smowton, P. Blood, A. Girndt, F. Jahnke, and S. W. Koch, "Comparison of experimental and theoretical GaInP quantum well gain spectra," *Appl. Phys. Lett.*, vol. 71, p. 157, 1997.

[75] K. S. Yee, "Numerical solution of initial boundary value problems involving Maxwell's equations in isotropic media," *IEEE Trans. Antennas Propagat.*, vol. 14, p. 302, 1966.

[76] J. P. Berenger, "A perfectly matched layer for the absorption of electromagnetic waves," *J. Computational Physics*, vol. 114, p. 185, 1994.

[77] M. Okoniewski, M. Mrozowski, and M. A. Stuchly, "Simple treatment of multi-term dispersion in FDTD," *IEEE Microwave Guided Wave Lett.*, vol. 7, p. 121, 1997.

[78] A. Taflove and S. C. Hagness, *Computational Electrodynamics—The Finite-Difference Time-Domain Method*. Artech House, Norwood, 2005.

[79] J. G. Maloney and G. S. Smith, "The efficient modeling of thin material sheets in the fdtd method," *IEEE Trans. Antennas Propagat.*, vol. 40, p. 323, 1992.

[80] (2012) Thorlabs, Inc. [Online]. Available: http://www.thorlabs.us

[81] S. L. McCall, A. F. J. Levi, R. E. Slusher, S. J. Pearton, and R. A. Logan, "Whispering-gallery mode microdisk lasers," *Appl. Phys. Lett.*, vol. 60, p. 289, 1991.

[82] A. F. J. Levi, S. L. McCall, S. J. Pearton, and R. A. Logan, "Room temperature operation of submicrometre radius disk laser," *Electron. Lett.*, vol. 29, p. 1666, 1993.

[83] K. Srinivasan, M. Borselli, O. Painter, A. Stintz, and S. Krishna, "Cavity Q, mode volume, and lasing threshold in small diameter AlGaAs microdisks with embedded quantum dots," *Opt. Express*, vol. 14, p. 1094, 2006.

[84] A. F. J. Levi, R. E. Slusher, S. L. McCall, J. L. Glass, S. J. Pearton, and R. A. Logan, "Directional light coupling from microdisk lasers," *Appl. Phys. Lett.*, vol. 62, p. 561, 1993.

[85] S.-K. Kim, S.-H. Kim, G.-H. Kim, H.-G. Park, D.-J. Shin, and Y.-H. Lee, "Highly directional emission from few-micron-size elliptical microdisks," *Appl. Phys. Lett.*, vol. 84, p. 861, 2004.

[86] S. Kita, K. Nozaki, S. Hachuda, H. Watanabe, Y. Saito, S. Otsuka, T. Nakada, Y. Arita, and T. Baba, "Photonic crystal point-shift nanolasers with and without nanoslots—design, fabrication, lasing, and sensing characteristics," *IEEE J. Sel. Top. Quantum Electron.*, vol. 17, p. 1632, 2011.

[87] J. Huang, S.-H. Kim, P. Regreny, C. Seassal, P. A. Postigo, and A. Scherer, "InAsP/InP nanobeam photonic crystal laser with quasi-continuous-wave operation and directional emission," 2012, manuscript in preparation.

[88] C. A. Balanis, *Advanced Engineering Electromagnetics*. Wiley, New York, 1989.

[89] J. Vučković, M. Lončar, H. Mabuchi, and A. Scherer, "Optimization of the q factor in photonic crystal microcavities," *IEEE J. Quantum Electron.*, vol. 38, p. 850, 2002.

[90] O. Painter, J. Vučković, and A. Scherer, "Defect modes of a two-dimensional photonic crystal in an optically thin dielectric slab," *J. Opt. Soc. Am. B*, vol. 16, p. 275, 1999.

[91] L. A. Graham, D. L. Huffaker, and D. G. Deppe, "Spontaneous lifetime control in a native-oxide-apertured microcavity," *Appl. Phys. Lett.*, vol. 74, p. 2408, 1999.

[92] Y. Yamamoto and S. Machida, "Microcavity semiconductor laser with enhanced spontaneous emission," *Phys. Rev. A*, vol. 44, p. 657, 1991.

[93] H. Yokoyama and S. D. Brorson, "Rate equation analysis of microcavity lasers," *J. Appl. Phys.*, vol. 66, p. 4801, 1989.

[94] H. Yokoyama, "Physics and device application of optical microcavities," *Science*, vol. 256, p. 66, 1992.

[95] J. Gérard and B. Gayral, "Toward high-efficiency quantum-dot single-photon sources," *Proc. SPIE*, vol. 5361, p. 88, 2004.

[96] K. Inoshita and T. Baba, "Fabrication of GaInAsP/InP photonic crystal lasers by ICP etching and control of resonant mode in point and line composite defects," *IEEE J. Sel. Top. Quantum Electron.*, vol. 9, p. 1347, 2003.

[97] J. K. Hwang, H. Y. Ryu, D. S. Song, I. Y. Han, H. K. Park, D. H. Jang, and Y. H. Lee, "Continuous room-temperature operation of optically pumped two-dimensional photonic crystal lasers at 1.6 μm," *IEEE Photon. Technol. Lett.*, vol. 12, p. 1295, 2000.

[98] J. Cao, W. Kuang, Z.-J. Wei, S.-J. Choi, H. Yu, M. Bagheri, J. O'Brien, and P. Dapkus, "Sapphire-bonded photonic crystal microcavity lasers and their far-field radiation patterns," *IEEE Photon. Technol. Lett.*, vol. 17, p. 4, 2005.

[99] O. J. Painter, "Optical nanocavities in two-dimensional photonic crystal planar waveguides," Ph.D. dissertation, California Institute of Technology, Pasadena, CA, 2001.

[100] S. G. Johnson, S. Fan, P. R. Villeneuve, J. D. Joannopoulos, and L. A. Kolodziejaki, "Guided modes in photonic crystal slabs," *Phys. Rev. B*, vol. 60, p. 5751, 1999.

[101] S.-H. Kim, J. Huang, and A. Scherer, "A photonic crystal nanocavity laser in an optically very thick slab," *Opt. Lett.*, vol. 37, p. 488, 2012.

[102] J. Huang, S.-H. Kim, J. Gardner, P. Regreny, C. Seassal, P. A. Postigo, and A. Scherer, "Room temperature, continuous-wave coupled-cavity InAsP/InP photonic crystal laser with enhanced far-field emission directionality," *Appl. Phys. Lett.*, vol. 99, p. 091110, 2011.

[103] P. B. Johnson and R. W. Christy, "Optical constants of the noble metals," *Phys. Rev. B*, vol. 6, p. 4370, 1972.

[104] J. A. Dionne, L. A. Sweatlock, and H. A. Atwater, "Plasmon slot waveguides: Towards chip-scale propagation with subwavelength-scale localization," *Phys. Rev. B*, vol. 73, p. 035407, 2006.

[105] H. T. Miyazaki and Y. Kurokawa, "Controlled plasmon resonance in closed metal/insulator/metal nanocavities," *Appl. Phys. Lett.*, vol. 89, p. 211126, 2006.

[106] A. Hosseini and Y. Massoud, "Nanoscale surface plasmon based resonator using rectangular geometry," *Appl. Phys. Lett.*, vol. 90, p. 181102, 2007.

[107] K. Yu, A. Lakhani, and M. C. Wu, "Subwavelength metal-optic semiconductor nanopatch lasers," *Opt. Express*, vol. 18, p. 8790, 2010.

[108] J.-C. Weeber, A. Bouhelier, G. C. des Francs, L. Markey, and A. Dereux, "Submicrometer in-plane integrated surface plasmon cavities," *Nano Lett.*, vol. 7, p. 1352, 2007.

[109] A. Mizrahi, V. Lomakin, B. A. Slutsky, M. P. Nezhad, L. Feng, and Y. Fainman, "Low threshold gain metal coated laser nanoresonators," *Opt. Lett.*, vol. 33, p. 1261, 2008.

[110] M. P. Nezhad, A. Simic, O. Bondarenko, B. Slutsky, A. Mizrahi, L. Feng, V. Lomakin, , and Y. Fainman, "Room-temperature subwavelength metallo-dielectric lasers," *Nat. Photonics*, vol. 4, p. 395, 2010.

[111] Y. Arakawa and H. Sakaki, "Multidimensional quantum well laser and temperature dependence of its threshold current," *Appl. Phys. Rev.*, vol. 40, p. 939, 1982.

[112] T. Baba, "Photonic crystals and microdisk cavities based on GaInAsP-InP system," *IEEE J. Sel. Top. Quantum Electron.*, vol. 3, p. 808, 1997.

[113] Z. Zhang, L. Yang, V. Liu, T. Hong, K. Vahala, and A. Scherer, "Visible submicron microdisk lasers," *Appl. Phys. Lett.*, vol. 90, p. 111119, 2007.

[114] Q. Song, H. Cao, S. T. Ho, and G. S. Solomon, "Near-IR subwavelength microdisk lasers," *Appl. Phys. Lett.*, vol. 94, p. 061109, 2009.

[115] (2001) Ioffe physico-technical institute electronic archive of new semiconductor materials, characteristics, and properties. [Online]. Available: http://www.ioffe.ru/SVA/NSM

[116] C. E. Hofmann, E. J. R. Vesseur, L. A. Sweatlock, H. J. Lezec, F. J. G. de Abajo, A. Polman, and H. A. Atwater, "Plasmonic modes of annular nanoresonators imaged by spectrally resolved cathodoluminescence," *Nano Lett.*, vol. 7, p. 3612, 2007.

[117] H. Kato, S. Adachi, H. Nakanishi, and K. Ohtsuka, "Optical properties of $(Al_xGa_{1-x})_{0.5}In_{0.5}P$ quaternary alloys," *Jpn. J. Appl. Phys.*, vol. 33, p. 186, 1994.

[118] G. Hunziker, W. Knop, and C. Harder, "Gain measurement on one, two, and three strained GaInP quantum well laser diodes," *IEEE Trans. Quantum Electron.*, vol. 30, p. 2235, 1994.

[119] M. T. Hill, M. Marell, E. S. P. Leong, B. Smalbrugge, Y. Zhu, M. Sun, P. J. van Veldhoven, E. J. Geluk, F. Karouta, Y.-S. Oei, R. Nötzel, C.-Z. Ning, and M. K. Smit, "Lasing in metal-insulator-metal sub-wavelength plasmonic waveguides," *Opt. Express*, vol. 17, p. 11107, 2009.

[120] F. Qian, Y. Li, S. Gradecak, H.-G. Park, Y. Dong, Y. Ding, Z. L. Wang, and C. M. Lieber, "Multi-quantum-well nanowire heterostructures for wavelength-controlled lasers," *Nat. Mater.*, vol. 7, p. 701, 2008.

[121] E. F. Schubert, Y.-H. Wang, A. Y. Cho, L.-W. Tu, and G. J. Zydzik, "Resonant cavity light-emitting diode," *Appl. Phys. Lett.*, vol. 60, p. 1992, 1992.

[122] H. Benisty, H. D. Neve, and C. Weisbuch, "Impact of planar microcavity effects on light extraction—Part I: basic concepts and analytical trends," *IEEE J. Quantum Electron.*, vol. 34, p. 1612, 1998.

[123] R. A. Matula, "Electrical resistivity of copper, gold, palladium, and silver," *J. Phys. Chem. Ref. Data*, vol. 8, p. 1147, 1979.

[124] S. Strauf, K. Hennessy, M. T. Rakher, Y.-S. Choi, A. Badolato, L. C. Andreani, E. L. Hu, P. M. Petroff, and D. Bouwmeester, "Self-tuned quantum dot gain in photonic crystal lasers," *Phys. Rev. Lett.*, vol. 96, 2006.

[125] Y. Akahane, T. Asano, B.-S. Song, and S. Noda, "Fine-tuned high-Q photonic-crystal nanocavity," *Opt. Express*, vol. 13, p. 1202, 2005.

[126] M. Loncar, M. Hochberg, A. Scherer, and Y. Qiu, "High quality factors and room-temperature lasing in a modified single-defect photonic crystal cavity," *Opt. Lett.*, vol. 29, p. 721, 2004.

[127] M. Fujita, A. Sugitatsu, T. Uesugi, and S. Noda, "Fabrication of indium phosphide compound photonic crystal by hydrogen iodide/xenon inductively coupled plasma etching," *Jpn. J. Appl. Phys.*, vol. 43, p. L1400, 2004.

[128] K. Srinivasan, P. Barclay, and O. Painter, "Fabrication-tolerant high quality factor photonic crystal microcavities," *Opt. Express*, vol. 12, p. 1458, 2004.

[129] J. P. Dowling, M. Scully, and F. DeMartini, "Radiation pattern of a classical dipole in a cavity," *Opt. Comm.*, vol. 82, p. 415, 1991.

[130] S. Fan and J. D. Joannopoulos, "Analysis of guided resonances in photonic crystal slabs," *Phys. Rev. B*, vol. 65, p. 235112, 2002.

[131] T. Baba and D. Sano, "Low threshold lasing and Purcell effect in microdisk lasers at room temperature," *IEEE J. Sel. Top. Quantum Electron.*, vol. 9, p. 1340, 2003.

[132] A. Tandaechanurat, S. Iwamoto, M. Nomura, N. Kumagai, and Y. Arakawa, "Increase of Q-factor in photonic crystal H1-defect nanocavities after closing of photonic bandgap with optimal slab thickness," *Opt. Express*, vol. 16, p. 448, 2008.

[133] H. Altug and J. Vučković, "Photonic crystal nanocavity array laser," *Opt. Express*, vol. 13, p. 8819, 2005.

[134] A. R. Alija, L. J. Martínez, P. A. Postigo, C. Seassal, and P. Viktorovitch, "Coupled-cavity two-dimensional photonic crystal waveguide ring laser," *Appl. Phys. Lett.*, vol. 89, p. 101102, 2006.

[135] K. Nozaki, H. Watanabe, and T. Baba, "Photonic crystal nanolaser monolithically integrated with passive waveguide for effective light extraction," *Appl. Phys. Lett.*, vol. 92, p. 021108, 2008.

[136] N.-V.-Q. Tran, S. Combrié, and A. D. Rossi, "Directive emission from high-Q photonic crystal cavities through band folding," *Phys. Rev. B*, vol. 79, p. 041101(R), 2009.

[137] J.-H. Kang, M.-K. Seo, S.-K. Kim, S.-H. Kim, M.-K. Kim, H.-G. Park, K.-S. Kim, and Y.-H. Lee, "Polarized vertical beaming of an engineered hexapole mode laser," *Opt. Express*, vol. 17, p. 6074, 2009.

[138] P. B. Deotare, M. W. McCutcheon, I. W. Frank, M. Khan, and M. Lončar, "Coupled photonic crystal nanobeam cavities," *Appl. Phys. Lett.*, vol. 95, p. 031102, 2009.

[139] I. W. Frank, P. B. Deotare, M. W. McCutcheon, and M. Lončar, "Programmable photonic crystal nanobeam cavities," *Opt. Express*, vol. 18, p. 8705, 2010.

[140] M. Eicheneld, R. Camacho, J. Chan, K. J. Vahala, and O. Painter, "A picogram- and nanometre-scale photoniccrystal optomechanical cavity," *Nature*, vol. 459, p. 550, 2009.

[141] T. P. M. Alegre, R. Perahia, and O. Painter, "Optomechanical zipper cavity lasers: theoretical analysis of tuning range and stability," *Opt. Express*, vol. 18, p. 7872, 2010.

[142] S. Fan, J. N. Winn, A. Devenyi, J. C. Chen, R. D. Meade, and J. D. Joannopoulos, "Guided and defect modes in periodic dielectric waveguides," *J. Opt. Soc. Am. B*, vol. 12, p. 1267, 1995.

[143] P. Lalanne, S. Mias, and J. P. Hugonin, "Two physical mechanisms for boosting the quality factor to cavity volume ratio of photonic crystal microcavities," *Opt. Express*, vol. 12, p. 458, 2004.

[144] C. Sauvan, G. Lecamp, P. Lalanne, and J. P. Hugonin, "Modal-reflectivity enhancement by geometry tuning in photonic crystal microcavities," *Opt. Express*, vol. 13, p. 245, 2005.

[145] C. Sauvan, P. Lalanne, and J. P. Hugonin, "Slow-wave effect and mode-prole matching in photonic crystal microcavities," *Phys. Rev. B*, vol. 71, p. 165118, 2005.

[146] R. D. Meade, A. M. Rappe, K. D. Brommer, and J. D. Joannopoulos, "Nature of the photonic band gap: some insights from a field analysis," *J. Opt. Soc. Am. B*, vol. 10, p. 328, 1993.

[147] Y. Tanaka, T. Asano, Y. Akahane, B.-S. Song, and S. Noda, "Theoretical investigation of a two-dimensional photonic crystal slab with truncated cone air holes," *Appl. Phys. Lett.*, vol. 82, p. 1661, 2003.

[148] M.-K. Kim, J.-K. Yang, Y.-H. Lee, and I.-K. Hwang, "Influence of etching slope on two-dimensional photonic crystal slab resonators," *J. Korean Phys. Soc.*, vol. 5, p. 1027, 2007.

[149] S. G. Johnson, S. Fan, A. Mekis, and J. D. Joannopoulos, "Multipole-cancellation mechanism for high-Q cavities in the absence of a complete photonic band gap," *Appl. Phys. Lett.*, vol. 78, p. 3388, 2001.

[150] K. Srinivasan and O. Painter, "Momentum space design of high-Q photonic crystal optical cavities," *Opt. Express*, vol. 10, p. 670, 2002.

[151] U. K. Khankhoje, S.-H. Kim, B. C. Richards, J. Hendrickson, J. Sweet, J. D. Olitzky, G. Khitrova, H. M. Gibbs, and A. Scherer, "Modelling and fabrication of GaAs photonic-crystal cavities for cavity quantum electrodynamics," *Nanotechnology*, vol. 21, p. 065202, 2010.

[152] (2012) Wolfram Alpha. [Online]. Available: http://www.wolframalpha.com

[153] S. Budavari, ed., *The Merck index: an encyclopedia of chemicals, drugs, and biologicals*, 11th ed. Merck, Rahway, NJ, 1989.

[154] E. A. Peretti, "Thermal analysis of the indium-iodine system," *J. Am. Chem. Soc.*, vol. 78, p. 5745, 1956.

[155] I. Junarsa, M. P. Stoykovich, P. F. Nealey, Y. Ma, F. Cerrina, and H. H. Solak, "Hydrogen silsesquioxane as a high resolution negative-tone resist for extreme ultraviolet lithography," *J. Vac. Sci. Technol. B*, vol. 23, p. 138, 2005.

[156] H. Namatsu, Y. Takahashi, K. Yamazaki, T. Yamaguchi, M. Nagase, and K. Kurihara, "Three-dimensional siloxane resist for the formation of nanopatterns with minimum linewidth fluctuations," *J. Vac. Sci. Technol. B*, vol. 16, p. 69, 1998.

[157] T. Nakamura, M. Sasaki, A. Kobayashi, K. Sawa, and K. Mine, "Oxidative curing of hydrogen silsesquioxane resin films by electron beam irradiation without additional heatings and characterization of the cured films," *Jpn. J. Appl. Phys.*, vol. 40, p. 6187, 2001.

[158] D. P. Mancini, K. A. Gehoski, E. Ainley, K. J. Nordquist, D. J. Resnick, T. C. Bailey, S. V. Sreenivasan, J. G. Ekerdt, and C. G. Willson, "Hydrogen silsesquioxane for direct electron-beam patterning of step and ash imprint lithography templates," *J. Vac. Sci. Technol. B*, vol. 20, p. 2896, 2002.

[159] C.-C. Yang and W.-C. Chen, "The structures and properties of hydrogen silsesquioxane (HSQ) films produced by thermal curing," *J. Mater. Chem.*, vol. 12, p. 1138, 2002.

[160] K. Srinivasan, P. E. Barclay, O. Painter, J. Chen, and A. Y. Cho, "Fabrication of high-quality-factor photonic crystal microcavities in InAsP/InGaAsP membranes," *J. Vac. Sci. Technol. B*, vol. 22, p. 875, 2004.

[161] H. Huang, X. Wang, X. Ren, Q. Wang, and Y. Huang, "Selective wet etching of InGaAs/InGaAsP in HCl/HF/CrO3 solution: application to vertical taper structures in integrated optoelectronic devices," *J. Vac. Sci. Technol. B*, vol. 23, p. 1650, 2005.

[162] A. F. J. Levi, R. E. Slusher, S. L. McCall, T. Tanbun-Ek, D. L. Coblentz, and S. J. Pearton, "Room temperature operation of microdisc lasers with submilliamp threshold current," *Electron. Lett.*, vol. 28, p. 1010, 1992.

[163] T. Baba, P. Fujita, A. Sakai, M. Kihara, and R. Watanabe, "Lasing characteristics of GaInAsP-InP strained quantum-well microdisk injection lasers with diameter of 2-10 μm," *IEEE Photonics Technol. Lett.*, vol. 9, p. 878, 1997.

[164] G. Björk, A. Karlsson, and Y. Yamamoto, "On the linewidth of microcavity lasers," *Appl. Phys. Lett.*, vol. 60, p. 304, 1992.

[165] R. J. Glauber, "The quantum theory of optical coherence," *Phys. Rev.*, vol. 130, p. 2529, 1963.

[166] R. Jin, D. Boggavarapu, M. Sargent, P. Meystre, H. M. Gibbs, and G. Khitrova, "Photon-number correlations near the threshold of microcavity lasers in the weak-coupling regime," *Phys. Rev. A*, vol. 49, p. 4038, 1994.

[167] S. M. Ulrich, C. Gies, S. Ates, J. Wiersig, S. Reitzenstein, C. Hofmann, A. Löffler, A. Forchel, F. Jahnke, and P. Michler, "Photon statistics of semiconductor microcavity lasers," *Phys. Rev. Lett.*, vol. 98, p. 043906, 2007.

[168] L. J. Martinez, B. Alén, I. Prieto, D. Fuster, L. González, Y. González, M. L. Dotor, and P. A. Postigo, "Room temperature continuous wave operation in a photonic crystal microcavity laser with a single layer of InAs/InP self-assembled quantum wires," *Opt. Express*, vol. 17, p. 14993, 2009.

[169] K. Tanabe, M. Nomura, D. Guimard, S. Iwamoto, and Y. Arakawa, "Room temperature continuous wave operation of InAs/GaAs quantum dot photonic crystal nanocavity laser on silicon substrate," *Opt. Express*, vol. 17, p. 7036, 2009.

[170] S. W. Corzine, R.-H. Yan, and L. A. Coldren, *Optical gain in III-V bulk and quantum well semiconductors.* Academic Press, Inc., San Diego, CA, 1993.

[171] S. Y. Hu, S. W. Corzine, K. K. Law, D. B. Young, A. C. Gossard, L. A. Coldren, and J. L. Merz, "Lateral carrier diffusion and surface recombination in InGaAs/AlGaAs quantum well ridge waveguide lasers," *J. Appl. Phys.*, vol. 76, p. 4479, 1994.

[172] M. E. Heimbuch, J. A. L. Holmes, C. M. Reaves, M. P. Mack, S. P. DenBaars, and L. A. Coldren, "Tertiarybutylarsine and tertiarybutylphosphine for the MOCVD growth of low threshold 1.55 μm InxGa1-xAs/InP quantum-well lasers," *J. Electron. Mater.*, vol. 23, p. 87, 1994.

[173] C. J. Sandroff, R. N. Nottenburg, J.-C. Bischoff, and R. Bhat, "Dramatic enhancement in the gain of a GaAs/AIGaAs heterostructure bipolar transistor by surface chemical passivation," *Apply. Phys. Lett.*, vol. 51, p. 33, 1987.

[174] S. R. Lunt, G. N. Fiyba, P. G. Santangelo, and N. S. Lewis, "Chemical studies of the passivation of GaAs surface recombination using surfides and thiols," *J. Appl. Phys.*, vol. 70, p. 7449, 1991.

[175] D. Englund, H. Altug, and J. Vučković, "Low-threshold surface-passivated photonic crystal nanocavity laser," *Appl. Phys. Lett.*, vol. 91, p. 071124, 2007.

[176] M. Boroditsky, R. Vrijen, V. F. Krauss, R. Coccioli, R. Bhat, and E. Yablonovitch, "Spontaneous emission and Purcell enhancement from thin-film 2-D photonic crystals," *J. Lightwave Tech.*, vol. 17, p. 2096, 1999.

[177] T. Baba, K. Inoshita, H. Tanaka, J. Yonekura, M. Ariga, A. Matsutani, T. Miyamoto, F. Koyama, and K. Iga, "Strong enhancement of light extraction efficiency in GaInAsP 2-D-arranged microcolumns," *J. Lightwave Technol.*, vol. 17, p. 2113, 1999.

[178] W. Shockley and J. W. T. Read, "Statistics of the recombinations of holes and electrons," *Phys. Rev.*, vol. 87, p. 835, 1952.

[179] R. N. Hall, "Electron-hole recombination in germanium," *Phys. Rev.*, vol. 87, p. 387, 1952.

[180] H.-Y. Ryu, J.-K. Hwang, D.-S. Song, I.-Y. Han, and Y.-H. Lee, "Effect of nonradiative recombination on light emitting properties of two dimensional photonic crystal slab structures," *Appl. Phys. Lett.*, vol. 78, p. 1174, 2001.

[181] V. Swaminathan, J. M. Freund, L. M. F. Chirovsky, T. D. Harris, N. A. Kuebler, and L. A. D'Asaro, "Evidence for surface recombination at mesa sidewalls of self-electro-optic effect devices," *J. Appl. Phys.*, vol. 68, p. 4116, 1990.

[182] D. D. Nolte, "Surface recombination, free-carrier saturation, and dangling bonds in InP and GaAs," *Solid-State Electron.*, vol. 33, p. 295, 1990.

[183] B. Sermage, H. J. Eichler, J. P. Heritage, R. J. Nelson, and N. K. Dutta, "Photoexcited carrier lifetime and Auger recombination in 1.3 μm InGaAsP," *Appl. Phys. Lett.*, vol. 42, p. 259, 1983.

[184] E. Wintner and E. P. Ippen, "Nonlinear carrier dynamics in $Ga_xIn_{1-x}As_yP_{1-y}$ compounds," *Appl. Phys. Lett.*, vol. 44, p. 99, 1984.

[185] H. Watanabe, K. Nozaki, and T. Baba, "Very wide wavelength chirping in photonic crystal nanolaser," in *Int. Symp. Compound Semicond.*, Kyoto, Japan, October 2007, p. TuC 9.

[186] G. Dagnall, J.-J. Shen, T.-H. Kim, R. A. Metzger, A. S. Brown, and S. R. Stock, "Solid source MBE growth of InAsP/InP quantum wells," *J. Electron. Mater.*, vol. 28, p. 933, 1999.

[187] J. A. McCaulley, V. M. Donnelly, M. Vernon, and I. Taha, "Temperature dependence of the near-infrared refractive index of silicon, gallium arsenide, and indium phosphide," *Phys. Rev. B*, vol. 49, p. 7408, 1994.

[188] F. G. D. Corte, G. Cocorullo, M. Iodice, and I. Rendina, "Temperature dependence of the thermo-optic coefficient of InP, GaAs, and SiC from room temperature to 600 K at the wavelength of 1.5 μm," *Appl. Phys. Lett.*, vol. 77, p. 1614, 2000.

[189] A. R. Adams, M. Asada, Y. Suematsu, and S. Arai, "The temperature dependence of the efficiency and threshold current of $In_{1-x}Ga_xAs_yP_{1-y}$ lasers related to intervalence band absorption," *Jpn. J. Appl. Phys.*, vol. 19, p. L621, 1980.

[190] Y. Zhang, M. Khan, Y. Huang, J. Ryou, P. Deotare, R. Dupuis, and M. Lončar, "Photonic crystal nanobeam lasers," *Appl. Phys. Lett.*, vol. 97, p. 051104, 2010.

[191] Y. Gong, B. Ellis, G. Shambat, T. Sarmiento, J. S. Harris, and J. Vučković, "Nanobeam photonic crystal cavity quantum dot laser," *Opt. Express*, vol. 18, p. 8781, 2010.

[192] V. R. Almeida, C. A. Barrios, R. R. Panepucci, and M. Lipson, "All-optical control of light on a silicon chip," *Nature*, vol. 431, p. 1081, 2004.

[193] T. Tanabe, M. Notomi, S. Mitsugi, A. Shinya, and E. Kuramochi, "All-optical switches on a silicon chip realized using photonic crystal nanocavities," *Appl. Phys. Lett.*, vol. 87, p. 151112, 2005.

[194] M. Hochberg, T. Baehr-Jones, G. Wang, M. Shearn, K. Harvard, J. Luo, B. Chen, Z. Shi, R. Lawson, P. Sullivan, A. K. Y. Jen, L. Dalton, and A. Scherer, "Terahertz all-optical modulation in a siliconpolymer hybrid system," *Nat. Mater.*, vol. 5, p. 703, 2006.

[195] K. Nozaki, T. Tanabe, A. Shinya, S. Matsuo, T. Sato, H. Taniyama, and M. Notomi, "Sub-femtojoule all-optical switching using a photonic-crystal nanocavity," *Nat. Photonics*, vol. 4, p. 477, 2010.

[196] A. Liu, R. Jones, L. Liao, D. Samara-Rubio, D. Rubin, O. Cohen, R. Nicolaescu, and M. Paniccia, "A high-speed silicon optical modulator based on a metal-oxide-semiconductor capacitor," *Nature*, vol. 427, p. 615, 2004.

[197] M. Lipson, "Compact electro-optic modulators on a silicon chip," *IEEE J. Sel. Top. Quantum Electron.*, vol. 12, p. 1520, 2006.

[198] Q. Xu, S. Manipatruni, B. Schmidt, J. Shakya, and M. Lipson, "12.5 Gbit/s carrier-injection-based silicon microring silicon modulators," *Opt. Express*, vol. 15, p. 430, 2007.

[199] B. Schmidt, Q. Xu, J. Shakya, S. Manipatruni, and M. Lipson, "Compact electro-optic modulator on silicon-on-insulator substrates using cavities with ultra-small modal volumes," *Opt. Express*, vol. 15, p. 3140, 2007.

[200] W. M. J. Green, M. J. Rooks, L. Sekaric, and Y. A. Vlasov, "Ultra-compact, low RF power, 10 Gb/s silicon Mach-Zehnder modulator," *Opt. Express*, vol. 15, p. 17106, 2007.

[201] T. Tanabe, N. Notomi, S. Mitsugi, A. Shinya, and E. Kuramochi, "Fast bistable all-optical switch and memory on a silicon photonic crystal on-chip," *Opt. Express*, vol. 30, p. 2575, 2005.

[202] A. Shinya, S. Matsuo, Yosia, T. Tanabe, E. Kuramochi, T. Sato, T. Kakitsuka, and M. Notomi, "All-optical on-chip bit memory based on ultra high-Q InGaAsP photonic crystal," *Opt. Express*, vol. 16, p. 19382, 2008.

[203] T. Tanabe, H. Sumikura, H. Taniyama, A. Shinya, and M. Notomi, "All-silicon sub-Gb/s telecom detector with low dark current and high quantum efficiency on chip," *Appl. Phys. Lett.*, vol. 96, p. 101103, 2010.

[204] M. A. Foster, A. C. Turner, J. E. Sharping, B. S. Schmidt, M. Lipson, and A. L. Gaeta, "Broad-band optical parametric gain on a silicon photonic chip," *Nature*, vol. 441, p. 960, 2006.

[205] (2011) Intel Research - Photonics. [Online]. Available: http://techresearch.intel.com/ResearchAreaDetails.aspx?Id=26

[206] (2010, Dec.) IBM Research - Silicon Integrated Nanophotonics. [Online]. Available: www.research.ibm.com/photonics

[207] (2012) Infinera Corporation. [Online]. Available: http://www.infinera.com

[208] D. J. Griffiths, *Introduction to Electrodynamics*. Prentice-Hall, Inc., Upper Saddle River, NJ, 1999.

[209] B. Schmid, A. Petrov, and M. Eich, "Optimized grating coupler with fully etched slots," *Opt. Express*, vol. 17, p. 11066, 2009.

[210] A. Shacham, K. Bergman, and L. P. Carloni, "On the design of a photonic network on chip," in *Proceedings of the First IEEE International Symposium on Networks-on-Chips*, Institute of Electrical and Electronics Engineers, New York, 2007, p. 53.

[211] D. A. B. Miller, "Device requirements for optical interconnects to silicon chips," *Proc. IEEE*, vol. 97, p. 1166, 2009.

[212] R. Soref and B. Bennett, "Electrooptical effects in silicon," *IEEE J. Quantum Electron.*, vol. 23, p. 123, 1987.

[213] (2009) Covega technology - thorlabs quantum electronics. [Online]. Available: http://www.covega.com

[214] Y. Enami, C. T. Derose, D. Mathine, C. Loychik, C. Greenlee, R. A. Norwood, T. D. Kim, J. Luo, Y. Tian, A. K.-Y. Jen, and N. Peyghambarian, "Hybrid polymer/solgel waveguide modulators with exceptionally large electrooptic coefficients," *Nat. Photonics*, vol. 1, p. 180, 2007.

[215] Y. Enami, D. Mathine, C. T. DeRose, R. A. Norwood, J. Luo, A. K.-Y. Jen, and N. Peyghambarian, "Hybrid cross-linkable polymer/sol-gel waveguide modulators with 0.65 V half wave voltage at 1550 nm," *Appl. Phys. Lett.*, vol. 91, p. 093505, 2007.

[216] D. Chen, H. R. Fetterman, A. Chen, W. H. Steier, L. R. Dalton, W. Wang, and Y. Shi, "Demonstration of 110 GHz electro-optic polymer modulators," *Appl. Phys. Lett.*, vol. 70, p. 3335, 1997.

[217] P. A. Sullivan, B. C. Olbricht, A. J. P. Akelaitis, A. A. Mistry, Y. Liao, and L. R. Dalton, "Tricomponent dielsalder polymerized dendrimer glass exhibiting large, thermally stable, electro-optic activity," *J. Mater. Chem.*, vol. 17, p. 2899, 2007.

[218] T. Baehr-Jones, M. Hochberg, G. Wang, R. Lawson, Y. Liao, P. Sullivan, L. Dalton, A. Jen, and A. Scherer, "Optical modulation and detection in slotted silicon waveguides," *Opt. Express*, vol. 13, p. 5216, 2005.

[219] T. Baehr-Jones, B. Penkov, J. Huang, P. Sullivan, J. Davies, J. Takayesu, J. Luo, T.-D. Kim, L. Dalton, A. Jen, M. Hochberg, and A. Scherer, "Nonlinear polymer-clad silicon slot waveguide modulator with a half wave voltage of 0.25 v," *Appl. Phys. Lett.*, vol. 92, p. 163303, 2008.

[220] B. Bortnik, Y.-C. Hung, H. Tazawa, B.-J. Seo, J. Luo, A. K.-Y. Jen, W. H. Steier, and H. R. Fetterman, "Electrooptic polymer ring resonator modulation up to 165 GHz," *IEEE J. Sel. Top. Quantum Electron.*, vol. 13, p. 104, 2007.

[221] G. Wang, T. Baehr-Jones, M. Hochberg, and A. Scherer, "Design and fabrication of segmented, slotted waveguides for electro-optic modulation," *Appl. Phys. Lett.*, vol. 91, p. 143109, 2007.

[222] M. Dinu, F. Quochi, and H. Garcia, "Third-order nonlinearities in silicon at telecom wavelengths," *Appl. Phys. Lett.*, vol. 82, p. 2954, 2003.

[223] A. Liu, H. Rong, M. Paniccia, O. Cohen, and D. Hak, "Net optical gain in a low loss silicon-on-insulator waveguide by stimulated Raman scattering," *Opt. Express*, vol. 12, p. 4261, 2004.

[224] H. Rong, A. Liu, R. Nicolaescu, M. Paniccia, O. Cohen, and D. Hak, "Raman gain and nonlinear optical absorption measurements in a low-loss silicon waveguide," *Appl. Phys. Lett.*, vol. 85, p. 2196, 2004.

[225] R. Claps, V. Raghunathan, D. Dimitropoulos, and B. Jalali, "Influence of nonlinear absorption on Raman amplification in silicon waveguides," *Opt. Express*, vol. 12, p. 2774, 2004.

[226] H. Y. Fan and A. K. Ramdas, "Infrared absorption and photoconductivity in irradiated silicon," *J. Appl. Phys.*, vol. 30, p. 1127, 1959.

[227] M. W. Geis, S. J. Spector, M. E. Grein, R. T. Schulein, J. U. Yoon, D. M. Lennon, S. Deneault, F. Gan, F. X. Kaertner, and T. M. Lyszczarz, "CMOS-compatible all-Si high-speed waveguide photodiodes with high responsivity in near-infrared communication band," *IEEE Photonics Technol. Lett.*, vol. 19, p. 152, 2007.

[228] Ö. Boyraz, P. Koonath, V. Raghunathan, and B. Jalali, "All optical switching and continuum generation in silicon waveguides," *Opt. Express*, vol. 12, p. 4094, 2004.

[229] D. Dimitropoulos, R. Jhaveri, R. Claps, J. C. S. Woo, and B. Jalali, "Lifetime of photogenerated carriers in silicon-on-insulator rib waveguides," *Appl. Phys. Lett.*, vol. 86, p. 071115, 2005.

[230] T. K. Liang and H. K. Tsang, "Role of free carriers from two-photon absorption in Raman amplification in silicon-on-insulator waveguides," *Appl. Phys. Lett.*, vol. 84, p. 2745, 2004.

[231] A. Liu, H. Rong, R. Jones, O. Cohen, D. Hak, and M. Paniccia, "Optical amplification and lasing by stimulated Raman scattering in silicon waveguides," *IEEE J. Lightwave Technol.*, vol. 24, p. 1440, 2006.

[232] K. Yamada, H. Fukuda, T. Tsuchizawa, T. Watanabe, T. Shoji, and S. Itabashi, "All-optical efficient wavelength conversion using silicon photonic wire waveguide," *IEEE Photonics Technol. Lett.*, vol. 18, p. 1046, 2006.

[233] D. Lenstra, B. H. Verbeek, and A. J. D. Boef, "Coherence collapse in single-mode semiconductor lasers due to optical feedback," *IEEE J. Quantum Electron.*, vol. 21, p. 674, 1985.

[234] R. Lang and K. Kobayashi, "External optical feedback effects on semiconductor injection laser properties," *IEEE J. Quantum Electron.*, vol. 16, p. 347, 1980.

[235] C. H. Henry, "Phase noise in semiconductor lasers," *J. Lightwave Technol.*, vol. 4, p. 298, 1986.

[236] H. Li, J. Ye, and J. G. McInerney, "Detailed analysis of coherence collapse in semiconductor lasers," *IEEE J. Quantum Electron.*, vol. 29, p. 2421, 1993.